DISSERTATION

PHOTOELECTROCHEMICAL MICROSCOPY STUDIES OF TRANSITION METAL DICHALCOGENIDES NANOFLAKES: ADDRESSING OPEN QUESTIONS OF STRUCTURE-FUNCTION RELATIONSHIPS

Submitted by

Michael Van Erdewyk

Department of Chemistry

In partial fulfillment of the requirements

For the Degree of Doctor of Philosophy

Colorado State University

Fort Collins, Colorado

Fall 2022

Doctoral Committee:

Advisor: Justin Sambur

Amber Krummel
Charles Henry
Tim Stasevich

ABSTRACT

PHOTOELECTROCHEMICAL MICROSCOPY STUDIES OF TRANSITION METAL DICHALCOGENIDES NANOFLAKES: ADDRESSING OPEN QUESTIONS OF STRUCTURE-FUNCTION RELATIONSHIPS

Transition metal dichalcogenides (TMDs) are exciting materials for applications in solar energy conversion. However, to advance technologies that leverage these materials, a strong understanding of fundamental photoelectrochemistry and related processes is necessary. Photoelectrochemical microscopy methods are well poised in this aspect. Methods like scanning photoelectrochemical microscopy allow for the excitation of small, localized region of a material with a focused laser and the subsequent measurement of the photocurrent. The measured photocurrent can be related to the position of the laser and the physical attributes of the material surface at the location, and variations in the photocurrent across the surface can be tracked. In this way, the technique offers insight into how different surface motifs affect the photoelectrochemical behavior of the material. This method can be combined with other spectroscopies, such as photoluminescence or Raman, to can further understanding about the studied material. The following work details the use of photoelectrochemical microscopy methods to answer questions relating to both the structure and underlying properties of mechanically exfoliated TMD nanoflakes.

ACKNOWLEDGEMENTS

First, I want to take the space to say thank you to Justin for the support and guidance throughout the past five years. I enjoy the way that you approach science and focus in on what the data really tells us about the underlying chemistry. More and more I am catch myself thinking like you, especially when it comes to how impactful a well-thought-out figure can be.

I also want thank all the Sambur group members, past and present, for their support both in-lab as it relates to the science and out-of-lab as friends. Music City Mondays or trips to the Skeller were always a good time.

To my parents and family, I want to say thank you. Your support of me in all the ways life takes me, means a lot to me. I also appreciate the frequent trips out here to eat good food, drink good beer, and watch some good and some not so good football.

Finally, to Kayla, thank you for your love and patience with me throughout this PhD. Being able to come home after a stressful day or after a great day in the lab and have you there always left me with something to look forward to.

TABLE OF CONTENTS

CHAPTER 1: INTRODUCTION AND BACKGROUND[i]

1.1 Introduction – Basics of Semiconductor Photoelectrochemistry

The basics of semiconductor photoelectrochemistry for bulk systems have been presented in detail by numerous other authors.[1-5] This section will describe in brief the basic equations and terminology of semiconductor photoelectrochemistry as well as discuss the processes that lead to photocurrent. Limitations of these basics as they apply to nanoscale systems will also be discussed.

For this discussion, the basic processes will be described for an n-type semiconductor. Initially, when a semiconductor contacts an electrolyte, an electric field is formed at the semiconductor/electrolyte interface creating a space-charge region. This process is analogous to the formation of the space-charge region of p-n junction. In the semiconductor/electrolyte situation, the Fermi level of the semiconductor (E_F) moves to meet the energy level of the redox active electrolyte species. The movement of the Fermi level is facilitated by the movement of electrons from the semiconductor across the interface and into the electrolyte and results in an equilibrium between the semiconductor and electrolyte. This movement of electrons leaves an excess of positive charge in the semiconductor, that is fixed to dopant atoms within the semiconductor (Figure 1.1).

[i] Section 1.2.2 contains portions of text from a manuscript that has been submitted to Current Opinion in Electrochemistry. The text was written by Michael Van Erdewyk, Dakota Lorenz, and Justin Sambur. The full-text of this manuscript is contained in Chapter 4 of this dissertation.

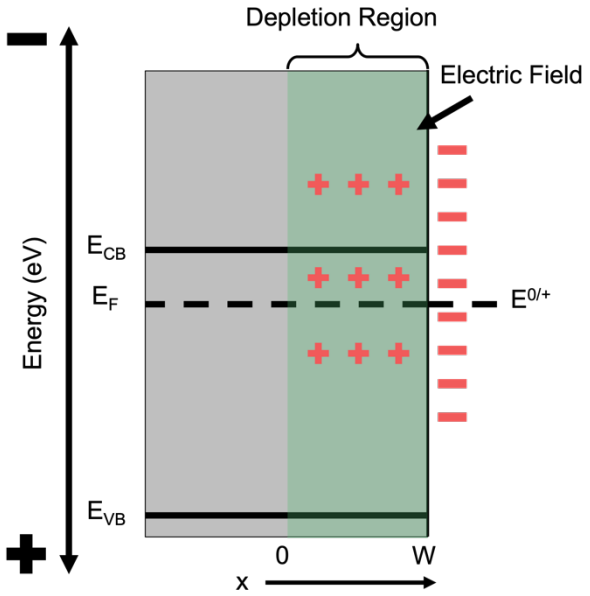

Figure 1.1: A cartoon of a semiconductor in contact with an electrolyte with redox potential $E^{0/+}$. The semiconductor Fermi level and conduction and valence bands are depicted as well as the depletion region (shaded green rectangle). The excess charge left behind in the semiconductor after equilibrating with the electrolyte is depicted by the red "pluses". The x-coordinate is also defined from 0 to W, with 0 being the edge of the depletion region inside of the semiconductor.

Importantly, the movement of electrons from the semiconductor occurs first from the semiconductor surface ($x > 0$), and then from the semiconductor interior until a point at which equilibrium is established ($x = 0$). Thus, the region of left-behind positive charge has been depleted and is referred to as the depletion region (W). Note that the x-coordinate origin is located in the interior of the semiconductor where the edge of the depletion region is located.

Because of the depletion of charge from this region, an electric field forms within the depletion region. The strength of this electric field at any point along the depletion region can be calculated. First, it is assumed that the charge density along the depletion region is a constant ($0 \leq x \leq W$). From there, the electric field strength can be calculated at any point, by Eq. 1.1,

$$E(x) = \frac{qN_d}{\varepsilon_s} x \ (0 \ \leq x \ \leq W) \qquad \text{Eq. 1.1}$$

where *E(x)* is the electric field strength at position *x*, ε_s is the dielectric constant of semiconductor, and N_d is the semiconductor doping density. The maximum electric field strength is then given by the same equation when $x = W$, and is located at the semiconductor/electrolyte interface (Figure 1.4).

The electric potential can then be calculating as the integral of the linear electric field derived from Eq. 1.1. This yields a quadratic expression for the electric potential (V), given in Eq. 1.2.

$$V(x) = -\left(\frac{qN_d}{2\varepsilon_s}\right)x^2 \ (0 \leq x \leq W) \qquad \text{Eq. 1.2}$$

Plots of this quadratic function the electric potential is plotted as a function of *x*, are called band-bending diagrams (Figure 1.2).

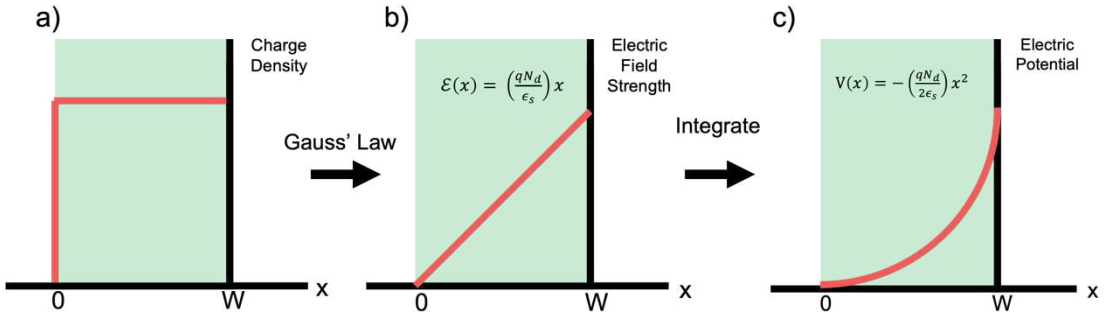

Figure 1.2: Diagrams of the equations that relate charge density, electric field strength, and the electric potential along the coordinate of the depletion region width. (a) A plot of the charge density (red line) as a function of position within the semiconductor (green rectangle). (b) A plot of the equation for the electric field strength as a function of position. (c) A plot of the electric potential within the semiconductor, showing that the highest value is reach at the interface of the semiconductor and electrolyte.

This depiction is useful as the potential energy of an electron within solid can be directly related to the electric potential profile. Similar to the maximum electric field strength, the electric potential is at a maximum at the semiconductor/electrolyte interface (Figure 1.2). The value of Eq. 1.2 when $x = W$ is called the built-in voltage (V_{bi}, see Figure 1.3). The built-in voltage is a property of a specific semiconductor and redox species system and can be calculated as the difference

between the Fermi level and the redox potential of the active species. However, many photoelectrochemical experiments are performed at an applied voltage to the semiconductor. In these circumstances the electric potential, or band-bending, within the semiconductor changes. It is more useful then to discuss the depletion region in terms of the applied potential and the flatband potential (E_{fb}), or the potential that results in the semiconductor valence bands returning to the initial condition before contact with electrolyte. With this definition in mind, Eq. 1.2 can be rearranged to solve for an expression to calculate the depletion region width at an applied potential,

$$W = \sqrt{\frac{2\varepsilon_s(E - E_{fb})}{qN_d}} \qquad \text{Eq. 1.3}$$

where E is the applied potential (relative to a reference electrode. In total, an electric field forms at the semiconductor/electrolyte interface upon contact of the two phases (Figure 1.3). This electric field is important because it separates and facilitates the transport of holes and electrons toward/away from the interface where they can take part in reaction with the redox active species in the electrolyte.

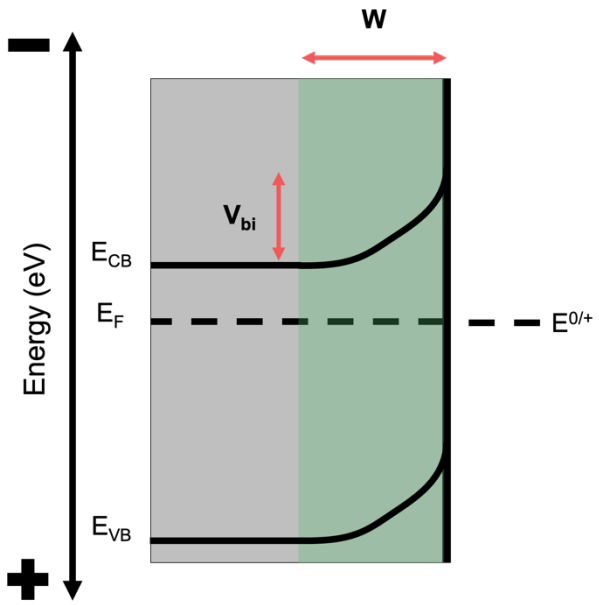

Figure 1.3: A cartoon of the internal band structure of a semiconductor in contact with an electrolyte. The semiconductor Fermi level and electrolyte electrochemical potential are denoted by the black dash lines. The conduction and valence band are shown bent due to the electric potential described above and shown in Figure 1.3. The depletion region width (W) is denoted by the horizontal red arrow and the built-in voltage (V_{bi}) is denoted by the horizontal red arrow.

According to Eq. 1.3, the width of the depletion region is determined by the difference in energies between the semiconductor Fermi level and the energy level of the redox active electrolyte species as well as the doping density (N_d) of the semiconductor. For example, two systems where the doping density is equal but the energy level difference is greater for system A than for system B, the depletion region width will be greater system A as it requires us to "reach further into" the semiconductor to access the electrons necessary to achieve equilibrium.[5]

The above discussion outlines the materials aspect of semiconductor photoelectrochemistry. However, further processes must be considered to understand photocurrent generation in these systems. The major processes that determine photocurrent are: charge carrier generation via photon absorption, charge carrier separation and transport, and interfacial charge transfer. The Gärtner-Butler model provides a quantitative expression for the photocurrent of a

semiconductor photoelectrochemical cell as a function of the applied potential.[6,7] In the model, all charge carriers generated within the depletion region, or within the minority carrier diffusion length of the depletion region edge are assumed to transport to the semiconductor/electrolyte interface with the aid of the internal electric field. All charge carriers that reach the semiconductor/electrolyte interface are assumed to be collected. The model results in the Gärtner-Butler equation that describes that photocurrent increases with increasing anodic potential for an n-type semiconductor. This model has been used to describe the photocurrent-potential relationship of photoelectrochemical cells.[7-9] The assumptions of this model thus can be used to help design an efficient photoelectrochemical cell. By matching the depletion region width of the semiconductor to the penetration depth of incident light, one could expect a highly efficient cell (Figure 1.4). However, as described in Eq. 1.3, the depletion region width is dependent on the doping density which is difficult or expensive to control. Because of this reason, nanoscale systems are exciting options for photoelectrochemical cells because they can be inexpensive and the size of the components is much closer in scale to the depletion region width (Figure 1.3). However, nanoscale systems do not behave the same as bulk electrodes in all cases.

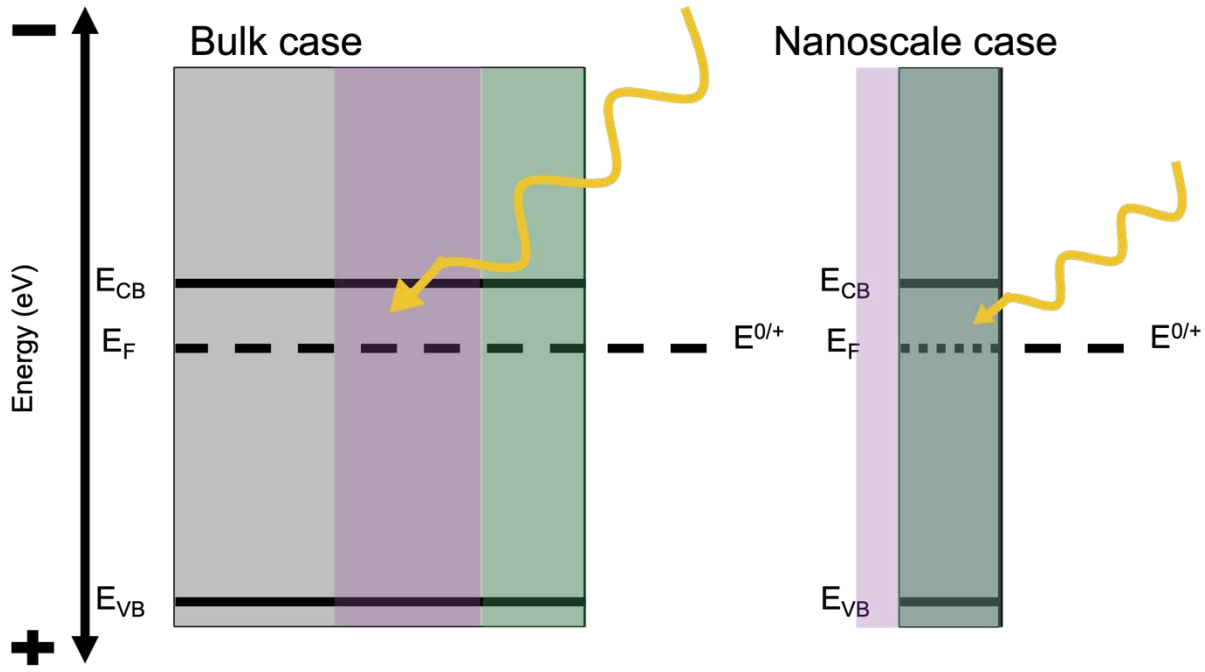

Figure 1.4: Cartoons of the bulk case of a semiconductor and the nanoscale case. The depletion region width is marked by the green rectangle in both cases, and the light penetration depth is shown as a purple rectangle. For the bulk case, the light penetrates much deeper into the semiconductor, thus leading to inefficiency. In the nanoscale case, the light penetration depth matches the depletion region width and thus all charge carriers can be separated by the electric field. For clarity, the semiconductor conduction and valence bands are shown not bent.

A large difference in the behavior of nanoscale systems is the size of the depletion region. For a bulk electrode, the depletion region width might be on the scale of a few hundred nanometers[10], but nanomaterials are on the order of 100 nm or less. In this situation, the shape of the electric potential in the depletion region is no longer quadratic as described by Eq. 1.2. Studies have derived the shape of the electric potential for number of different geometries but the heterogeneity present in many nanomaterial systems has made it difficult to apply these models to experimental studies.[11-16] An additional complication with nanomaterial systems is to maintain high light absorption in combination with short transport distances for photogenerated charge carriers. Regardless of the exact problem in applying bulk theory to nanoscale systems, it is clear

that experimental methods are needed to better understand the photoelectrochemical behavior of nanomaterials. One such approach is to attempt to isolate nanomaterials for individual study. This approach is attractive as it allows for direct correlation of a single nanomaterials' photoelectrochemical behavior to its size and morphology. Single particle photoelectrochemistry studies can be used to address important questions relating to the underlying properties of nanomaterials and provide knowledge that will be useful in the development of new photoelectrochemical cells and other solar energy conversion devices.

1.2 Transition Metal Dichalcogenides For Use In Solar Energy Conversion Applications

1.2.1 Structure and Properties of TMDs

The development of solar energy conversion devices that utilize inexpensive semiconductor materials is a key research area.[10,17-20] Semiconductors have been employed in devices such as the dye-sensitized solar cell or other photovoltaics as well as solar water splitting devices for hydrogen production.[21-23] The basic principles of semiconductor photoelectrochemistry underlie the function of all of these devices. A strong understanding of how the principles of photoelectrochemistry influence device function is thus key to achieving further developments. This is amplified in cases where nanostructured semiconductor materials are utilized. Despite the advantages offered by nanostructured systems (shorter charge transport distance, lower cost of processing)[10,24], there are challenges in understanding the function of these systems because the equations and models used to describe bulk systems no longer apply (as discussed in section 1.1). However, researchers have devoted their efforts to understanding this bulk-to-nano for semiconductor materials. One such group of materials are transition metal dichalcogenides (TMDs), such as MoS_2, $MoSe_2$, WS_2, and

WSe_2.[25-29] These materials are of interest for solar energy conversion applications due to their ideal bandgaps (1-2 eV) and their stability in aqueous media.[30]

TMDs have a layer type structure where each layer is 3 atoms thick in a chalcogen-metal-chalcogen pattern. Individual layers are then separated by weak van der Waals forces (Figure 1.5).

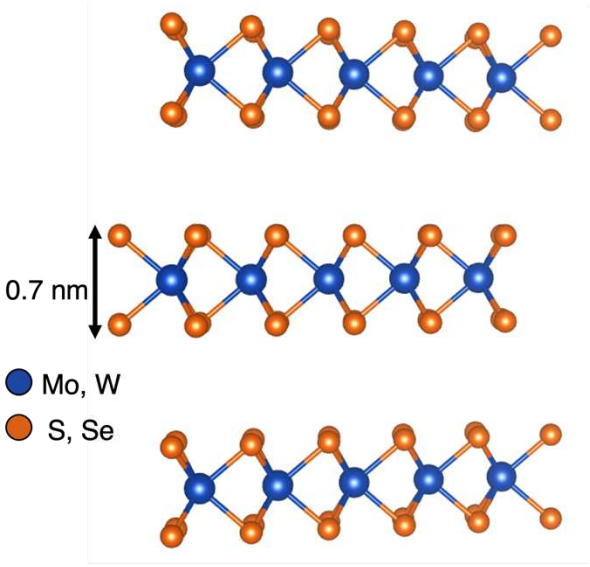

Figure 1.5: Crystal structure of TMDs. Each layer consists of a sandwich of chalcogen-transition metal-chalcogen. The layers are separated by van der Waals forces.

The layer-type structure of these materials results in crystal-to-crystal variation due to differences in layer thickness and surface morphology. The surfaces of TMD crystals contain both smooth basal planes of the S-terminated surface of a crystal layer, and step-edges where the layer thickness of the material changes (Figure 1.6). Step-edges, as well as the perimeter edges of the crystal can be either chalcogen or transition metal terminated.

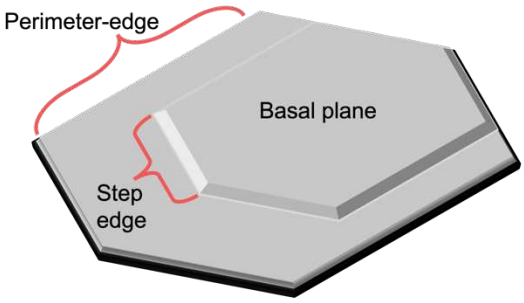

Figure 1.6: Cartoon of a TMD crystal denoting a basal plane, step-edge, and perimeter edge.

The layer-type structure of these materials offers the opportunity of mechanical exfoliation of thinner flakes of material as well as greater surface area (Figure 1.7), similar to "scotch-tape" exfoliation of graphite to graphene.[31,32]

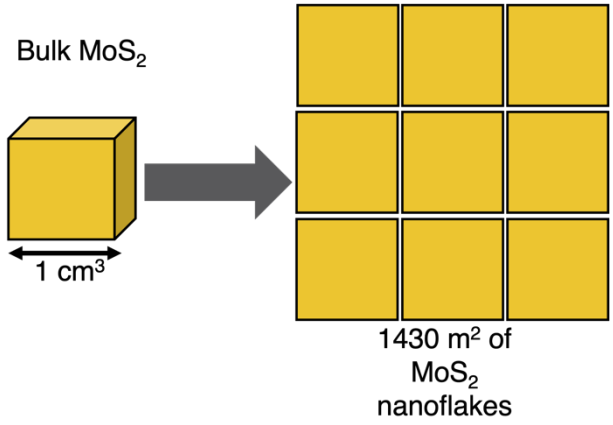

Figure 1.7: Cartoon demonstrating how mechanical exfoliation of bulk TMD crystals greatly increases the surface area of material.

The exfoliation of TMD materials for use in photoelectrochemical energy conversion devices is advantageous as the distance photogenerated electrons and holes must travel from generation to surface collection is shortened, therefore reduced recombination and higher collection efficiencies are expected. Additionally, exfoliated mono- to few-layer flakes have been shown to exhibit unique electronic and light-harvesting properties.[33,34] These developments have led to interest in TMDs for use in photoelectrochemical hydrogen production[35], as well as from the photovoltaic

(PV) community.[36] Furchi and co-workers have demonstrated tunable van der Waals heterojunctions constructed from mechanically exfoliated TMD crystals.[37]

An area of major research focus on exfoliated TMD materials has been the role of surface morphology, such as basal planes and step- and perimeter-edges, in the photoelectrochemical efficiency of the material.[38] Jaramillo and co-workers discovered that the edge-sites of MoS_2 serve as the active sites for hydrogen evolution.[39] This report supports earlier observations by Chaparro and Salvador for TMDs in iodide electrolytes. In those studies, they reported that step-edges exhibited enhanced photoelectrochemical efficiency compared to basal planes.[40-42] However, other researchers have reported that step- and perimeter-edges exhibit decreased photoelectrochemical efficiency or that photocorrosion proceeds from these locations.[43-48] This discrepancy in the role of edges is a major question that remains to be fully answered. Additionally, variations in photoelectrochemical efficiency within and among basal planes of exfoliated TMDs have been observed.[43,46,49]

1.2.2 1980s: Edge sites are recombination centers: Fact or fiction?

The working principles of bulk n-type TMD|I^-,I_3^-|Pt cells are as follows: (1) illumination produces electrons and holes in the semiconductor; (2) photogenerated holes move to the solid/liquid interface and react with surface-adsorbed iodide species ($2I^- + 2h^+ \rightarrow I_2$); (3) surface adsorbed iodine reacts with solution phase iodide to form tri-iodide ($I_2 + I^- \rightarrow I_3^-$); (4) photogenerated electrons extracted from the semiconductor move through the external circuit and reduce I_3^- at the Pt electrode.

In 1978, Gobrecht and Gerischer grew $MoSe_2$ crystals via vapor transport using Br_2 as the transport agent and reported a 3.5 % efficient photoelectrochemical solar cell in an iodide/tri-iodide electrolyte.[50] Tenne and Wold photoetched WSe_2 crystals in perchloric acid under positive

bias, creating a presumably "spongy" WO_3 surface that could be removed by immersing the crystal in hot KOH.[51] The significant performance enhancement (>14%-efficient cell) was attributed to less-reflective and well-defined sharp edges that did not contribute to recombination like native step-edges. These results suggest–step-edges have the capability of being either beneficial or detrimental to cell performance. Prasad and Srivastava photo-etched n-WSe_2 in aqua regia and reported a 17% efficient n-WSe_2|I^-,I_3^-|Pt cell with a high >32 mA/cm^2 short circuit current density.[52] Carefully cleaving crystals to achieve smooth surfaces, Kline et al. reported fill factors >0.75 in n-WSe_2|I^-,I_3^-|Pt cells.[44,53] They also showed that $MoSe_2$ cells could operate for over a month with no visible degradation of the electrode surface.[44]

Despite the outstanding performance of TMD|I^-,I_3^-|Pt cells, a consensus emerged that highly stepped or imperfect crystals produced lower photocurrents and fill factors than apparently smooth crystals.[44,46,50-53] Gerischer argued that Mo *d*-orbitals extended into the electrolyte at exposed step-edges and participated in electron exchange with tri-iodide species.[54] However, anecdotal evidence in literature suggests that crystal surface morphology alone could not explain performance variation among TMD|I^-,I_3^- cells. For example, Parkinson commented "some crystals which have areas apparently free of surface defects when observed with optical microscopy can still show considerable variation in carrier collection."[55] Bicelli and Razzini remarked "a layer-type semiconductor photoanode, which has an apparently defect-free, smooth surface, does not necessarily give high output characteristics, as is often assumed"[56] and, furthermore, "some crystals having smooth surfaces on a microscopic scale have much lower performance and that this cannot be improved through surface treatments."[57] These ensemble-level observations motivated spatially resolved photoelectrochemical studies to investigate the relationship between bulk crystal properties, surface morphology, and solar cell performance.

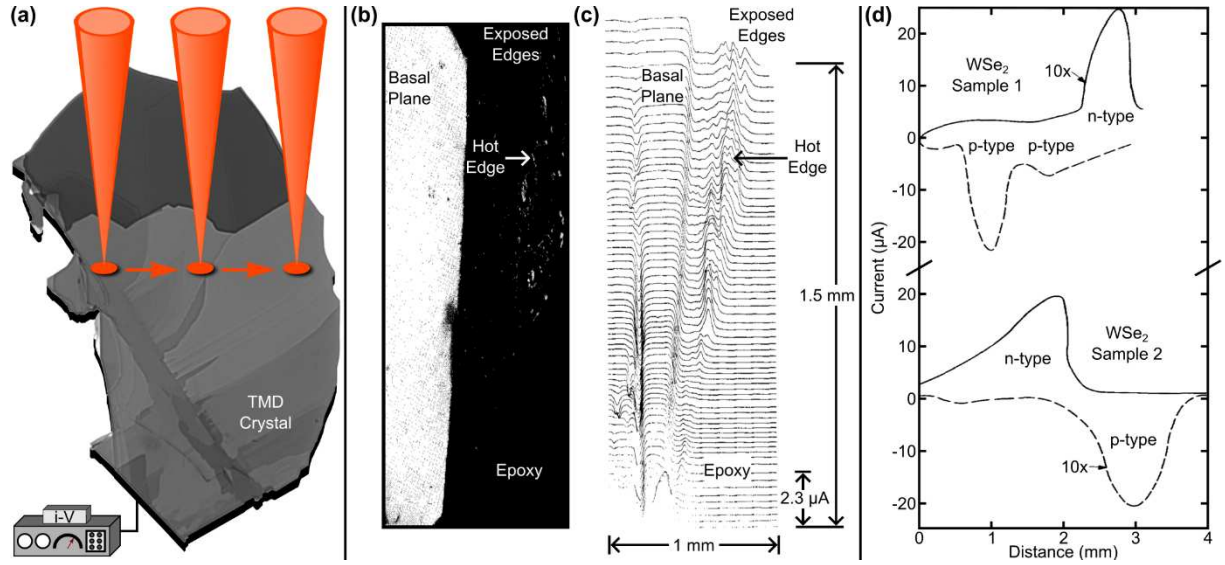

Figure 1.8: a) Cartoon illustration of scanning photocurrent microscopy of a TMD|I^-,I_3^- solar cell. The red light cones represent a focused laser spot moving across a TMD photoelectrode (e.g., MoS_2 or WSe_2). **b)** Photograph and **c)** photocurrent line scan data from a WSe_2|I^-,I_3^- with smooth and highly stepped regions. (c-d) Adapted from *J. Appl. Phys.* 51, 6018-6021 (1980), with the permission of AIP Publishing. **d)** Photocurrent line scan data from the same region of two different WSe_2 crystals. The solid line and dashed lines represent photocurrent measured at 0.1 and -1.4 V vs. $E_{I/I2}$, respectively. Adapted from *Appl. Phys. Lett.* 38, 949 (1981), with the permission of AIP Publishing.

In 1980, Furtak and Parkinson adapted spatially resolved carrier collection measurements for solid-state solar cells to n-GaAs and n-WSe_2 photoelectrochemical cells.[46] Figure 1.8a shows the general principle of scanning photocurrent microscopy measurements. By scanning a laser across a semiconducting sample, supra-bandgap illumination generates electrons and holes only within the illumination volume of the semiconductor. Typically, a potentiostat measures the total current at a fixed applied potential as a function of illumination position, yielding a photocurrent map. Those maps represent the total current flowing through the cell upon generating carriers in different microscopic regions of the crystal; the photocurrent map does not directly image where photogenerated electrons or holes react at the solid/electrolyte interface. The method does not

spatially resolve the dark current, therefore, neglecting local dark current contributions to the photocurrent response. Nonetheless, scanning photocurrent microscopy became a powerful technique to study how surface morphology affects performance of layered TMD while controlling the carrier generation location relative to a feature of interest (e.g., step-edges in Figure 1.8a).

Figure 1.8b,c shows the first example of scanning photocurrent microscopy data of a $WSe_2|I^-,I_3^-$ cell. The photocurrent line scans (Figure 1.8b) show high photocurrent in the smooth crystal regions (region A in Figure 1.8c) and generally low photocurrent in highly stepped areas (region B in Figure 1.8c), supporting the general literature hypothesis that recombination occurs at step-edges. Close examination of the dataset also shows that directly illuminating highly stepped sample regions can produce equivalent photocurrent magnitude as smooth basal planes, suggesting the existence of "hot edges" (see Figure 1.8c). However, A combination of the large light spot size (25 μm diameter) and inability to co-localize the photoelectrochemical data with the–local, illuminated surface structural features likely limited the authors' ability to resolve and elucidate the origin of step-edge performance variability.

Concomitantly, Menezes and Lewerenz applied scanning photocurrent microscopy to study performance variation among different specimens prepared from a single batch.[58] These samples ensemble-level electrochemical measurements revealed mixed n- and p-type crystals (even though all samples were prepared under the same reaction conditions). Figure 1.8d shows photocurrent line scan data at positive (solid line) and negative (dashed line) potentials from the same microscopic region of two different mixed n- and p-type crystals. The authors observed negligible anodic photocurrent from some regions of two different crystals under significant anodic bias even though whole-crystal illumination produced anodic photocurrent in ensemble-level current-voltage curve measurements. Under negative bias, the authors observed cathodic photocurrent in

the crystal regions that did not exhibit clear n-type behavior. However, the 60,000 μm^2 laser spot size, which is five orders of magnitude larger than near-diffraction limited laser spot sizes reported in the 2020s,[59-65] prevented the authors from characterizing the n- and p-type domain sizes and carrier generation-collection behavior near step-edges.

The spatially resolved photocurrent measurements in Figure 1.8 raised several interesting questions that could help to answer the critical question "Why do some smooth TMD crystals make bad solar cells?" Furtak and Parkinson's results (Figure 1.8b,c) showed directly illuminating some highly stepped regions of n-type crystals produced larger anodic photocurrents than smooth crystal regions. *Are step-edges recombination centers or highly active for iodide oxidation? Do n- and p-type domains exist within all TMD crystals? If mixed n- and p-type domains are generally present in TMD samples, how do neighboring n- and p-type domains affect carrier generation and transport behavior parallel to the layers?*

Photoelectrochemical microscopy is a technique that is well poised to address open questions in the 2D materials field. It allows for the relation of photoelectrochemical performance to surface structural features and the incorporation of other micro-spectroscopies like Raman microscopy or photoluminescence microscopy. The work presented in this dissertation utilizes photoelectrochemical microscopy in a number of ways to address open questions in the 2D materials community. With these methods, new knowledge is generated that will be beneficial to researchers looking to develop 2D materials for use in solar energy conversion devices.

1.2.3 Chapter Summaries

Each chapter contained in this dissertation is summarized below. The respective introduction sections for each chapter will clearly define the problem that will be studied.

Chapter 2 presents a study on the doping heterogeneity found among MoS_2 nanoflakes that were mechanically exfoliated from a natural crystal. The results detail the behavior and origin of n- and p-type domains that result from the doping heterogeneity. Additionally, an explanation is offered as to how the domains interact to result in the observed ensemble-level photoelectrochemical performance of a nanoflake electrode under illumination.

Chapter 3 contains a study on the phenomenon of iodine deposition on TMD materials, first discussed by Tributsch and co-workers in 1981. A molecular reaction imaging technique was used in combination with a novel image analysis algorithm to identify iodine deposition spots and relate them to underlying photoelectrochemical activity and surface motifs. This analysis procedure uncovered a surface recombination reaction relating to the movement of photogenerated holes.

Chapter 4 presents a mini-review on the use of different microscopy or scanning light spot methods to understand the origin of efficiency losses in TMD photoelectrochemical solar cells. The discussion walks through the historical literature and details the first use of a scanning-light spot measurement of a TMD crystal and an early report that discusses doping heterogeneity among the basal plane of a TMD crystal. Following that discussion, the mini-review discusses how these older methods were unable to provide answers to important questions and thus a number of loose ends or open questions were left relating to TMD materials. Modern methods that have the availability to provide answers to these questions are presented in two parts. Part 1 details scanning photocurrent microscopy methods and part 2 details new advancements in scanning electrochemical cell microscopy.

Chapter 5 presents data and results for a kinetic modelling study on the photocurrent measured during molecular reaction imaging experiments

REFERENCES

(1) Gerischer, H.; Kolb, D. M.; Sass, J. K. The Study of Solid Surfaces by Electrochemical Methods. *Advances in Physics* **1978**, *27* (3), 437–498. https://doi.org/10.1080/00018737800101424.

(2) Gerischer, H. Charge Transfer Processes at Semiconductor-Electrolyte Interfaces in Connection with Problems of Catalysis. *Surface Science* **1969**, *18* (1), 97–122. https://doi.org/10.1016/0039-6028(69)90269-6.

(3) Peter, L. M. Dynamic Aspects of Semiconductor Photoelectrochemistry. *Chem. Rev.* **1990**, *90* (5), 753–769. https://doi.org/10.1021/cr00103a005.

(4) Pleskov, Yu. V. Encyclopedia of Electrochemistry, Bard, A.J. and Stratmann, M., Eds., Vol. 6, Semiconductor Electrodes and Photoelectrochemistry, Licht, S., Ed., Weinheim: Wiley–VCH, 2002. *Russian Journal of Electrochemistry* **2003**, *39* (3), 328–330. https://doi.org/10.1023/A:1022896331878.

(5) Tan, M. X.; Laibinis, P. E.; Nguyen, S. T.; Kesselman, J. M.; Stanton, C. E.; Lewis, N. S. Principles and Applications of Semiconductor Photoelectrochemistry. In *Progress in Inorganic Chemistry*; John Wiley & Sons, Ltd, 1994; pp 21–144. https://doi.org/10.1002/9780470166420.ch2.

(6) Gärtner, W. W. Depletion-Layer Photoeffects in Semiconductors. *Phys. Rev.* **1959**, *116* (1), 84–87. https://doi.org/10.1103/PhysRev.116.84.

(7) Butler, M. A. Photoelectrolysis and Physical Properties of the Semiconducting Electrode WO2. *Journal of Applied Physics* **1977**, *48* (5), 1914–1920. https://doi.org/10.1063/1.323948.

(8) Etchebery, A.; Etman, M.; Fotouhi, B.; Gautron, J.; Sculfort, J.; Lemasson, P. Diffusion Length of Minority Carrier in N-type Semiconductors: A Photoelectrochemical Determination in Aqueous Solvents. *Journal of Applied Physics* **1982**, *53* (12), 8867–8873. https://doi.org/10.1063/1.330441.

(9) Lemasson, P.; Etcheberry, A.; Gautron, J. Analysis of Photocurrents at the Semiconductor—Eletrolyte Junction. *Electrochimica Acta* **1982**, *27* (5), 607–614. https://doi.org/10.1016/0013-4686(82)85048-2.

(10) Wang, L.; Schmid, M.; Sambur, J. B. Single Nanoparticle Photoelectrochemistry: What Is Next? *J. Chem. Phys.* **2019**, *151* (18), 180901. https://doi.org/10/ggp7cp.

(11) Peter, L. M.; Gurudayal; Wong, L. H.; Abdi, F. F. Understanding the Role of Nanostructuring in Photoelectrode Performance for Light-Driven Water Splitting. *Journal of Electroanalytical Chemistry* **2018**, *819*, 447–458. https://doi.org/10.1016/j.jelechem.2017.12.031.

(12) Albery, W. J.; Bartlett, P. N.; Hamnett, A.; Dare-Edwards, M. P. The Transport and Kinetics of Minority Carriers in Illuminated Semiconductor Electrodes. *J. Electrochem. Soc.* **1981**, *128* (7), 1492. https://doi.org/10.1149/1.2127670.

(13) Albery, W. J. The Transport and Kinetics of Photogenerated Carriers in Colloidal Semiconductor Electrode Particles. *Journal of The Electrochemical Society* **1984**, *131* (2), 315. https://doi.org/10.1149/1.2115568.

(14) Bisquert, J.; Garcia-Belmonte, G.; Fabregat-Santiago, F. Modelling the Electric Potential Distribution in the Dark in Nanoporous Semiconductor Electrodes. *J Solid State Electrochem* **1999**, *3* (6), 337–347. https://doi.org/10/dxhbz4.

(15) Yu, X.; Sivula, K. Photogenerated Charge Harvesting and Recombination in Photocathodes of Solvent-Exfoliated WSe2. *Chem. Mater.* **2017**, *29* (16), 6863–6875. https://doi.org/10/gbwv4z.
(16) Hill, J. W.; Hill, C. M. Directly Mapping Photoelectrochemical Behavior within Individual Transition Metal Dichalcogenide Nanosheets. *Nano Lett.* **2019**, *19* (8), 5710–5716. https://doi.org/10.1021/acs.nanolett.9b02336.
(17) Jiang, C.; Moniz, S. J. A.; Wang, A.; Zhang, T.; Tang, J. Photoelectrochemical Devices for Solar Water Splitting – Materials and Challenges. *Chem. Soc. Rev.* **2017**, *46* (15), 4645–4660. https://doi.org/10/gd32cr.
(18) Walter, M. G.; Warren, E. L.; McKone, J. R.; Boettcher, S. W.; Mi, Q.; Santori, E. A.; Lewis, N. S. Solar Water Splitting Cells. *Chemical Reviews* **2010**, *110* (11), 6446–6473. https://doi.org/10/bjxk7f.
(19) Nozik, A. J. Photoelectrochemistry: Applications to Solar Energy Conversion. *Annual Review of Physical Chemistry* **1978**, *29* (1), 189–222. https://doi.org/10/fptdnk.
(20) Bard, A. J. Design of Semiconductor Photoelectrochemical Systems for Solar Energy Conversion. *J. Phys. Chem.* **1982**, *86* (2), 172–177. https://doi.org/10.1021/j100391a008.
(21) Grätzel, M. Dye-Sensitized Solar Cells. *Journal of Photochemistry and Photobiology C: Photochemistry Reviews* **2003**, *4* (2), 145–153. https://doi.org/10.1016/S1389-5567(03)00026-1.
(22) Song, H.; Luo, S.; Huang, H.; Deng, B.; Ye, J. Solar-Driven Hydrogen Production: Recent Advances, Challenges, and Future Perspectives. *ACS Energy Lett.* **2022**, *7* (3), 1043–1065. https://doi.org/10.1021/acsenergylett.1c02591.
(23) *Best Research-Cell Efficiency Chart*. Nationable Renewable Energy Laboratory. https://www.nrel.gov/pv/cell-efficiency.html (accessed 2022-09-20).
(24) Kamat, P. V. Meeting the Clean Energy Demand: Nanostructure Architectures for Solar Energy Conversion. *J. Phys. Chem. C* **2007**, *111* (7), 2834–2860. https://doi.org/10.1021/jp066952u.
(25) Bernardi, M.; Palummo, M.; Grossman, J. C. Extraordinary Sunlight Absorption and One Nanometer Thick Photovoltaics Using Two-Dimensional Monolayer Materials. *Nano Lett.* **2013**, *13* (8), 3664–3670. https://doi.org/10.1021/nl401544y.
(26) Velický, M.; Toth, P. S. From Two-Dimensional Materials to Their Heterostructures: An Electrochemist's Perspective. *Applied Materials Today* **2017**, *8*, 68–103. https://doi.org/10/ggssfs.
(27) Tributsch, H. Electrochemical Solar Cells Based on Layer-Type Transition Metal Compounds: Performance of Electrode Material. *Sol. Energy Mater.* **1979**, *1* (3), 257–269. https://doi.org/10.1016/0165-1633(79)90044-3.
(28) Lu, Q.; Yu, Y.; Ma, Q.; Chen, B.; Zhang, H. 2D Transition-Metal-Dichalcogenide-Nanosheet-Based Composites for Photocatalytic and Electrocatalytic Hydrogen Evolution Reactions. *Advanced Materials* **2016**, *28* (10), 1917–1933. https://doi.org/10/f3kcd5.
(29) Tributsch, H. Solar Energy-Assisted Electrochemical Splitting of Water. Some Energetical, Kinetical and Catalytical Considerations Verified on MoS2 Layer Crystal Surfaces. *Z. Naturforsch. A.* **1977**, *32* (9), 972–985. https://doi.org/10/ggp7h7.
(30) Yu, X.; Sivula, K. Toward Large-Area Solar Energy Conversion with Semiconducting 2D Transition Metal Dichalcogenides. *ACS Energy Lett.* **2016**, *1* (1), 315–322. https://doi.org/10.1021/acsenergylett.6b00114.

(31) Novoselov, K. S.; Jiang, D.; Schedin, F.; Booth, T. J.; Khotkevich, V. V.; Morozov, S. V.; Geim, A. K. Two-Dimensional Atomic Crystals. *Proceedings of the National Academy of Sciences* **2005**, *102* (30), 10451–10453. https://doi.org/10.1073/pnas.0502848102.
(32) Geim, A. K.; Novoselov, K. S. The Rise of Graphene. *Nature Mater* **2007**, *6* (3), 183–191. https://doi.org/10.1038/nmat1849.
(33) Splendiani, A.; Sun, L.; Zhang, Y.; Li, T.; Kim, J.; Chim, C.-Y.; Galli, G.; Wang, F. Emerging Photoluminescence in Monolayer MoS2. *Nano Lett.* **2010**, *10* (4), 1271–1275. https://doi.org/10.1021/nl903868w.
(34) Britnell, L.; Ribeiro, R. M.; Eckmann, A.; Jalil, R.; Belle, B. D.; Mishchenko, A.; Kim, Y.-J.; Gorbachev, R. V.; Georgiou, T.; Morozov, S. V.; Grigorenko, A. N.; Geim, A. K.; Casiraghi, C.; Neto, A. H. C.; Novoselov, K. S. Strong Light-Matter Interactions in Heterostructures of Atomically Thin Films. *Science* **2013**, *340* (6138), 1311–1314. https://doi.org/10.1126/science.1235547.
(35) Yu, X.; Prévot, M. S.; Guijarro, N.; Sivula, K. Self-Assembled 2D WSe 2 Thin Films for Photoelectrochemical Hydrogen Production. *Nat Commun* **2015**, *6* (1), 7596. https://doi.org/10.1038/ncomms8596.
(36) Li, C.; Cao, Q.; Wang, F.; Xiao, Y.; Li, Y.; Delaunay, J.-J.; Zhu, H. Engineering Graphene and TMDs Based van Der Waals Heterostructures for Photovoltaic and Photoelectrochemical Solar Energy Conversion. *Chem. Soc. Rev.* **2018**, *47* (13), 4981–5037. https://doi.org/10.1039/C8CS00067K.
(37) Furchi, M. M.; Pospischil, A.; Libisch, F.; Burgdörfer, J.; Mueller, T. Photovoltaic Effect in an Electrically Tunable van Der Waals Heterojunction. *Nano Lett.* **2014**, *14* (8), 4785–4791. https://doi.org/10.1021/nl501962c.
(38) Chen, Z.; Jaramillo, T. F.; Deutsch, T. G.; Kleiman-Shwarsctein, A.; Forman, A. J.; Gaillard, N.; Garland, R.; Takanabe, K.; Heske, C.; Sunkara, M.; McFarland, E. W.; Domen, K.; Miller, E. L.; Turner, J. A.; Dinh, H. N. Accelerating Materials Development for Photoelectrochemical Hydrogen Production: Standards for Methods, Definitions, and Reporting Protocols. *Journal of Materials Research* **2010**, *25* (1), 3–16. https://doi.org/10.1557/JMR.2010.0020.
(39) Jaramillo, T. F.; Jørgensen, K. P.; Bonde, J.; Nielsen, J. H.; Horch, S.; Chorkendorff, I. Identification of Active Edge Sites for Electrochemical H2 Evolution from MoS2 Nanocatalysts. *Science* **2007**, *317* (5834), 100–102. https://doi.org/10.1126/science.1141483.
(40) Salvador, P.; Chaparro, A. M.; Mir, A. Digital Imaging of the Effect of Photoetching on the Photoresponse of N-Type Tungsten Diselenide and Molybdenum Diselenide Single Crystal Electrodes. *J. Phys. Chem.* **1996**, *100* (2), 760–768. https://doi.org/10/fhvs5p.
(41) Chaparro, A. M.; Salvador, P.; Peter, L. M. The Role of Surface Defects in the Photooxidation of Iodide at N-MoSe2: Evidence for a Local "Autocatalytic" Effect. *J. Phys. Chem.* **1995**, *99* (17), 6677–6683. https://doi.org/10.1021/j100017a059.
(42) Chaparro, A. M.; Salvador, P.; Tabernero, A.; Navarro, R.; Coll, B.; Caselles, V. Charge Recombination Imaging at the WSe2/I− Interface. *Surface Science* **1993**, *295* (3), 457–461. https://doi.org/10/ctpm9k.
(43) Lewerenz, H. J.; Heller, A.; DiSalvo, F. J. Relationship between Surface Morphology and Solar Conversion Efficiency of Tungsten Diselenide Photoanodes. *J. Am. Chem. Soc.* **1980**, *102* (6), 1877–1880. https://doi.org/10/b52hqq.
(44) Kline, G.; Kam, K.; Canfield, D.; Parkinson, B. A. Efficient and Stable Photoelectrochemical Cells Constructed with WSe2 and MoSe2 Photoanodes. *Sol. Energy Mater.* **1981**, *4* (3), 301–308. https://doi.org/10/d87x7q.

(45) Kautek, W.; Gerischer, H. Anisotropic Photocorrosion of N-Type MoS2 MoSe2, and WSe2 Single Crystal Surfaces: The Role 0f Cleavage Steps, Line and Screw Dislocations. *Surface Science* **1982**, *119* (1), 46–60. https://doi.org/10/fcmw2m.
(46) Furtak, T. E.; Canfield, D. C.; Parkinson, B. A. Scanning Light-spot Analysis of the Carrier Collection in Liquid-junction Solar Energy Converters. *J. Appl. Phys.* **1980**, *51* (11), 6018–6021. https://doi.org/10/fvdfk5.
(47) Kam, K. K.; Parkinson, B. A. Detailed Photocurrent Spectroscopy of the Semiconducting Group VIB Transition Metal Dichalcogenides. *J. Phys. Chem.* **1982**, *86* (4), 463–467. https://doi.org/10/fsccvh.
(48) Gerischer, H.; Roß, D.; Lübke, M. Electrochemistry of N-Type MoSe2: A Comparison of Photocorrosion and Dissolution under High Anodic Bias. *Zeitschrift für Physikalische Chemie* **1984**, *139* (139), 1–9. https://doi.org/10/fgpxvp.
(49) Bicelli, L. P.; Razzini, G. Surface Defects on N-MoSe2 Electrodes Used in Photoelectrochemical Solar Cells. *Surface Technology* **1983**, *20* (4), 383–392. https://doi.org/10.1016/0376-4583(83)90116-4.
(50) Gobrecht, J.; Tributsch, H.; Gerischer, H. Performance of Synthetical N-MoSe2 in Electrochemical Solar Cells. *J. Electrochem. Soc.* **1978**, *125* (12), 2085. https://doi.org/10/ddtbz9.
(51) Tenne, R.; Wold, A. Passivation of Recombination Centers in N-WSe2 Yields High Efficiency (>14%) Photoelectrochemical Cell. *Appl. Phys. Lett.* **1985**, *47* (7), 707–709. https://doi.org/10/fcxrk9.
(52) Prasad, G.; Srivastava, O. N. The High-Efficiency (17.1%) WSe2photo-Electrochemical Solar Cell. *J. Phys. D: Appl. Phys.* **1988**, *21* (6), 1028–1030. https://doi.org/10/c7k5qr.
(53) Kline, G.; Kam, K. K.; Ziegler, R.; Parkinson, B. A. Further Studies of the Photoelectrochemical Properties of the Group VI Transition Metal Dichalcogenides. *Solar Energy Materials* **1982**, *6* (3), 337–350. https://doi.org/10.1016/0165-1633(82)90039-9.
(54) Ahmed, S. M.; Gerischer, H. Influence of Crystal Surface Orientation on Redox Reactions at Semiconducting MoS2. *Electrochimica Acta* **1979**, *24* (6), 705–711. https://doi.org/10.1016/0013-4686(79)87055-3.
(55) Parkinson, B. A.; Furtak, T. E.; Canfield, D.; Kam, K.-K.; Kline, G. Evaluation and Reduction of Efficiency Losses at Tungsten Diselenide Photoanodes. *Faraday Discuss. Chem. Soc.* **1980**, *70* (0), 233–245. https://doi.org/10/cg82t4.
(56) Razzini, G. Photocatalytic Behaviour of N-MoSe2 Single Crystals in Contact with the I−, I2 Redox Couple in Solar Photo-Electrochemical Cells. *Journal of Power Sources* **1982**, *7* (3), 275–280. https://doi.org/10.1016/0378-7753(82)80016-5.
(57) Bicelli, L. P.; Razzini, G. Surface Behaviour of N-MoSe2 Photoanodes in Photoelectrochemical Solar Cells. *Surface Technology* **1982**, *16* (1), 37–47. https://doi.org/10.1016/0376-4583(82)90093-0.
(58) Menezes, S.; Schneemeyer, L. F.; Lewerenz, H. J. Efficiency Losses from Carrier-type Inhomogeneity in Tungsten Diselenide Photoelectrodes. *Appl. Phys. Lett.* **1981**, *38* (11), 949–951. https://doi.org/10/bpmvbx.
(59) M. Velazquez, J.; John, J.; V. Esposito, D.; Pieterick, A.; Pala, R.; Sun, G.; Zhou, X.; Huang, Z.; Ardo, S.; P. Soriaga, M.; S. Brunschwig, B.; S. Lewis, N. A Scanning Probe Investigation of the Role of Surface Motifs in the Behavior of P-WSe 2 Photocathodes. *Energy Environ. Sci.* **2015**, *9* (1), 164–175. https://doi.org/10/ggpvh4.

(60) Todt, M. A.; Isenberg, A. E.; Nanayakkara, S. U.; Miller, E. M.; Sambur, J. B. Single-Nanoflake Photo-Electrochemistry Reveals Champion and Spectator Flakes in Exfoliated MoSe2 Films. *J. Phys. Chem. C* **2018**, *122* (12), 6539–6545. https://doi.org/10/gdc6df.
(61) Isenberg, A. E.; Todt, M. A.; Wang, L.; Sambur, J. B. Role of Photogenerated Iodine on the Energy-Conversion Properties of MoSe2 Nanoflake Liquid Junction Photovoltaics. *ACS Appl. Mater. Interfaces* **2018**, *10* (33), 27780–27786. https://doi.org/10.1021/acsami.8b07617.
(62) Erdewyk, M. V.; Sambur, J. B. Single Nanoflake Photoelectrochemistry Reveals Intrananoflake Doping Heterogeneity That Explains Ensemble-Level Photoelectrochemical Behavior. *ACS Appl. Mater. Interfaces* **2022**, *14* (20), 22737–22746. https://doi.org/10.1021/acsami.1c14928.
(63) Wang, L.; Sambur, J. B. Efficient Ultrathin Liquid Junction Photovoltaics Based on Transition Metal Dichalcogenides. *Nano Lett.* **2019**, *19* (5), 2960–2967. https://doi.org/10/gf2wsk.
(64) Wang, L.; Schmid, M.; Nilsson, Z. N.; Tahir, M.; Chen, H.; Sambur, J. B. Laser Annealing Improves the Photoelectrochemical Activity of Ultrathin MoSe2 Photoelectrodes. *ACS Appl. Mater. Interfaces* **2019**, *11* (21), 19207–19217. https://doi.org/10/ggp7cq.
(65) Wang, L.; Tahir, M.; Chen, H.; Sambur, J. B. Probing Charge Carrier Transport and Recombination Pathways in Monolayer MoS2/WS2 Heterojunction Photoelectrodes. *Nano Letters* **2019**. https://doi.org/10/ggp65d.

CHAPTER 2: SINGLE NANOFLAKE PHOTOELECTROCHEMISTRY REVEALS INTRA-NANOFLAKE DOPING HETEROGENEITY THAT EXPLAINS ENSEMBLE-LEVEL PHOTOELECTROCHEMICAL BEHAVIOR[ii]

2.1 Introduction

Transition metal dichalcogenides (TMDs) such as WSe_2 and MoS_2 are promising light harvesting materials for photoelectrochemical (PEC) solar energy conversion applications because they exhibit long-term stability[11] and nearly optimum band gaps for solar photon capture.[4,7,10,13] One advantage of their layered crystal structure is bulk TMDs can be exfoliated into two-dimensional (2D) nanoflakes and then processed into large area thin film photoelectrodes.[1,18,19] For example, Wells et al. demonstrated a high-throughput roll-to-roll deposition process that first exfoliates MoS_2 nanoflakes from commercially available powders using solvents and then deposits 10 cm-wide films on electrode surfaces.[20] Advances in mechanical exfoliation have also led to the production of high quality macroscopic monolayers and artificial heterostructures,[21,22] which opens the exciting possibility of creating macroscopic p-n junctions with controllable properties defined by the parent bulk material. Hence, the 2D materials community is advancing large-scale production methods for potentially low-cost and high-performance thin film photoelectrodes.

Unfortunately, TMD nanoflake thin films have not achieved the same photoelectrochemical performance as bulk TMDs. In the 1980s, several groups demonstrated efficient bulk TMD|I^-,I_2|Pt PEC solar cells.[11,7,5,23] The PEC solar cells achieved >70% internal quantum efficiency (IQE) at zero applied bias and maintained >10% power conversion efficiency

[ii] This chapter was published previously as: Van Erdewyk, M.; Sambur, J.B.; "Single nanoflake photoelectrochemistry reveals intra-nanoflake doping heterogeneity that explains ensemble-level photoelectrochemical behavior" *ACS Appl. Mater. Interfaces,* **2022**, 14, 20, 22737–22746

for over one month of continuous operation.[11,13] On the other hand, TMD nanoflake photoelectrodes produce much lower photocurrent densities for the same iodide oxidation reaction even under applied bias (e.g., uniform 0.26 cm^2 MoS_2/WSe_2 nanoflake electrodes produced 40 μA cm^{-2} under 100 mW/cm^2 illumination[20] whereas 0.05 cm^2 bulk MoS_2, WS_2, and WSe_2 electrodes produced 6-10 mA/cm^2 under 80-90 mW/cm^2 illumination[24]). Bulk TMDs[25] also out-perform nanoflakes in the PEC hydrogen evolution reaction.[26,27] Light absorption differences between bulk and nanoflake photoelectrodes cannot fully account for the significant performance gap.[1]

One likely contribution to the poor performance of nanoflake photoelectrodes is the high number of exposed defect and edge sites after the exfoliation process.[27,28] Exposed edge sites of TMD photoanodes were identified as potent recombination centers decades ago.[10,13,8,29–35] Specific chemical treatments have been developed to mitigate charge carrier recombination at edge sites on both bulk and nanoflake electrodes.[13,27,36–38]

Considerably less attention has been paid to PEC performance variation among apparently smooth basal planes within single nanoflakes. Velický et. al. discovered layer thickness and light intensity influenced the PEC performance of basal planes within mono- and few-layer MoS_2 nanoflakes.[39] Todt et al. attributed the heterogeneous activity of different basal planes to surface defects and impurities.[28] Additional single nanoflake-level PEC and electrocatalytic measurements reported performance variations among different basal planes on the same nanoflake.[40–43] However, the materials chemistry origin of PEC performance variation among nanoflake basal planes has not been elucidated.

One possible explanation for PEC performance variation among apparently smooth basal planes is doping heterogeneity. Hill and co-workers observed anodic to cathodic photocurrent switching behavior for different basal planes of single nanoflakes,[40] suggesting doping

heterogeneity exists within the flake. In the early 1980s, Menezes and Lewerenz reported doping heterogeneity limits the photoelectrochemical efficiency of synthetic bulk TMD crystals.[17,44] Similarly, Kline and Parkinson provided some evidence that bulk MoS_2 and WSe_2 photoelectrodes with ideal stoichiometry exhibited better photovoltage, open-circuit potential, and fill factor than crystals with non-ideal stoichiometry.[24] Spatially resolved PEC measurements of bulk TMD crystals revealed similar results.[16,34,45] Lewis and co-workers reported the external quantum yield of different basal planes on p-WSe_2 varied due to differences in local electronic structure.[34] Hence, there is significant literature precedent that doping heterogeneity in bulk TMD materials can transfer to individual nanoflakes and limit PEC performance.

In this study, we test the literature-based hypothesis that doping heterogeneity limits PEC performance of exfoliated nanoflake photoelectrodes. To test this hypothesis, we compared the PEC performance of MoS_2 nanoflakes that were mechanically exfoliated from two widely used commercial sources: synthetic n-type Re-doped MoS_2 from 2D Semiconductor (https://www.2dsemiconductors.com/n-type-mos2/) and naturally occurring MoS_2 from SPI (https://www.2spi.com/item/z429ml/). All 21 Re-doped MoS_2 nanoflakes were efficient n-type photoanodes for iodide oxidation (IQE values exceeded 80%), confirming the ensemble-level result that the Re-doped MoS_2 nanoflake thin film produced larger photocurrents than the natural MoS_2 nanoflake film. On the other hand, photocurrent mapping and local photocurrent-potential (*i*-*E*) measurements of natural MoS_2 nanoflakes revealed the presence of n- and p-type domains within the same nanoflake. Interestingly, the n- and p-type domains were efficient for iodide oxidation and tri-iodide reduction, respectively (IQE values within single flakes exceed 80%). The single nanoflake-level *i*-*E* measurements explain the poor ensemble-level photocurrent from the natural MoS_2 nanoflake sample: the n- and p-type diode currents from individual domains oppose

each other upon illuminating the entire nanoflake, resulting in a negligible total photocurrent. While this doping heterogeneity effect limits photoanode or photocathode performance, these findings open the possibility to synthesize TMD nanoflakes with lateral p- and n-type domains for photocatalytic applications.

2.2 Experimental Methods

2.2.1 Electrode preparation and ensemble-level electrochemical measurements

MoS_2 nanoflake-coated ITO electrodes were prepared by mechanical exfoliation of commercially available bulk MoS_2 crystals: Re-doped n-type MoS_2 (2D semiconductors, BLK-MoS2-N, doping density 10^{17}-10^{18} cm^{-3}) and naturally occurring bulk MoS2 (SPI, 470MOS2L-AB). In a typical mechanical exfoliation procedure, low residue Nitto tape (BT-150E-CM, Nitto) was manually pressed onto the surface of bulk crystals for 10 min and then gently removed. Gentle, manual pressure was applied to the crystal surface to remove air bubbles. A commercially available gel-film (Gelfilm from Gelpak)[46] was used to transfer exfoliated MoS_2 from the Nitto tape to a pre-cleaned ITO electrode (4-10 Ω, 25 × 75 × 1.1 mm, Delta Technologies). The ITO cleaning procedure is provided in our previous study.[28] The nanoflake-coated ITO electrodes were assembled into a 3-electrode electrochemical flow cell as described previously.[28] A Pt wire served as the counter electrode and a Ag/AgI wire was used as the reference electrode. All ensemble-level photoelectrochemical measurements of MoS_2 nanoflake-coated ITO electrodes were performed in 1 M NaI/1 mM I_2 electrolytes. Electrochemical measurements with a polished 7 mm^2 glassy carbon (GC) disc electrode (CHI Instruments, CHI104) were performed in 3 mM NaI electrolyte. An Ivium potentiostat (CompactStat.h) measured current-voltage curves in a three-electrode configuration. An 8 mW 530 nm LED (ThorLabs, M530L3) illuminated the nanoflake films for ensemble-level measurements.

2.2.2 Scanning photoelectrochemical microscopy

The electrochemical flow cells were mounted on an Olympus IX73 inverted microscope equipped with confocal Raman and photoelectrochemical mapping capabilities.[28,47] In this study, 0.30 – 0.7 mW 415 nm laser light (Oxxius, LBX-415-120-CSB-PPA) was directed through the back port of the microscope, reflected by a 414 nm dichroic mirror (Edmund Optics, 86330) in the filter cube, and aligned on the back aperture of a 60× objective (UPLANSAPO60x/W), yielding a 0.86 mm diameter laser spot (as determined by a knife-edge scan in Figure S2.1) and a laser power density of 52 - 121 W/cm^2. All photoelectrochemical mapping experiments were performed at fixed 0.600 V vs. Ag/AgI while 1 M NaI/1 mM I_2 electrolyte was flowed through the cell at a rate of 25 mL/min. The total current from the electrochemical cell was measured by an Ivium CompactStat potentiostat. The analog current output from the potentiostat was measured by a Measurement Computing Data Acquisition card (USB-1608FS-Plus) at a rate of 25 Hz. At the same time, the DAQ card measured the XY stage position (Marzhauzer SCANplus IM). The typical step size for mapping experiments was 1 mm. The step size was adjusted to 2 mm for large area nanoflakes (e.g., >6000 mm^2). The photocurrent value at each stage position (i.e., pixel) represents the averaging current during a 400 ms time period, corresponding to 10 data points. The average current from the ITO background pixels was subtracted from the current at each illumination nanoflake location. We correlate the photocurrent and structural images of nanoflakes using our correlated laser reflection-photocurrent mapping procedure (details may be found in the Supplementary Information of ref [48]). Supplemental Information Note 1 of this work describes the detailed image analysis procedures to calculate IQE values from the EQE maps.

2.2.3 Local photocurrent-potential measurements

A focused 415 nm laser spot excited 2.3 mm^2 areas of single nanoflakes to measure local *i-E* curves. A lock-in detection scheme was used to sensitively measure the photo-induced current from single nanoflakes. In a typical local photocurrent-voltage curve measurement, the excitation laser was chopped at 37 Hz to induce a modulating photocurrent due to iodide oxidation or tri-iodide reduction. The chopper frequency (TTI-C995) and the analog current output from the potentiostat were fed into a Stanford Research Systems SR830 lock-in amplifier. The lock-in detected current was measured at a fixed applied potential and averaged over an 8 s period. The measurement was repeated in 3 mV increments. The signal from the lock-in was converted from arbitrary units to ampere units by determining the proportional constant from direct current measurements.

2.2.4 XPS characterization

Re-MoS_2 and SPI-MoS_2 crystals were freshly cleaved using double-sided conductive carbon tape (Nisshin-EM). The MoS_2-coated tape samples were analyzed in a PHI PE-5800 X-ray photoelectron spectroscopy (XPS) system. High resolution XPS spectra of the C, Mo, and S regions were acquired at multiple locations on each sample using an 800 mm^2 aperture. The spectra were analyzed with PHI Multipak software. The Mo 3d peaks were fit with two mixed Gaussian-Lorentzian peak shapes at a fixed peak separation of 3.13 eV. The S 2p peaks were fit with two mixed Gaussian-Lorentzian peak shapes at a fixed peak separation of 1.1 eV. The C 1s peak was used to correct each spectrum for charging effects.

2.2.5 Elemental analysis

Re-MoS_2 and SPI-MoS_2 were immersed in a vial containing aqueous 3 M HNO_3 solution and the vial was placed in a water bath at 40°C for 4 days. Mo and S concentrations in each sample

were determined via inductively coupled plasma-atomic emission spectroscopy (ICP-AES) analysis of the acidic solutions (Perkin Elmer, Optima 7300 DV).

2.2.6 Electron Microscopy

The morphology of exfoliated Re-MoS_2 and SPI-MoS_2 samples were analyzed using scanning electron microscopy (SEM) and energy dispersive x-ray spectroscopy (EDS) in a JEOL 6500 FE-SEM electron microscope. SEM imaging and EDS spectroscopy were acquired with 2 keV and 15 keV accelerating voltages, respectively.

2.3 Results

2.3.1 Photoelectrochemical characterization

Synthetic n-type Re-doped MoS_2 and naturally occurring MoS_2 crystals were purchased from 2Dsemiconductors and SPI Supplies, respectively. The crystals were mechanically exfoliated using low residue Nitto Tape and transferred to ITO electrodes with a commercially available gel-film.[46] We refer to these nanoflake-coated ITO electrodes as Re-MoS_2 and SPI-MoS_2. Figure 2.a-b shows representative optical transmission images of the Re-MoS_2 and SPI-MoS_2 samples as well as the parent bulk crystals (additional images provided in Figure S2.2). Mechanical exfoliation produces a heterogeneous distribution of nanoflakes ranging from 25-210 mm in diameter and 15-70 nm in thickness. Supplementary Information Note 2 describes the procedure for thickness determination. The heterogeneous nanoflake population motivates our single nanoflake-level PEC approach, which allows us to quantitatively compare IQE values of individual Re-MoS_2 and SPI-MoS_2 nanoflakes that have different light absorption properties.

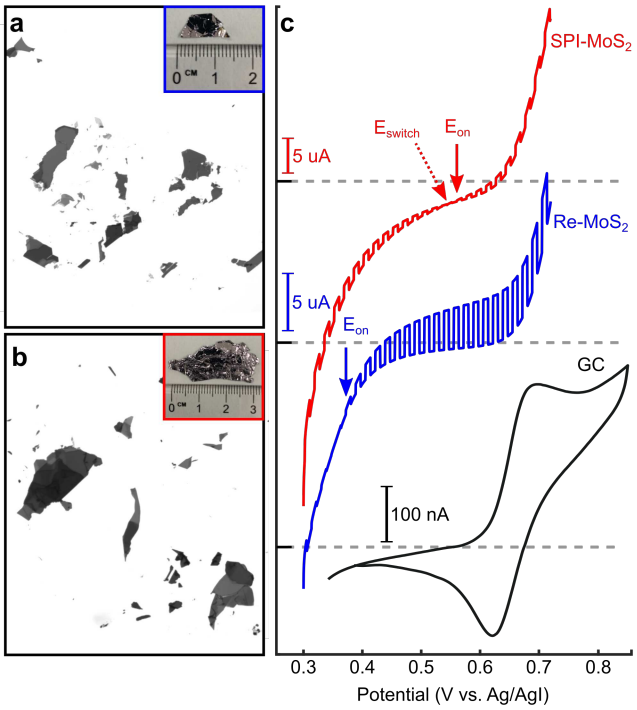

Figure 2.1. Optical and ensemble-level photoelectrochemical characterization of MoS_2 nanoflake photoelectrodes. Optical transmission images of (a) Re-MoS_2 and (b) SPI-MoS_2. Insets show photographs of the parent bulk crystals. (c) LSV of Re-MoS_2 (blue) and SPI-MoS_2 (red) nanoflake films in aqueous 1 M NaI/1mM I_2 electrolyte and under chopped light illumination (8 mW 532 nm LED illuminating a 2.5 cm^2 area). The black line represents a polished glassy carbon (GC) disk working electrode under dark conditions. The vertical red and blue arrows indicate the photocurrent onset potential (E_{on}).

Figure 2.c shows current-potential measurements of SPI-MoS_2 (top) and Re-MoS_2 (middle) in aqueous 1 M NaI/1mM I_2 electrolyte under chopped light conditions. The anodic photocurrent for both samples increases with increasing positive potential, consistent with n-type semiconducting behavior.[11,30] The anodic photocurrent onset potential (E_{on}) of Re-MoS_2 and SPI-MoS_2 samples were 0.39 and 0.56 V vs Ag/AgI, respectively (indicated by vertical arrows in Figure 2.c). These E_{on} values occur at more negative potentials than the iodide oxidation reaction on a polished GC disk electrode (Figure 2.c, black trace). We also observed an anodic-to-cathodic photocurrent switching effect for SPI-MoS_2 (indicated by E_{switch} in Figure 2.c-top). For potentials more negative than E_{switch}, SPI-MoS_2 exhibits an increasing cathodic photocurrent with increasing negative

potential, consistent with p-type semiconducting behavior. This photocurrent switching has previously been shown for natural MoS_2 by Chen et al.[49] Interpretating the ensemble-level observations in Figure 2.c-top is challenging because the measurements do not reveal what fraction of SPI-MoS_2 nanoflakes are either n-type, p-type, or both. In this work, we use single nanoflake-level PEC measurements to address the sample heterogeneity issue and explore the origin of the n- and p-type photocurrent response in SPI-MoS_2.

In a typical single nanoflake PEC experiment, a 415 nm laser excites a 0.86 mm-diameter spot on the nanoflake-coated ITO electrode while a potentiostat measures the current of the entire electrochemical cell as a function of laser illumination position. We chose to map the photocurrent at fixed 0.600 V vs Ag/AgI because the photocurrent reaches a light-limited and potential-independent value at this potential, evidenced by local *i-E* measurements below. IQE mapping with the 415 laser measures charge separation and collection efficiency of photogenerated electrons in the space charge region at the solid-liquid interface because the penetration depth (d) of the 415 nm light is 10 nm ($d = 1/\alpha(\lambda)$ and $\alpha(415\text{ nm}) = 9\times10^5\text{ cm}^{-1}$)[50] and we estimate from the Mott-Schottky equation that the space charge region thickness is 20 nm at an applied potential of 0.21 V versus the flatband potential (E-E_{fb}) and a doping density of $5'10^{17}\text{ cm}^{-3}$.

Figure 2.a-d shows representative optical images and photocurrent mapping results from a single 45 nm-thick Re-MoS_2 nanoflake under 415 nm excitation. The optical transmission images reveal differences in flake thickness (Figure 2.a) whereas the reflection contrast reveals variations in surface step features (Figure 2.b). Comparing the reflection and transmission images to the IQE map in Figure 2.c reveals how nanoflake structural properties influence the photocurrent response: the photocurrent is uniform within a single basal plane and decreases when the laser spot moves across step edges. In addition, the dark red contrast at the nanoflake perimeter indicates lower

anodic photocurrents at perimeter edge sites. Hence, illuminated edge sites produce lower anodic photocurrents, in agreement with previous spatially resolved measurements of bulk n-type WSe_2, WS_2, and $MoSe_2$ photoelectrodes that showed edge sites are recombination centers in iodide-based electrolytes.[43,51] Figure 2.d shows the IQE distribution from the nanoflake in Figure 2.a-c. The average IQE value is 55.0 ± 8.0 % (S.D.), in agreement with IQE values for n-type WSe_2 single crystals reported by Kline and Parkinson.[11] We observed similarly high IQE values for other nanoflakes within the same film (Figure 2.e-h). The average IQE from 21 nanoflakes studied herein was 38.2 ± 15.3 % (Figure S2.3). We note that our group previously mapped 53 mechanically exfoliated $MoSe_2$ nanoflakes and observed 66% of nanoflakes were inactive "spectators",[28] meaning the flakes did not produce a photocurrent larger than the indium tin oxide (ITO) substrate. In that study, we hypothesized that poor electrical contact between $MoSe_2$ nanoflakes and ITO substrate was responsible for the large spectator population. The results in Figure 2. suggest that poor electrical contact cannot entirely account for the large population of inactive $MoSe_2$ nanoflakes because all active Re-MoS_2 nanoflakes in this work share the same contact with the ITO substrate in the $MoSe_2$ study. This work explores an alternative hypothesis to explain the origin of poor photocurrent collection efficiency in mechanically exfoliated nanoflakes: doping heterogeneity in the parent material limits PEC performance.

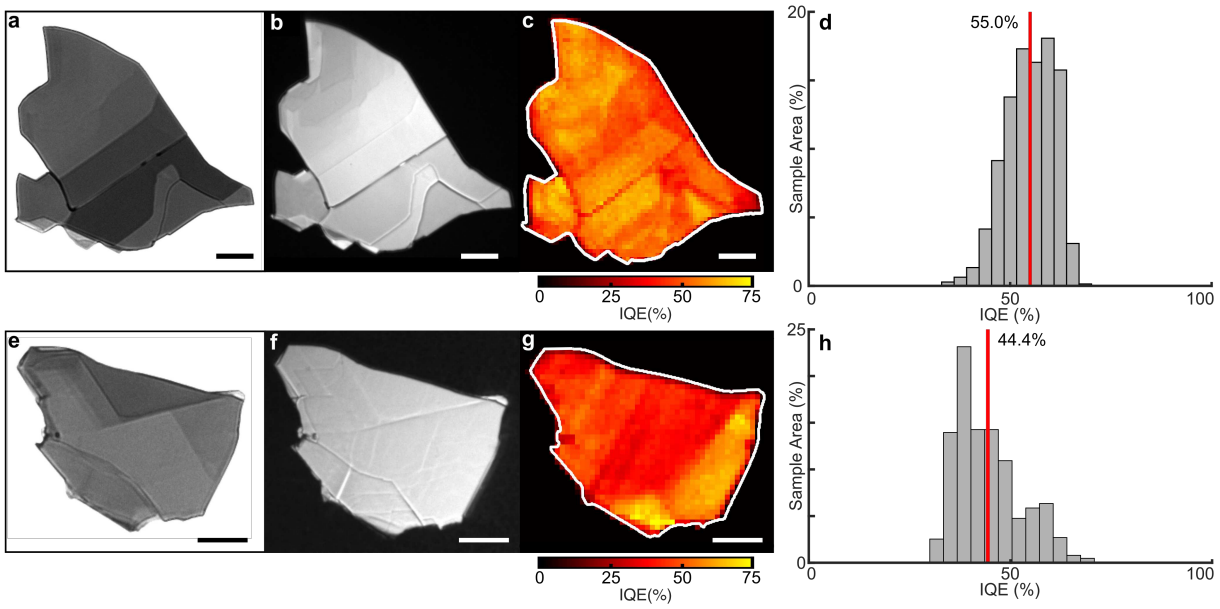

Figure 2.2. Single nanoflake photoelectrochemical measurements of Re-MoS_2. (a) Bright field transmission image, (b) reflection image, and (c) IQE map of a 45 nm-thick nanoflake. The IQE map was measured at +0.600 V vs Ag/AgI in aqueous 1 M NaI/1mM I_2 electrolyte using a 860 nm-diameter 0.50 mW 415 nm laser. (d) Histogram of IQE values from the IQE map in (c). (e-h) same as (a-d), but for a 48 nm-thick Re-MoS_2 nanoflake. All scale bars represent 10 mm.

Photocurrent mapping experiments of SPI-MoS_2 nanoflakes revealed strikingly different photoelectrochemical behavior than the Re-MoS_2 nanoflakes. We classified SPI-MoS_2 nanoflake behaviors into three categories: (1) dominant n-type behavior, (2) dominant p-type behavior, and (3) mixed n- and p-type behavior. The categories were quantitatively based on the area fraction of a nanoflake that exhibited an n- or p-type photocurrent response. We defined dominant n-type behavior as >75% of the nanoflake area producing EQE values >1%. Figure 2.a shows representative photocurrent mapping results of an n-type SPI-MoS_2 nanoflake. The nanoflake exhibits uniform n-type photo-activity across the main basal plane and low or no activity near the perimeter edges. 12 out of 52 (23%) SPI-MoS_2 nanoflakes exhibited similar behavior (Figure S2.4 shows more examples). The inactive perimeter edges were striking in SPI-MoS_2 nanoflakes and were also present in our previous study of $MoSe_2$ nanoflakes. The inactive perimeter edges cannot

be explained by the exfoliation process because the Re-MoS_2 nanoflakes did not show this effect and undergo the same exfoliation procedure. Instead, the inactive edges in SPI-MoS_2 and synthetic $MoSe_2$ are likely due to doping heterogeneity effects discussed below.

On the other hand, 9 out 52 (17 %) SPI-MoS_2 nanoflakes exhibited dominant p-type behavior (Figure 2.b and Figure S2.5). We defined dominant p-type nanoflakes as those flakes with >75% of the nanoflake area producing EQE < -1%. The negative EQE values indicate steady state cathodic photocurrents due to the photoelectrochemical reduction of I_3^- and are represented as blue contrast in IQE maps. Interestingly, the mean cathodic IQE of p-type nanoflakes is nearly as efficient as the mean anodic IQE of n-type nanoflakes (Figure 2.a-iii vs. Figure 2.b-iii). These results show the parent SPI-MoS_2 crystal contains both n- and p-type domains and the individual domains are nearly equally efficient under focused laser illumination (i.e., upon photo-excitation of a single domain).

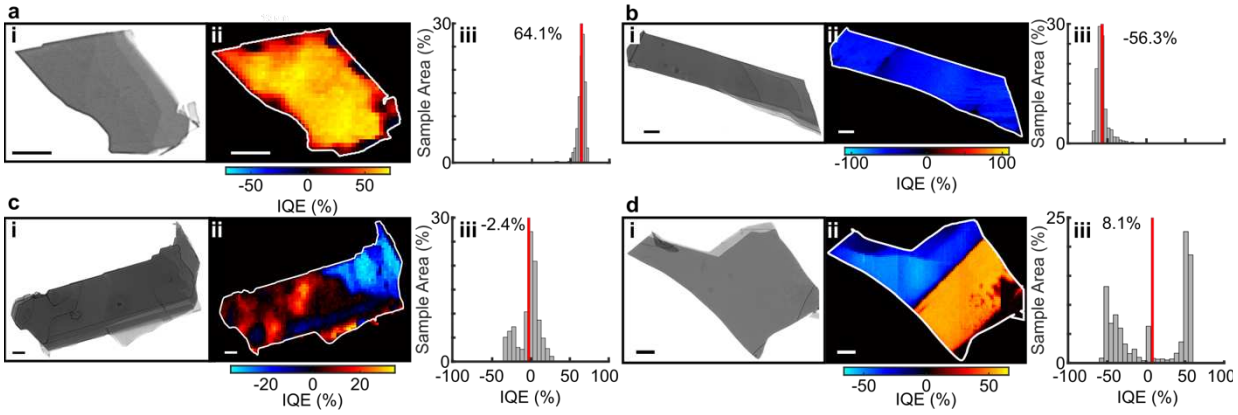

Figure 2.3. Single nanoflake photoelectrochemical measurements of SPI-MoS_2. Representative photocurrent maps of (a) 16 nm-thick n-type nanoflake, (b) 63 nm-thick p-type nanoflake, and (c-d) mixed n-type and p-type within a (c) 63 nm-thick and (d) 70 nm-thick nanoflake. Panels (i-iii) represent bright field transmission images, IQE maps, and IQE distributions, respectively. IQE maps were measured at +0.600 V vs Ag/AgI in aqueous 1 M NaI/1mM I_2 electrolyte using a 860 nm-diameter, 0.50 mW 415 nm laser. All scale bars are 10 mm.

Single nanoflake-level measurements also revealed intra-nanoflake doping heterogeneity in SPI-MoS_2. For 31 out of 52 nanoflakes, n- and p-type domains appeared within a single nanoflake (Figure 2.c,i-iii and more examples in Figure S2.6). In 39% of nanoflakes, we observed large n- and p-type domains separated by sharp boundaries (Figure 2.d,i-iii and more examples in Figure S2.7). The average fractional areas of the n- and p-type domains were 17 ± 27% and 37 ± 41%, respectively. Of all the nanoflakes with intra-nanoflake doping heterogeneity, 71% exhibited a mean anodic current response at fixed +0.6 V (Figure 2.d-ii). The remaining 29% yielded a net cathodic photocurrent response (Figure 2.c-iii). The fact that more nanoflakes exhibit n-type behavior agrees with the net anodic photocurrent magnitude at +0.6 V in ensemble-average photocurrent-voltage curves (Figure 2.c-top). Interestingly, the locations of the n- and p-type domains in Figure 2.c-d did not necessarily correlate with structural features apparent in optical reflection images or transmission images, suggesting that materials chemistry properties influence local doping heterogeneity instead of physical properties such as layer thickness or step edges. Another interesting feature of the mixed behavior nanoflakes is that the average value of the IQE distributions are nearly 0% (Figure 2.c-iii and Figure 2.d-iii). This low average value suggests that, upon illuminating the entire nanoflake, the sum of the photocurrents is nearly zero even though there are highly active n- and p-type domains within the nanoflake.

To further understand how the presence of n- and p-type domains in a single nanoflake contribute to the total nanoflake photocurrent, we measured *i-E* curves at single domains with a focused laser spot. The filled red circles in Figure 2.4a show *i-E* curves from three different n-type domains located on three different SPI-MoS_2 nanoflakes. Each curve displays n-type Schottky diode behavior: the photocurrent increases rapidly with increasingly positive potentials and reaches a potential-independent value within 25 mV of E_{on}. Salvador and Pujadas previously

observed a steep rise in initial photocurrent versus applied potential curves that mimic the lock-in detection conditions employed in this work.[14] The *i-E* curves from SPI-MoS_2 n-type domains varied more than those from Re-MoS_2 (filled blue circles in Figure 2.a). As a result, the distribution of E_{on} values from natural SPI-MoS_2 nanoflakes was significantly larger than synthetic Re-MoS_2 nanoflakes (filled red versus filled blue circles in Figure 2.4b). Chaparro et al. also reported variations in E_{on} and *i-E* curve shapes from different regions of bulk n-WSe_2 and n-$MoSe_2$ crystals.[45] Figure 2.b quantitatively compares E_{on} values from SPI-MoS_2 and Re-MoS_2. The average E_{on} value of Re-MoS_2 was about 100 mV more negative than SPI-MoS_2 (0.223 ± 0.004 V versus 0.316 ± 0.032 V, see diamond symbols in Figure 2.4b). Since E_{on} is equivalent to E_{fb} for ideal semiconductor/electrolyte interfaces (i.e., $E_{on} \approx E_{fb} = E_F - E^{0'}(I^-/I_2)$),[52] the more negative E_{on} value for Re-MoS_2 is likely due to a more negative Fermi level position on the electrochemical scale (E_F) as a result of higher doping density in the synthetic Re-doped crystals.

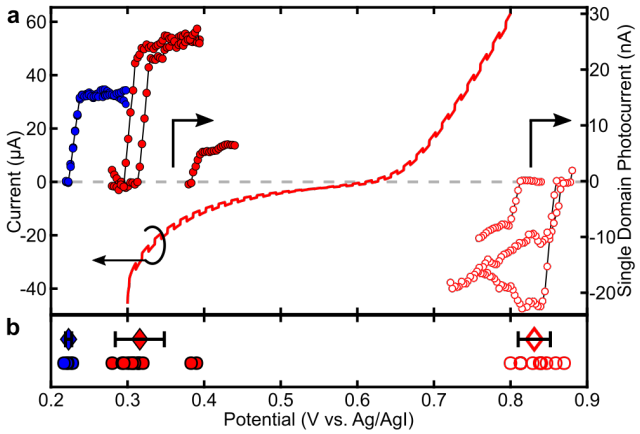

Figure 2.4: Single domain *i-E* curves from Re-MoS_2 and SPI-MoS_2. (a) Ensemble-level chopped light LSV from Figure 2.a (solid line, left axis). Single domain *i-E* curves from 2 Re-MoS_2 nanoflakes (blue filled circles), 3 n-type SPI-MoS_2 domains (red filled circles), and 3 p-type SPI-MoS_2 domains (red open circles). The solid lines show ensemble-level *i-E* curves from Figure 2.a. (b) Distribution of E_{on} values from the individual domain curves in panel a (circles). The diamond markers indicate the average E_{on}. Error bars represent the standard deviation.

The *i-E* curves from p-type domains display p-type Schottky diode behavior: the cathodic current rises sharply at E_{on} and reaches a potential-independent value (open red circles in Figure 2.4a). The *i-E* curves from the natural SPI-MoS_2 varied significantly from domain to domain, yielding a large distribution of E_{on} values (open red circles in Figure 2.4b). The average E_{on} value from the p-type domains was 0.831 ± 0.021 V. Importantly, none of the single domain *i-E* curves from SPI-MoS_2 exhibited a photocurrent switching effect that was apparent in the ensemble-level measurement in Figure 2.c. Therefore, the photocurrent switching effect observed at the ensemble-level in Figure 2.c is likely caused by summing n- and p-type domain currents, which will be discussed below.

2.3.2 Materials characterization.

To understand the origin of doping heterogeneity in SPI-MoS_2, we analyzed the morphology and composition of Re-MoS_2 and SPI-MoS_2 samples using ICP-AES, SEM-EDS, and XPS. Elemental analysis did not show significant composition variations between the samples (Table S2.1). If impurities are responsible for the p-type domains in SPI-MoS_2, then they are likely present in less than ppb concentrations, which is lower than the detection limit of the ICP-AES instrument. The flake morphologies appear qualitatively similar in SEM images (Figure S2.8) and no significant composition differences between the samples were observed in SEM-EDS, in agreement with the ICP-AES elemental analysis results.

XPS analysis revealed major differences between Re-MoS_2 and SPI-MoS_2. Figure 2.a shows XPS spectra of the Mo 3d region measured from three different 800 mm^2 regions of freshly cleaved Re-MoS_2. The peak positions did not depend on sample position and the average binding energy from three locations was 229.0 ± 0.03 eV. On the other hand, the Mo 3d spectra from SPI-MoS_2 crystals vary from location to location (Figure 2.b). Figure 2.c compares the Mo $3d_{5/2}$ peak

binding energy values from different regions of Re-MoS_2 and SPI-MoS_2 (see Figure S2.9 for S peak fitting results). The SPI-MoS_2 Mo $3d_{5/2}$ peak binding energy varies from 230.0 eV to 228.5 eV, whereas the Re-MoS_2 peak binding energy remains constant at 229.0 eV. For the SPI-MoS_2 sample, the peak shifts are accompanied by changes in the S:Mo atomic ratio (indicated by the large red oval in Figure 2.d). Mo $3d_{5/2}$ peak shifts to lower binding energy are correlated with higher S:Mo ratios. McDonnell et. al. reported that this peak shift to lower binding energy can be explained by S-rich, p-type domains.[53] In this scenario, the peak shifts to lower binding energy because the Fermi level moves toward the valence band. The shifts in Mo binding energy are not attributed to a new chemical state as similar shifts in binding energy are observed for S 2p spectra. On the other hand, the Re-MoS_2 data localizes to a constant binding energy and S:Mo ratio (indicated by the small blue oval in Figure 2.d).

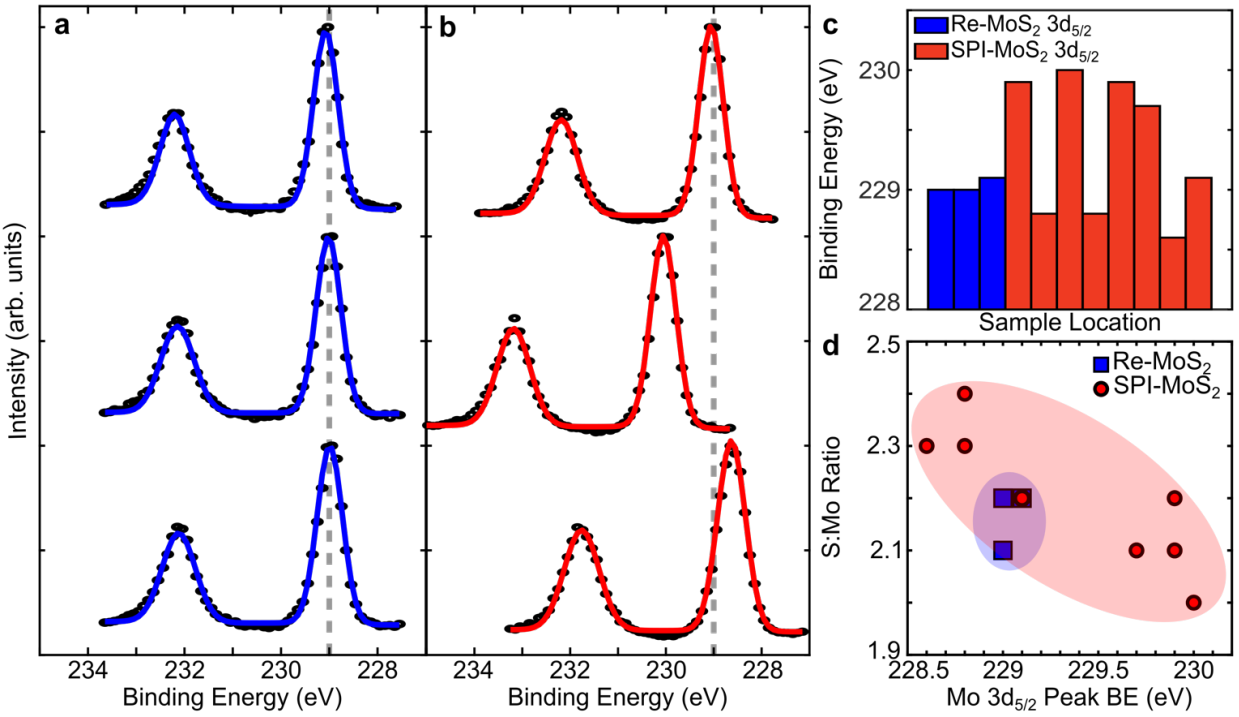

Figure 2.5. XPS analysis of Re-MoS_2 and SPI-MoS_2. (a-b) Spectra of the Mo 3d region from three separate locations on (a) Re-MoS_2 and (b) SPI-MoS_2. Solid blue and red lines represent fits to the data (solid circles). The vertical dashed gray lines represent the average Mo $3d_{5/2}$ peak position from all individual spectra. (c) Mo $3d_{5/2}$ peak positions for different sample locations. (d) S:Mo ratio, as determined from XPS peak fitting, versus the Mo $3d_{5/2}$ peak binding energy. The large

red oval highlights the negative correlation between binding energy and S:Mo ratio for SPI-MoS_2. The small blue oval highlights the nearly constant binding energy and S:Mo ratio for Re-MoS_2.

2.4 Discussion

Here we (1) discuss the likely origin and mechanism of doping heterogeneity in SPI-MoS_2 and (2) describe how the n- and p-type diode response of individual domains contributes to the total current of a single nanoflake.

Nonideal stoichiometry likely causes the doping heterogeneity in SPI-MoS_2. Our XPS data showed a sample location-dependent correlation between the S:Mo ratio and the Mo $3d_{5/2}$ peak binding energy (Figure 2.). In 1968, Upadhyayula et al. linked the presence of excess chalcogen to p-type conductivity in synthetic WSe_2 crystals,[54] suggesting that the S-rich locations of the SPI-MoS_2 crystal studied herein are responsible for p-type photoelectrochemical behavior. Recent scanning tunneling spectroscopy (STS) and XPS measurements of SPI-MoS_2 crystals showed similar trends: S-rich regions of MoS_2 exhibit p-type behavior.[53] In addition, the Mo 3d and S 2p binding energies shifted to lower binding energy in S-rich regions, in agreement with our data in Figure 2.. In 1981, Menezes and Lewerenz first demonstrated how the doping heterogeneity effect influenced photoelectrochemical performance in a I^-/I_3^- electrolyte similar to the one employed in this work.[17] The authors showed n- and p-type domains co-exist in synthetic WSe_2 photoelectrodes grown by chemical vapor transport. The 0.06 mm^2 633 nm laser spot in those experiments was 10^5 times larger than the light spot employed herein, which prevented direct observation and quantification of domain sizes. Regardless, Menezes et al. attributed the doping heterogeneity to variations in Se concentration or segregation of impurities. The doping heterogeneity effect was also reported for other TMD materials and growth methods.[55]

Multiple mechanisms can explain the doping heterogeneity effect in bulk TMDs. Santosh et al. reported the exfoliation process produces S vacancies. The S vacancies produce defect states within the band gap, 0.6 eV below the conduction band minimum (CBM).[56] These defect donor levels can contribute to the n-type character of S-deficient domains.[57] However, other reports have disputed this mechanism.[57–61] Zhang et. al. showed that S vacancies led to the formation of acceptor states just above the valence band maximum (VBM) and an upward shift of the VBM by 0.2 eV toward the Fermi level, consistent with p-type doping.[62] The STS study of the same SPI-MoS_2 crystals employed herein provide strong evidence that S-rich regions exhibit p-type doping behavior, suggesting the former mechanism can explain doping heterogeneity in these naturally occurring crystals. Regardless of the exact mechanism responsible for doping heterogeneity in these natural crystals, our spatially resolved *i-E* measurements revealed the presence of n- and p-type domains within single exfoliated MoS_2 nanoflakes and quantified the distribution of domain sizes.

Finally, we discuss how the photoelectrochemical properties of individual domains contribute to the total current under whole-flake illumination. If we illuminate an entire nanoflake, then the total nanoflake current will be the sum of the individual n- and p-type diode currents. Scheme 2.1 schematically shows how the n- and p-type diode currents (dashed orange and blue lines, respectively) sum to an s-shaped curve (solid black line). This s-shaped curve qualitatively agrees with the ensemble-average photoelectrochemical behavior from Figure 2.c (red line in Scheme 2.1) and explains the apparent photocurrent switching effect in Figure 2.c. E_{switch} occurs about halfway between the E_{on} values of the n- and p-type domains.

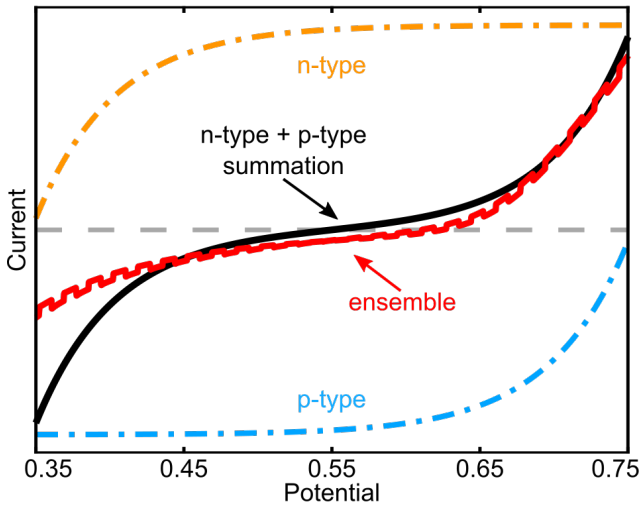

Scheme 2.1: Schematic explanation of how individual n- and p-type domain currents contribute to the ensemble-level photoelectrochemical behavior. The dot-dashed lines represent n- and p-type diode curves from individual domains, under constant illumination. The black line represents the sum of the individual curves. The red line is the ensemble-level experimental data for SPI-MoS_2 under chopped illumination, from Figure 2.1c.

2.5 Conclusion

TMD nanoflake electrodes exhibit lower PEC performance than bulk TMDs. Single nanoflake-level IQE mapping revealed n- and p-type domains within single nanoflakes. Average IQE values from single domains exceeded 60%, indicating that the individual n- and p-type domains were efficient for iodide oxidation and tri-iodide reduction, respectively. Single domain *i-E* curves showed diode-like responses that do not appear in the ensemble-level photoelectrochemical measurement. We propose that the sum of the n- and p-type diode currents cause the low ensemble-average PEC current response. XPS measurements indicate that the origin of the n- and p-type domains is likely non-ideal stoichiometry within the parent crystal. Our findings contribute to the understanding of the origin of the performance gap between bulk and nanoflake TMD photoelectrodes. Furthermore, our work suggests that it may be possible to

synthesize nanoflakes with lateral p-n junctions to enhance charge separation in TMD photocatalysts.

REFERENCES

(1) Yu, X.; Sivula, K. Toward Large-Area Solar Energy Conversion with Semiconducting 2D Transition Metal Dichalcogenides. *ACS Energy Lett*. **2016**, *1* (1), 315–322. https://doi.org/10.1021/acsenergylett.6b00114.

(2) Lu, Q.; Yu, Y.; Ma, Q.; Chen, B.; Zhang, H. 2D Transition-Metal-Dichalcogenide-Nanosheet-Based Composites for Photocatalytic and Electrocatalytic Hydrogen Evolution Reactions. *Advanced Materials* **2016**, *28* (10), 1917–1933. https://doi.org/10/f3kcd5.

(3) Velický, M.; Toth, P. S. From Two-Dimensional Materials to Their Heterostructures: An Electrochemist's Perspective. *Applied Materials Today* **2017**, *8*, 68–103. https://doi.org/10/ggssfs.

(4) Tributsch, H. Solar Energy-Assisted Electrochemical Splitting of Water. Some Energetical, Kinetical and Catalytical Considerations Verified on MoS2 Layer Crystal Surfaces. *Z. Naturforsch. A*. **1977**, *32* (9), 972–985. https://doi.org/10/ggp7h7.

(5) Tributsch, H. Electrochemical Solar Cells Based on Layer-Type Transition Metal Compounds: Performance of Electrode Material. *Sol. Energy Mater*. **1979**, *1* (3), 257–269. https://doi.org/10.1016/0165-1633(79)90044-3.

(6) Bernardi, M.; Palummo, M.; Grossman, J. C. Extraordinary Sunlight Absorption and One Nanometer Thick Photovoltaics Using Two-Dimensional Monolayer Materials. *Nano Lett*. **2013**, *13* (8), 3664–3670. https://doi.org/10.1021/nl401544y.

(7) Gobrecht, J.; Tributsch, H.; Gerischer, H. Performance of Synthetical N-MoSe2 in Electrochemical Solar Cells. *J. Electrochem. Soc*. **1978**, *125* (12), 2085. https://doi.org/10/ddtbz9.

(8) Gobrecht, J.; Gerischer, H.; Tributsch, H. Electrochemical Solar Cell Based on the D-Band Semiconductor Tungsten-Diselenide. *Ber. Bunsen. Phys. Chem*. **1978**, *82* (12), 1331–1335. https://doi.org/10.1002/bbpc.19780821212.

(9) Schneemeyer, L.; Wrighton, M. Flat-Band Potential of n-Type Semiconducting Molybdenum Disulfide by Cyclic Voltammetry of Two-Electron Reductants: Interface Energetics and the Sustained Photooxidation of Chloride. *J. Am. Chem. Soc*. **1979**, *101* (22), 6496–6500. https://doi.org/10/fxfkkq.

(10) Lewerenz, H. J.; Heller, A.; DiSalvo, F. J. Relationship between Surface Morphology and Solar Conversion Efficiency of Tungsten Diselenide Photoanodes. *J. Am. Chem. Soc*. **1980**, *102* (6), 1877–1880. https://doi.org/10/b52hqq.

(11) Kline, G.; Kam, K.; Canfield, D.; Parkinson, B. A. Efficient and Stable Photoelectrochemical Cells Constructed with WSe2 and MoSe2 Photoanodes. *Sol. Energy Mater*. **1981**, *4* (3), 301–308. https://doi.org/10/d87x7q.

(12) Kautek, W.; Gerischer, H. Anisotropic Photocorrosion of N-Type MoS2 MoSe2, and WSe2 Single Crystal Surfaces: The Role 0f Cleavage Steps, Line and Screw Dislocations. *Surface Science* **1982**, *119* (1), 46–60. https://doi.org/10/fcmw2m.

(13) Tenne, R.; Wold, A. Passivation of Recombination Centers in N-WSe2 Yields High Efficiency (>14%) Photoelectrochemical Cell. *Appl. Phys. Lett*. **1985**, *47* (7), 707–709. https://doi.org/10/fcxrk9.

(14) Salvador, P.; Pujadas, M.; Campet, G. Photoreactions at the N-Type-WSe2--Electrolyte Interface: Study by Electrolyte Electroreflectance and Photocurrent Transient Measurements. *Phys. Rev. B* **1988**, *38* (14), 9881–9888. https://doi.org/10/d7qzqm.
(15) Kautek, W.; Gerischer, H. The Photoelectrochemistry of the Aqueous Iodide/Iodine Redox System at n-Type MoSe2-Electrodes. *Electrochimica Acta* **1981**, *26* (12), 1771–1778. https://doi.org/10.1016/0013-4686(81)85162-6.
(16) Furtak, T. E.; Canfield, D. C.; Parkinson, B. A. Scanning Light-spot Analysis of the Carrier Collection in Liquid-junction Solar Energy Converters. *J. Appl. Phys.* **1980**, *51* (11), 6018–6021. https://doi.org/10/fvdfk5.
(17) Menezes, S.; Schneemeyer, L. F.; Lewerenz, H. J. Efficiency Losses from Carrier-type Inhomogeneity in Tungsten Diselenide Photoelectrodes. *Appl. Phys. Lett.* **1981**, *38* (11), 949–951. https://doi.org/10/bpmvbx.
(18) Li, C.; Cao, Q.; Wang, F.; Xiao, Y.; Li, Y.; Delaunay, J.-J.; Zhu, H. Engineering Graphene and TMDs Based van Der Waals Heterostructures for Photovoltaic and Photoelectrochemical Solar Energy Conversion. *Chem. Soc. Rev.* **2018**, *47* (13), 4981–5037. https://doi.org/10.1039/C8CS00067K.
(19) Ganguly, P.; Harb, M.; Cao, Z.; Cavallo, L.; Breen, A.; Dervin, S.; Dionysiou, D. D.; Pillai, S. C. 2D Nanomaterials for Photocatalytic Hydrogen Production. *ACS Energy Lett.* **2019**, *4* (7), 1687–1709. https://doi.org/10.1021/acsenergylett.9b00940.
(20) Wells, R. A.; Johnson, H.; Lhermitte, C. R.; Kinge, S.; Sivula, K. Roll-to-Roll Deposition of Semiconducting 2D Nanoflake Films of Transition Metal Dichalcogenides for Optoelectronic Applications. *ACS Appl. Nano Mater.* **2019**, *2* (12), 7705–7712. https://doi.org/10.1021/acsanm.9b01774.
(21) Magda, G. Z.; Pető, J.; Dobrik, G.; Hwang, C.; Biró, L. P.; Tapasztó, L. Exfoliation of Large-Area Transition Metal Chalcogenide Single Layers. *Sci Rep* **2015**, *5* (1), 14714. https://doi.org/10.1038/srep14714.
(22) Liu, F.; Wu, W.; Bai, Y.; Chae, S. H.; Li, Q.; Wang, J.; Hone, J.; Zhu, X.-Y. Disassembling 2D van Der Waals Crystals into Macroscopic Monolayers and Reassembling into Artificial Lattices. *Science* **2020**, *367* (6480), 903–906. https://doi.org/10.1126/science.aba1416.
(23) Fan, F.-R. F.; White, H. S.; Wheeler, B.; Bard, A. J. Semiconductor Electrodes: XXIX . High Efficiency Photoelectrochemical Solar Cells with Electrodes in an Aqueous Iodide Medium. *J. Electrochem. Soc.* **1980**, *127* (2), 518. https://doi.org/10.1149/1.2129700.
(24) Kline, G.; Kam, K. K.; Ziegler, R.; Parkinson, B. A. Further Studies of the Photoelectrochemical Properties of the Group VI Transition Metal Dichalcogenides. *Solar Energy Materials* **1982**, *6* (3), 337–350. https://doi.org/10.1016/0165-1633(82)90039-9.
(25) McKone, J. R.; Pieterick, A. P.; Gray, H. B.; Lewis, N. S. Hydrogen Evolution from Pt/Ru-Coated p-Type WSe2 Photocathodes. *J. Am. Chem. Soc.* **2013**, *135* (1), 223–231. https://doi.org/10.1021/ja308581g.
(26) Yu, X.; Prévot, M. S.; Guijarro, N.; Sivula, K. Self-Assembled 2D WSe 2 Thin Films for Photoelectrochemical Hydrogen Production. *Nat Commun* **2015**, *6* (1), 7596. https://doi.org/10.1038/ncomms8596.
(27) Yu, X.; Guijarro, N.; Johnson, M.; Sivula, K. Defect Mitigation of Solution-Processed 2D WSe2 Nanoflakes for Solar-to-Hydrogen Conversion. *Nano Lett.* **2017**, *18* (1), 215–222. https://doi.org/10/gcpk8j.

(28) Todt, M. A.; Isenberg, A. E.; Nanayakkara, S. U.; Miller, E. M.; Sambur, J. B. Single-Nanoflake Photo-Electrochemistry Reveals Champion and Spectator Flakes in Exfoliated MoSe2 Films. *J. Phys. Chem. C* **2018**, *122* (12), 6539–6545. https://doi.org/10/gdc6df.
(29) Parkinson, B. A.; Furtak, T. E.; Canfield, D.; Kam, K.-K.; Kline, G. Evaluation and Reduction of Efficiency Losses at Tungsten Diselenide Photoanodes. *Faraday Discuss. Chem. Soc.* **1980**, *70* (0), 233–245. https://doi.org/10/cg82t4.
(30) Fan, F.-R. F.; Bard, A. J. Semiconductor Electrodes: XXXVI . Characteristics of , Electrodes in Aqueous Solution. *J. Electrochem. Soc.* **1981**, *128* (5), 945. https://doi.org/10.1149/1.2127580.
(31) Lewerenz, H. J.; Gerischer, H.; Lübke, M. Photoelectrochemistry of WSe2 Electrodes: Comparison of Stepped and Smooth Surfaces. *J. Electrochem. Soc.* **1984**, *131* (1), 100. https://doi.org/10/cgqfcc.
(32) Kautek, W.; Gerischer, H.; Tributsch, H. The Role of Surface Orientation in the Photoelectrochemical Behavior of Layer Type D-Band Semiconductors. *Ber. Bunsen. Phys. Chem.* **1979**, *83* (10), 1000–1008. https://doi.org/10.1002/bbpc.19790831010.
(33) Salvador, P.; Chaparro, A. M.; Mir, A. Digital Imaging of the Effect of Photoetching on the Photoresponse of N-Type Tungsten Diselenide and Molybdenum Diselenide Single Crystal Electrodes. *J. Phys. Chem.* **1996**, *100* (2), 760–768. https://doi.org/10/fhvs5p.
(34) M. Velazquez, J.; John, J.; V. Esposito, D.; Pieterick, A.; Pala, R.; Sun, G.; Zhou, X.; Huang, Z.; Ardo, S.; P. Soriaga, M.; S. Brunschwig, B.; S. Lewis, N. A Scanning Probe Investigation of the Role of Surface Motifs in the Behavior of P-WSe 2 Photocathodes. *Energy Environ. Sci.* **2015**, *9* (1), 164–175. https://doi.org/10/ggpvh4.
(35) Eisenberg, D. Imaging the Anisotropic Reactivity of a Tungsten Diselenide Photocathode. *ChemElectroChem* **2015**, *2* (9), 1259–1263. https://doi.org/10/f277m3.
(36) Canfield, D.; Parkinson, B. A. Improvement of Energy Conversion Efficiency by Specific Chemical Treatments of Molybdenum Selenide (n-MoSe2) and Tungsten Selenide (n-WSe2) Photoanodes. *J. Am. Chem. Soc.* **1981**, *103* (5), 1279–1281. https://doi.org/10/fnk2st.
(37) White, H. S.; Abruna, H. D.; Bard, A. J. Semiconductor Electrodes: XLI . Improvement of Performance of Electrodes by Electrochemical Polymerization of O-Phenylenediamine at Surface Imperfections. *J. Electrochem. Soc.* **1982**, *129* (2), 265. https://doi.org/10.1149/1.2123810.
(38) Shearer, M. J.; Li, W.; Foster, J. G.; Stolt, M. J.; Hamers, R. J.; Jin, S. Removing Defects in WSe2 via Surface Oxidation and Etching to Improve Solar Conversion Performance. *ACS Energy Lett.* **2019**, *4* (1), 102–109. https://doi.org/10.1021/acsenergylett.8b01922.
(39) Velický, M.; Bissett, M. A.; Woods, C. R.; Toth, P. S.; Georgiou, T.; Kinloch, I. A.; Novoselov, K. S.; Dryfe, R. A. W. Photoelectrochemistry of Pristine Mono- and Few-Layer MoS2. *Nano Lett.* **2016**, *16* (3), 2023–2032. https://doi.org/10.1021/acs.nanolett.5b05317.
(40) Hill, J. W.; Hill, C. M. Directly Mapping Photoelectrochemical Behavior within Individual Transition Metal Dichalcogenide Nanosheets. *Nano Lett.* **2019**, *19* (8), 5710–5716. https://doi.org/10.1021/acs.nanolett.9b02336.
(41) Takahashi, Y.; Kobayashi, Y.; Wang, Z.; Ito, Y.; Ota, M.; Ida, H.; Kumatani, A.; Miyazawa, K.; Fujita, T.; Shiku, H.; Korchev, Y. E.; Miyata, Y.; Fukuma, T.; Chen, M.; Matsue, T. High-Resolution Electrochemical Mapping of the Hydrogen Evolution Reaction on Transition-Metal Dichalcogenide Nanosheets. *Angew. Chem.* **2020**, *59* (9), 3601–3608. https://doi.org/10.1002/anie.201912863.

(42) Hill, J. W.; Fu, Z.; Tian, J.; Hill, C. M. Locally Engineering and Interrogating the Photoelectrochemical Behavior of Defects in Transition Metal Dichalcogenides. *J. Phys. Chem. C* **2020**, *124* (31), 17141–17149. https://doi.org/10.1021/acs.jpcc.0c05235.
(43) Tóth, P. S.; Szabó, G.; Janáky, C. Structural Features Dictate the Photoelectrochemical Activities of Two-Dimensional MoSe2 and WSe2 Nanostructures. *J. Phys. Chem. C* **2021**, *125* (14), 7701–7710. https://doi.org/10.1021/acs.jpcc.1c01265.
(44) Bicelli, L. P.; Razzini, G. Surface Defects on N-MoSe2 Electrodes Used in Photoelectrochemical Solar Cells. *Surface Technology* **1983**, *20* (4), 383–392. https://doi.org/10.1016/0376-4583(83)90116-4.
(45) Chaparro, A. M.; Salvador, P.; Mir, A. The Scanning Microscope for Semiconductor Characterization: Photocurrent, Photovoltage and Electrolyte Electroreflectance Imaging at the n-MoSe2/I– Interface. *J. Electroanal. Chem.* **1997**, *424* (1), 153–157. https://doi.org/10/cbf5rw.
(46) Castellanos-Gomez, A.; Buscema, M.; Molenaar, R.; Singh, V.; Janssen, L.; Zant, H. S. J. van der; Steele, G. A. Deterministic Transfer of Two-Dimensional Materials by All-Dry Viscoelastic Stamping. *2D Mater.* **2014**, *1* (1), 011002. https://doi.org/10.1088/2053-1583/1/1/011002.
(47) Isenberg, A. E.; Todt, M. A.; Wang, L.; Sambur, J. B. Role of Photogenerated Iodine on the Energy-Conversion Properties of MoSe2 Nanoflake Liquid Junction Photovoltaics. *ACS Appl. Mater. Interfaces* **2018**, *10* (33), 27780–27786. https://doi.org/10.1021/acsami.8b07617.
(48) Wang, L.; Sambur, J. B. Efficient Ultrathin Liquid Junction Photovoltaics Based on Transition Metal Dichalcogenides. *Nano Lett.* **2019**, *19* (5), 2960–2967. https://doi.org/10/gf2wsk.
(49) Chen, Z.; Forman, A. J.; Jaramillo, T. F. Bridging the Gap Between Bulk and Nanostructured Photoelectrodes: The Impact of Surface States on the Electrocatalytic and Photoelectrochemical Properties of MoS2. *J. Phys. Chem. C* **2013**, *117* (19), 9713–9722. https://doi.org/10.1021/jp311375k.
(50) Frindt, R. F.; Yoffe, A. D.; Bowden, F. P. Physical Properties of Layer Structures : Optical Properties and Photoconductivity of Thin Crystals of Molybdenum Disulphide. *Proc. R. Soc. A.* **1963**, *273* (1352), 69–83. https://doi.org/10.1098/rspa.1963.0075.
(51) Hill, J. W.; Hill, C. M. Directly Visualizing Carrier Transport and Recombination at Individual Defects within 2D Semiconductors. *Chem. Sci.* **2021**, *12* (14), 5102–5112. https://doi.org/10.1039/D0SC07033E.
(52) Cooper, G.; Turner, J. A.; Nozik, A. J. Mott-Schottky Plots and Flatband Potentials for Single Crystal Rutile Electrodes. *J. Electrochem. Soc.* **1982**, *129* (9), 1973. https://doi.org/10.1149/1.2124334.
(53) McDonnell, S.; Addou, R.; Buie, C.; Wallace, R. M.; Hinkle, C. L. Defect-Dominated Doping and Contact Resistance in MoS2. *ACS Nano* **2014**, *8* (3), 2880–2888. https://doi.org/10/f5whbz.
(54) Upadhyayula, L. C.; Loferski, J. J.; Wold, A.; Giriat, W.; Kershaw, R. Semiconducting Properties of Single Crystals of N- and P-Type Tungsten Diselenide (WSe2). *J. Appl. Phys.* **1968**, *39* (10), 4736–4740. https://doi.org/10.1063/1.1655829.
(55) Hofmann, W. K.; Lewerenz, H. J. Improved Photoactivity of Melt-Grown Group VI Transition Metal Dichalcogenides: Preparation from Se and Se-Te Melts. *Sol. Energy Mater.* **1988**, *17* (5), 369–374. https://doi.org/10.1016/0165-1633(88)90018-4.

(56) KC, S.; Longo, R. C.; Addou, R.; Wallace, R. M.; Cho, K. Impact of Intrinsic Atomic Defects on the Electronic Structure of MoS2monolayers. *Nanotechnology* **2014**, *25* (37), 375703. https://doi.org/10.1088/0957-4484/25/37/375703.
(57) Brandão, F. D.; Ribeiro, G. M.; Vaz, P. H.; González, J. C.; Krambrock, K. Identification of Rhenium Donors and Sulfur Vacancy Acceptors in Layered MoS2 Bulk Samples. *J. Appl. Phys.* **2016**, *119* (23), 235701. https://doi.org/10.1063/1.4954017.
(58) Komsa, H.-P.; Krasheninnikov, A. V. Native Defects in Bulk and Monolayer MoS2 from First Principles. *Phys. Rev. B* **2015**, *91* (12), 125304. https://doi.org/10.1103/PhysRevB.91.125304.
(59) Noh, J.-Y.; Kim, H.; Kim, Y.-S. Stability and Electronic Structures of Native Defects in Single-Layer MoS2. *Phys. Rev. B* **2014**, *89* (20), 205417. https://doi.org/10.1103/PhysRevB.89.205417.
(60) Singh, A.; Singh, A. K. Origin of N-Type Conductivity of Monolayer MoS2. *Phys. Rev. B* **2019**, *99* (12), 121201. https://doi.org/10.1103/PhysRevB.99.121201.
(61) Rao, R.; Carozo, V.; Wang, Y.; Islam, A. E.; Perea-Lopez, N.; Fujisawa, K.; Crespi, V. H.; Terrones, M.; Maruyama, B. Dynamics of Cleaning, Passivating and Doping Monolayer MoS 2 by Controlled Laser Irradiation. *2D Mater.* **2019**, *6* (4), 045031. https://doi.org/10.1088/2053-1583/ab33ab.
(62) Zhang, X.; Wang, S.; Lee, C.-K.; Cheng, C.-M.; Lan, J.-C.; Li, X.; Qiao, J.; Tao, X. Unravelling the Effect of Sulfur Vacancies on the Electronic Structure of the MoS2 Crystal. *Phys. Chem. Chem. Phys.* **2020**, *22* (38), 21776–21783. https://doi.org/10.1039/C9CP07004D.
(63) Menezes, S.; Schneemeyer, L. F.; Lewerenz, H. J. Efficiency Losses from Carrier-type Inhomogeneity in Tungsten Diselenide Photoelectrodes. *Appl. Phys. Lett.* **1981**, *38* (11), 949–951. https://doi.org/10/bpmvbx.
(64) Chaparro, A. M.; Salvador, P.; Peter, L. M. The Role of Surface Defects in the Photooxidation of Iodide at N-MoSe2: Evidence for a Local "Autocatalytic" Effect. *J. Phys. Chem.* **1995**, *99* (17), 6677–6683. https://doi.org/10.1021/j100017a059.
(65) Addou, R.; Colombo, L.; Wallace, R. M. Surface Defects on Natural MoS2. *ACS Appl. Mater. Interfaces* **2015**, *7* (22), 11921–11929. https://doi.org/10.1021/acsami.5b01778.
(66) Addou, R.; McDonnell, S.; Barrera, D.; Guo, Z.; Azcatl, A.; Wang, J.; Zhu, H.; Hinkle, C. L.; Quevedo-Lopez, M.; Alshareef, H. N.; Colombo, L.; Hsu, J. W. P.; Wallace, R. M. Impurities and Electronic Property Variations of Natural MoS2 Crystal Surfaces. *ACS Nano* **2015**, *9* (9), 9124–9133. https://doi.org/10.1021/acsnano.5b03309.

CHAPTER 3: MOLECULAR REACTION IMAGING OF A SURFACE RECOMBINATION PROCESS EXPLAINS PERFORMANCE VARIATION AMONG SMOOTH MOS_2 PHOTOELECTRODES[iii]

3.1 Introduction

TMD|I^-,I_3^-|Pt cells are among the most efficient and stable photoelectrochemical (PEC) solar cells known.[1-5] Tenne and Wold reported a WSe_2 cell with 14.1% efficiency and Parkinson and co-authors reported fill factors as high as 0.78.[1,4] These high-performing cells were made using apparently smooth bulk crystals, meaning their surface morphology was qualitatively characterized either by eye or a low resolution optical microscope. Crystals with a high density of exposed step edges typically exhibit higher dark currents, lower photovoltages, and lower fill factors.[6-8] For example, Furtak and Parkinson spatially resolved the carrier collection efficiency using scanning light spot photoelectrochemical measurements of bulk TMD crystals.[9,10] The authors observed the highest efficiencies on smooth basal planes and lowest efficiencies on stepped regions. The performance loss of highly stepped n-type crystals had been attributed to electron exchange via Mo *d*-orbitals extending into the electrolyte at exposed step-edges.[11,1,3,9,10,12,7,13] Kam et. al. used photocurrent spectroscopy of edge and basal plane mounted crystals to show that crystal edges introduce surface states into the band-gap of the material.[13] These surface states can participate in the dark reduction of I_3^-, which reduces the solar cell performance characteristics. In summary, TMD liquid junction solar cell research largely conducted in the 1980s concluded that smooth crystals were necessary for achieving high efficiency solar cells.

[iii] This chapter is part of a manuscript that has been accepted for publication to the Journal of the Electrochemical Society. Michael Van Erdewyk performed the experiments and analyzed data. Michael Van Erdewyk and Justin B. Sambur designed experiments and wrote the manuscript.

However, Parkinson et. al. also reported poor PCE in several "apparently defect-free" TMD crystals. These results were attributed to impurities within the crystal that could affect the depth of the space-charge region. At the same time, Menezes and Lewerenz reported that doping heterogeneity limits PEC efficiency in WSe_2 crystals with smooth basal planes.[14] However, the size and role of mixed n- and p-type domains on photoelectrochemical performance had not been elucidated.

We recently revisited the question of doping heterogeneity in MoS_2 nanoflake samples exfoliated from both synthetic and naturally occurring crystals and discovered that highly efficient n- and p-type domains can be present within an individual nanoflake.[15] In those experiments, a 1 μm-diameter light spot excites a single domain. We hypothesized that simultaneously illuminating all n-type and p-type domains within a single nanoflake causes individual n-type and p-type photodiode behaviors to sum and oppose each other, yielding an overall low efficiency nanoflake. In this work, we test that hypothesis using a combination of scanning photocurrent microscopy and whole nanoflake-level photoelectrochemical microscopy experiments. Furthermore, we use a novel molecular reaction imaging technique to uncover a hidden surface recombination process within the p-type domains. Our results provide a unifying view of efficiency variability among smooth TMD|I^-,I_3^-|Pt solar cells.

3.2 Experimental Methods

3.2.1 Electrode preparation:

MoS_2 nanoflake-coated tin-doped indium oxide (ITO) electrodes were prepared by mechanical exfoliation of commercially available bulk MoS_2 crystals: Re-doped n-type MoS_2 (2D semiconductors, BLK-MoS_2-N, doping density 10^{17}-10^{18} cm^{-3}) and naturally occurring bulk MoS_2 (SPI, 470MOS2L-AB). The detailed two-step exfoliation procedure[16] using low residue Nitto tape

(BT–150E–CM, Nitto) and gel–film (Gelfilm from Gelpak) can be found in the Supplemental Information of our previous study.[15] The nanoflake–coated ITO electrodes were assembled into a 3–electrode electrochemical flow cell as described previously.[17] A Pt wire and Ag/AgI wire served as the counter and reference electrodes, respectively.

3.2.2 Scanning photoelectrochemical microscopy:

The electrochemical flow cells were mounted on an Olympus IX73 inverted microscope equipped with confocal Raman and photoelectrochemical mapping capabilities. Scanning photoelectrochemical microscopy experiments were carried out at a fixed applied potential of 0.600 V vs. Ag/AgI in 1 M NaI/1 mM I_2 electrolyte at a constant flow rate of 25 μL/min. A fixed, low laser power excited the sample (typically 0.30 – 0.50 μW focused into a 0.86 μm–diameter spot size). The incident laser power was less than the critical power necessary to observe iodine deposition.[18] The laser power for each nanoflake is chosen to result in approximately 20 – 40 nA of photocurrent at the most efficient region of the nanoflake. A detailed description of the photoelectrochemical microscopy data acquisition and processing algorithms are provided in the Supporting Information of our previous study.[15]

3.2.3 Molecular reaction imaging experiments:

In a typical molecular reaction imaging experiment, the same focused 415 nm laser used for scanning photocurrent microscopy was rastered across a single nanoflake in 1 μm steps. The location of the line scan was chosen by qualitatively comparing the EQE map with the physical appearance of the nanoflake, as observed in bright field transmission and reflection images (see main text for discussion). At each step or pixel in the line scan, a potentiostat measures the electrochemical current with 40 ms time resolution while a cMOS camera (Prime 95B) acquires bright field transmission images at a 5 per second frame rate. Initially, these data are acquired

under dark conditions for 1 s. Then, an electronic laser shutter opens and the current and bright field images are acquired under illumination conditions for 5 seconds. A second dark period of 2 s follows before the stage is moved to the next position. Hence, each pixel in the line scan requires 8 seconds. This process repeats for each step in the line scan. Following the experiment, the image data was processed using a homewritten MATLAB code detailed in Supplementary Note 2. Briefly, we developed a thresholding algorithm that identifies low contrast pixels in the transmission images that can be assigned to iodine formation during the 5 second period at which the laser is illuminating the flake.[18] The identified iodine deposition spots are collated for each pixel in the line scan and overlaid on a single reference image of the nanoflake as shown in Figure 3.1 of main text.

3.2.4 Single flake photocurrent–potential measurements:

A linear sweep waveform (0.30 V to 0.70 V at a scan rate of 5 mV/s) was applied to the entire nanoflake-coated ITO electrode while a 50,000-100,000 μm^2 light spot illuminated an entire nanoflake. To illuminate an entire nanoflake, a 530 nm light emitting diode (LED, THORLabs M530L3) was mounted in the transmitted light illumination column of the inverted microscope, above the electrochemical cell. The field iris diaphragm was used to control the illumination spot size at the sample (Figure S3.1) shows a representative image of the illumination spot size). The LED illumination was chopped at a frequency of 0.3 Hz to distinguish the single nanoflake photocurrent from the ensemble-level dark current.

3.3 Results and Discussion

3.3.1 Doping heterogeneity profiles of single nanoflakes:

We designed a multi-step experimental workflow to test the central hypothesis that simultaneously illuminating all n-type and p-type domains within a single nanoflake causes

individual n-type and p-type photodiode behaviors to sum and oppose each other, yielding an overall low efficiency nanoflake. First, we performed scanning photocurrent microscopy experiments to characterize the doping heterogeneity "profile" of a single TMD nanoflake. Second, we performed molecular reaction imaging experiments that detect reactivity "hot spots" for the iodide oxidation reaction. Importantly, comparing the photocurrent maps with the locations of reactivity hot spots allowed us to reveal the recombination mechanism upon illuminating apparently smooth TMD nanoflakes. Next, we linked those imaging results with the ensemble-level photoelectrochemical behavior of a single nanoflake by measuring current-potential curves under whole-flake illumination conditions. Finally, we aggregated data from 69 nanoflakes and discovered a hidden correlation between the doping heterogeneity profile of a single nanoflake and its global photoelectrochemical behavior.

We studied exfoliated MoS_2 nanoflakes from naturally occurring and synthetic bulk crystals because the quantum yield for iodide oxidation equals the values reported from high efficiency cells in the 1980s and the large number of exfoliated entities allows us to better understand the correlation between basal and edge site surface morphologies on photoelectrochemical performance.[19,17,20,21] The commercial crystal samples used herein are widely studied in the 2D materials community and may provide insight for interpreting current-voltage measurements in optoelectronic devices.[22-28] We choose to present photocurrent maps and molecular reaction imaging results from the naturally occurring crystal because the doping heterogeneity effect is enhanced in that sample.

To measure the doping heterogeneity profile of a single nanoflake, we scan a 415 nm laser across a single nanoflake in 1 μm increments and measure the current from the entire electrode at a fixed applied potential of 0.6 V vs. Ag/AgI (see Figure 3.1a). Figure 3.1d shows a representative

photocurrent map from a single exfoliated nanoflake from a naturally occurring crystal (see additional examples from naturally occurring and synthetic crystals in Figure S3.2 and Figure S3.1). Illuminating n-type MoS_2 domains at 0.600 V vs. Ag/AgI induces an anodic photocurrent due to iodide oxidation (red contrast pixels in Figure 3.1d).[15] Conversely, illuminating p-type MoS_2 domains at the same applied potential induces a cathodic photocurrent due to tri-iodide reduction (blue contrast pixels in Figure 3.1d). The photocurrent maps show n- and p-type domains exist within a single nanoflake. In these experiments, the laser power induces a 20-40 nA photocurrent signal at each illumination condition, which is below the critical current (i.e., reaction rate) to induce iodine deposition on the nanoflake surface (see Supplementary Note 3).[18,29]

3.3.2 Molecular reaction imaging of iodide oxidation hot spots:

Having determined the doping heterogeneity profile of a single nanoflake, we used a molecular reaction imaging approach to (1) characterize where the hole-induced iodide oxidation reaction occurs on the nanoflake surface and (2) further understand how n- and p-type domains influence charge transport to active sites. In a typical molecular reaction imaging experiment, the 415 nm laser moves across the nanoflake in 1 μm increments or steps in a one-dimensional line scan (Figure 3.1a). At each step, a potentiostat measures the electrochemical current from the entire cell while a cMOS camera captures brightfield transmission images of the sample (Figure 3.1b). We adjust the laser power such that the hole-induced iodide oxidation rate exceeds the critical reaction rate (i.e., current) for iodine deposition on the MoS_2 surface (discussed in detail in Supplementary Note 3). Line scan locations were chosen by qualitatively comparing the doping heterogeneity "profile" (i.e., EQE map in Figure 3.1d) with the physical appearance of the nanoflake, as observed in bright field transmission images (Figure 3.1c). For example, we chose the line scan location in Figure 3.1c because this scan direction traverses an n-type/p-type domain boundary and step edges.

In general, we preferred to study n- and p-type domain boundaries and then step-edges (see Supplementary Note 1 for examples).

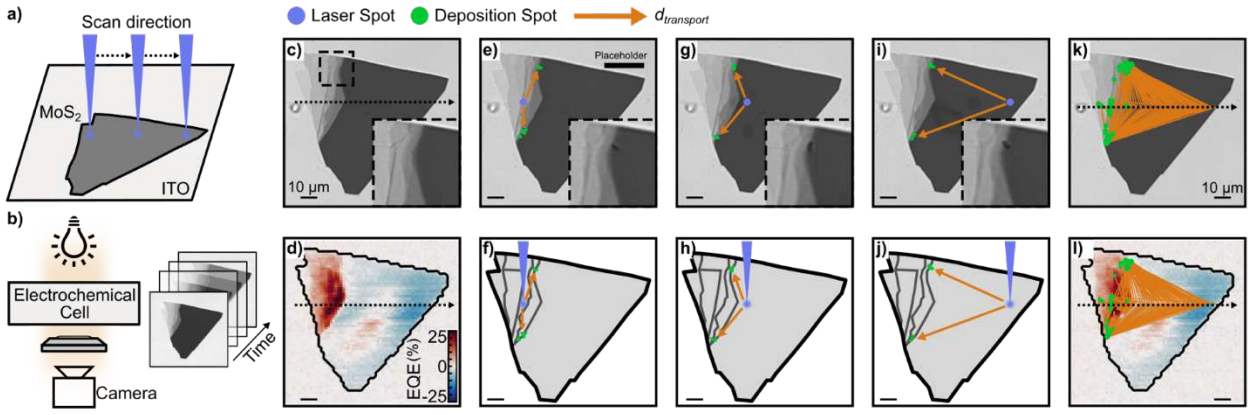

Figure 3.1: Photocurrent mapping and molecular reaction imaging of a single MoS_2 nanoflake. (a) Cartoon illustration of the 425 nm excitation laser scanning across a nanoflake in a point-by-point fashion for 2D photocurrent mapping and 1D molecular reaction imaging line scan experiments. (b) Cartoon illustration of the bright field transmission imaging sequence during molecular reaction imaging. (c) Transmission image and (d) external quantum efficiency (EQE) map of a single MoS_2 nanoflake before a molecular reaction imaging experiment. The black dashed arrow in (c-d) indicates the laser line scan direction. The inset in (c) shows a magnified view of the nanoflake region indicated by the black dashed box. (e, g, i) Transmission images of the same MoS_2 nanoflake at different excitation locations during a molecular reaction imaging experiment. The purple circle, green shaded pixel regions, and the orange arrows represent the laser position, iodine deposition spots, and hole transport distance from the laser centroid to the deposition spot ($d_{transport}$), respectively. The dark contrast pixels in the inset images show the iodine deposition spots. (f, h, j) Cartoon illustrations depicting the carrier generation, hole transport, and hole-induced iodine formation process. (k-i) Cumulative results of a molecular reaction imaging experiment, where all iodine deposition spots and $d_{transport}$ vectors are overlayed on the (k) transmission image and (l) EQE map.

Figure 3.1c-l shows representative molecular reaction imaging results of a single nanoflake with neighboring n- and p-type domains. Initially, we position the excitation laser off the nanoflake on the ITO substrate, which produces no photocurrent (Figure 3.1d) and no pixel contrast changes in bright field transmission images (Figure 3.1c-inset). As the line scan experiment progresses from left to right, the laser moves from the ITO substrate to the MoS_2 nanoflake, inducing an anodic photocurrent in the n-type domain. At the same time, dark contrast pixels appear at step

edges that can be attributed to iodine deposition (Figure 3.1e-inset).[18,29] Supplementary Note 2 describes the detailed image analysis algorithm to detect and analyze the iodine deposition locations. The distance between the focused laser spot centroid and the iodine deposition spots represents the charge transport distance ($d_{transport}$, indicated by orange arrows in Figure 3.1). For the iodine deposition reaction, the charge carrier is a photogenerated hole. Interestingly, for the nanoflake in Figure 3.1, iodine deposition spots repeatedly appear at step edges even as the laser spot moves tens of microns away from the highly reactive step edge. We observed no iodine deposition on the apparently smooth basal plane. The cumulative results in Figure 3.1k show photogenerated holes can travel parallel to the layers as far as 45 μm from the carrier generation location to the reactivity hot spot, in agreement with recent photocurrent mapping results from Hill and co-workers[30] and ensemble-level observations that step edges are highly active for iodide oxidation.[31-34]

One explanation for our observation of micron-scale travel of photogenerated holes is that the negative surface charge drives photogenerated hole transport to the step edges via a drift mechanism. Recently, Hill and co-workers showed that TMD step edges possess significant negative surface charge.[35] The magnitude of the surface charge is apparently sufficiently large enough to generate a lateral electric field emanating from the step edge that overcomes other possible perpendicular electric fields present at the basal planes of the n– and p–type domains.[12,36] Another possibility is that long-range hole transport is driven by carrier diffusion along a concentration gradient from the point of generation (focused laser spot) to the highly active edge site. The micron-scale diffusion length is likely due to the relatively long carrier lifetime of TMD nanoflakes versus single layers.[37] If the highly active edge sites consume holes at a very high rate,

then photogenerated holes in the region of the laser excitation spot may be driven along a concentration gradient to the low hole concentration region at the edge sites.

Statistical analyses of 48 nanoflakes confirmed iodine deposition repeatedly occurs at step edges. To investigate and quantify the relationship between iodine deposition locations and nanoflake surface morphology, we measured the distance from each deposition event to the nearest physical boundary (denoted as $d_{boundary}$ in Figure 3.2). Figure 3.2b shows the distribution of $d_{boundary}$ values for the same nanoflake in Figure 3.1. Figure 3.2c-f show the same analysis for two additional nanoflakes (Figure S3.4 shows the laser line scan position and the EQE maps for these nanoflakes). The mean $d_{boundary}$ value for 1870 deposition spots from 20 SPI-MoS_2 nanoflakes is 1.2 ± 1.4 μm, and the median $d_{boundary}$ value is 0.75 μm (Figure S3.5). Most iodine deposition spots appear directly at step edges (first bin in Figure 3.2b,d,f) and the majority of all deposition occurs <1 μm from the edge. Note, optical transmission imaging does not detect small step edge features that may otherwise appear using other imaging methods such as optical reflection (Figure S3.6) and scanning probe microscopy (Figure S12 in ref 17). Thus, it is possible that small step edge features exist near the noticeable edges in these mechanically exfoliated samples and, therefore, we hypothesize our larger $d_{boundary}$ values in Figure 3.2b,d,f overestimate the true value because iodine deposition occurs at small step edges that do not appear in the bright field transmission images. In summary, molecular reaction imaging experiments showed photogenerated holes travel 10s of microns to reach and react with iodide anions at highly active edge sites.

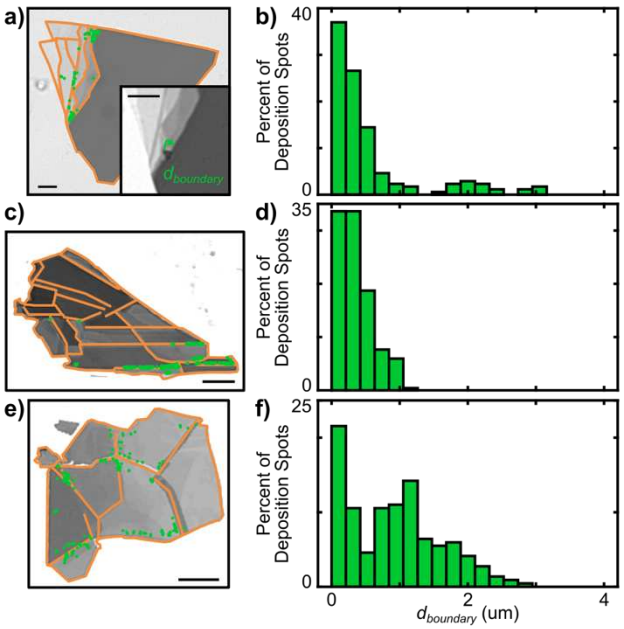

Figure 3.2: Spatial distribution analysis of iodine deposition hot spots. (a) Transmission image of an MoS_2 nanoflake. Orange lines represent physical boundaries such as perimeter and step edges. Green circles represent iodine deposition spots. The inset shows a magnified view of the top left portion of the nanoflake. (b) Histogram of the distance from each deposition spot to the nearest boundary for the data in (a). (c, e) Same as (a) but for two other MoS_2 nanoflakes. (d, f) Same as (b) but for the respective nanoflakes in (c, e). All scale bars represent 10 μm.

Another critical observation from correlated photocurrent mapping and molecular reaction imaging experiments is iodine deposition occurs at the same step edge locations regardless of whether n– or p–type domains are illuminated. For example, Figure 3.11 shows consistent iodine deposition at the same step edge as the laser spot moves from an n-type domain to a p-type domain (see additional examples in SI Figure S3.7). For the illuminated p-type domain, this observation is significant because the hole-induced iodide oxidation reaction represents a surface recombination process involving minority carriers. In this scenario, photogenerated holes in the p-type domain travel to and react at highly active edge sites for iodide oxidation instead of being collected at the ITO contact. Importantly, this observation led us to develop a hypothesis to explain performance variation among apparently smooth TMD crystals: TMD crystals with more p-type domains located near highly active edge sites will exhibit lower ensemble-level performance than TMD

crystals with less doping heterogeneity and active edge sites. To test this hypothesis, we performed a series of whole nanoflake-level photocurrent-potential measurements and correlated those results with the photocurrent maps and molecular reaction imaging results, as discussed below.

3.3.3 Single flake photocurrent–potential measurements.

Figure 3.3a illustrates the experimental setup for whole nanoflake-level photocurrent-potential (*i-E*) measurements. A 530 nm LED was positioned above the sample at the transmitted light illumination column of the inverted optical microscope. The LED light was directed through an iris to control the illumination spot size on the sample. A potentiostat measured the current from the entire electrode while a linear sweep waveform was applied (0.30 to 0.70 V vs. Ag/AgI) and the LED was chopped at 0.3 Hz.

Figure 3.3b shows *i-E* data for the three nanoflakes in Figure 3.3a that had already been characterized using photocurrent mapping and molecular reaction imaging techniques. Nanoflakes-1 and 3 exhibit anodic and cathodic photocurrents at 0.6 V, in agreement with the photocurrent maps in Figure 3.3a. We observed no photocurrent when the LED illuminated a bare ITO region located tens of microns from the nearest flake, indicating the on-off photocurrent behaviors stem from illumination of a single nanoflake. Unexpectedly, the photocurrent produced by Nanoflake-2 was nearly equivalent to Nanoflake-1 even though the EQE map of Nanoflake-2 showed significant doping heterogeneity. We expected Nanoflake-1 to produce a large anodic photocurrent because its EQE map shows dominant n-type behavior. On the other hand, we expected the anodic and cathodic currents from the n- and p-type domains within Nanoflake-2 to sum to zero, yielding an "inactive" nanoflake at the ensemble-level. This result cannot be explained by differences in light absorption due to nanoflake thickness because both nanoflakes are much thicker (>60 nm) than the penetration depth of the 530 nm excitation light (30 nm).[38,39] Instead,

we hypothesized that the whole-nanoflake photocurrent depends not only on the fraction of n- and p-type domains but also the efficiency of those domains.

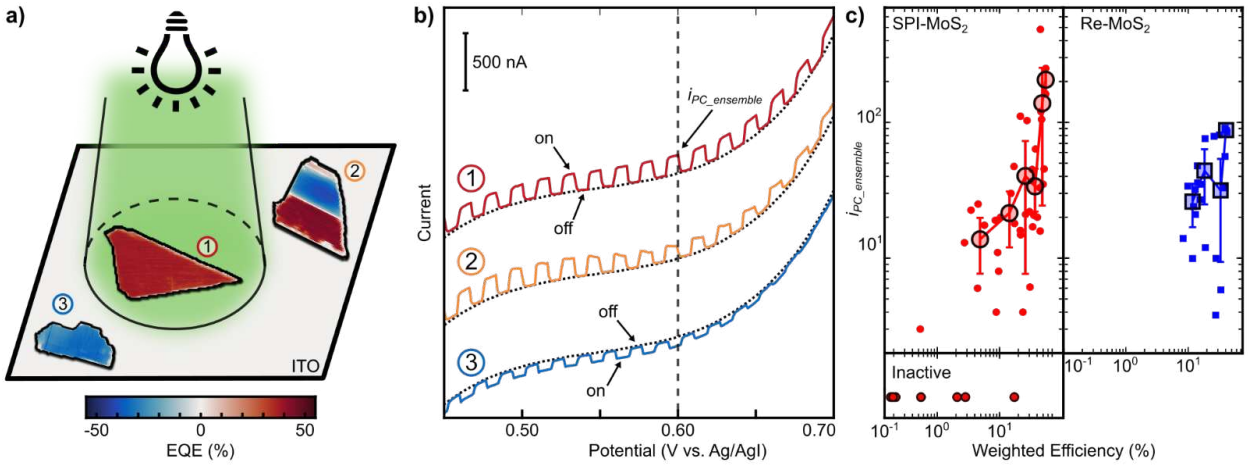

Figure 3.3: Single flake photocurrent-potential measurements. (a) Experimental scheme for single nanoflake i-E measurements. A 530 nm LED illuminates a single MoS_2 nanoflake (chopped at 0.3 Hz). The EQE maps represent photocurrent mapping results, not cartoon illustrations. (b) Single nanoflake *i-E* data from the MoS_2 nanoflakes labeled 1, 2, and 3 in panel (a). The black, dashed line represents the dark current measured from the entire ITO electrode. The potential range is limited for clarity to emphasize the photocurrent magnitude at the same potential used for photocurrent mapping and molecular reaction imaging experiments (0.6 V, indicated by vertical dashed grey line). $i_{PC\_ensemble}$ represents the whole nanoflake-level photocurrent at 0.6 V. (c) $i_{PC\_ensemble}$ versus weighted EQE efficiency for naturally occurring (SPI-MoS_2) and synthetic Re-doped (Re-MoS_2). The small symbols represent individual nanoflake values. The large symbols represent binned and averaged values to show the general trend. The bottom panel includes data points for inactive SPI–MoS_2 nanoflakes with $i_{PC\_ensemble} = 0$ nA that could not be plotted on a log scale.

To further understand how the abundance and efficiency of n- and p-type domains influences whole-nanoflake photocurrents, we performed the following quantitative analysis. First, we histogrammed the EQE map of each nanoflake into 5% EQE bins ranging from –100% to +100% EQE (41 total bins, Figure 3.4b) to generate the n- and p-type efficiency distribution of each nanoflake. Next, we normalized the bin height to the total number of pixels in the EQE map such that the bin magnitude reflects the areal fraction of the nanoflake. Finally, we calculated the weighted EQE efficiency of each nanoflake using Eq. 3.1, where EQE_i and A_i represent the EQE value and areal fraction (or height) of bin i, respectively. The weighted EQE efficiency is a single

value that accounts for not only how many n– and p–type domains exist within the nanoflake but also the efficiency of these domains.

$$Weighted\ EQE\ Efficiency = \sum_{i=1}^{41}(EQE_i \times A_i) \qquad \text{Eq. 3.1}$$

Next, we examined the correlation between the performance of each nanoflake under whole-flake illumination and the single nanoflake weighted EQE efficiency, which accounts for intra-nanoflake performance heterogeneity. Figure 3.3c plots the single nanoflake photocurrent at 0.60 V ($i_{PC\_ensemble}$ in Figure 3.3b, which is the same potential used for photocurrent mapping and molecular reaction imaging experiments) versus the weighted EQE efficiency of the same nanoflake. We observed a clear positive correlation between $i_{\mathrm{PC\_ensemble}}$ and weighted EQE efficiency, indicating nanoflakes with a larger fraction of high-efficiency n-type domains or p-type domains produce more anodic or cathodic photocurrent, regardless of the amount of doping heterogeneity. This trend also explains why the anodic photocurrent of Nanoflake-2 is nearly equal to Nanoflake-1 in Figure 3.3b. The weighted EQE efficiency of Nanoflake-2 is 13 % whereas Nanoflake-1 is 40 %. Although the absolute magnitudes are not correct, the key point is that the weighted EQE efficiency of Nanoflake-2 accounts for the area fraction of high efficiency domains and thus predicts an anodic photocurrent. The positive weighted EQE efficiency value for Nanoflake-2 is not immediately clear upon qualitative visual inspection or calculating the arithmetic mean (only 8.6 %) of the EQE map (Figure 3.3a). The n–type domains of Nanoflake-2 are more efficient and more prevalent than the high-efficiency p–type domains, accounting for the net anodic photocurrent response. In general, inactive nanoflakes have low weighted EQE efficiency values after EQE mapping analysis.

Finally, to further explain the photocurrents produced by these heterogeneous nanoflakes, we simulated the total nanoflake *i-E* curve (i_{sim}-E) assuming i_{sim} is the sum of n- and p-type diode currents from all domains in the nanoflake, $i_n(E)$ and $i_p(E)$. The individual diode currents were calculated according to Eq. 3.2 and Eq. 3.3

$$i_{\mathrm{n}}(E) = \left(i_{ph} - i_0 \left[e^{-\frac{q\left(E-E^{0'}\right)}{nkT}} - 1 \right] \right) \times A \qquad \text{Eq. 3.2}$$

$$i_{\mathrm{p}}(E) = \left(i_0 \left[e^{\frac{q(E-E^{0'})}{nkT}} - 1 \right] - i_{ph} \right) \times A \qquad \text{Eq. 3.3}$$

where i_0 is the saturation current, i_{ph} is the photogenerated minority carrier current, q is the elementary charge, (E–$E^{0'}$) is the applied potential reference to the formal potential of the iodide/tri-iodide couple (0.63 V vs. Ag/AgI) and represents the potential drop in the depletion region of the semiconductor, n is the ideality factor (set to 1.46 according to Yu and Sivula[40]), k is the Boltzmann constant, T is the temperature, and A is the area fraction of the domain. We calculated a diode curve for every bin in the EQE distribution. For example, we calculated a series of n-type and p-type diode curves (Figure 3.4c) by setting the i_l value for each curve to the EQE bin value from the histogram (Figure 3.4b) and scaling the current magnitude by the areal fraction of that bin (i.e., A_i) . The colored i_{sim}-E curves in Figure 3.4c match the corresponding bin value in Figure 3.4b. Next, we summed all the photodiode curves in Figure 3.4c and plotted the result versus the whole-nanoflake experimental data in Figure 3.4d, where the light on-off effect of light chopping has been included for clarity). Importantly, the grey simulated *i-E* curves correctly predict the sign of the experimental data for a wide variety of heterogeneous nanoflakes in Figure 3.4. The simulations for the nanoflakes in Figure 3.4 correctly predict ensemble n-type behavior for heterogeneous (Figure 3.4a) and homogeneous (Figure 3.4b) photocurrent maps as well as

ensemble p-type behavior for homogeneous (Figure 3.4c) and heterogeneous (Figure 3.4d) cases. The magnitude of the simulated curves is likely incorrect because our scanning photocurrent microscopy method does not measure the dark current from each domain, as in scanning electrochemical cell microscopy,[41,42,35] and the 1 μm spatial resolution does not fully characterize nanoscale domain heterogeneity, limiting our ability to quantify the magnitude and areal fraction of n- and p-type domains. We note that the simulated data for both the fully n–type and fully p–type case (Figure 3.4h, l) does not follow the S-shaped curve of the experimental data. This disagreement likely stems from the fact that the experimental data includes the dark current from the entire ITO electrode and the simulated curve considers only ideal n– or p–type diodes; the simulation does not include the dark current and ideality factor from the individual domains. However, the key point is that the simulation approach uses photocurrent mapping data at the single nanoflake-level to explain the whole-nanoflake photoelectrochemical behavior.

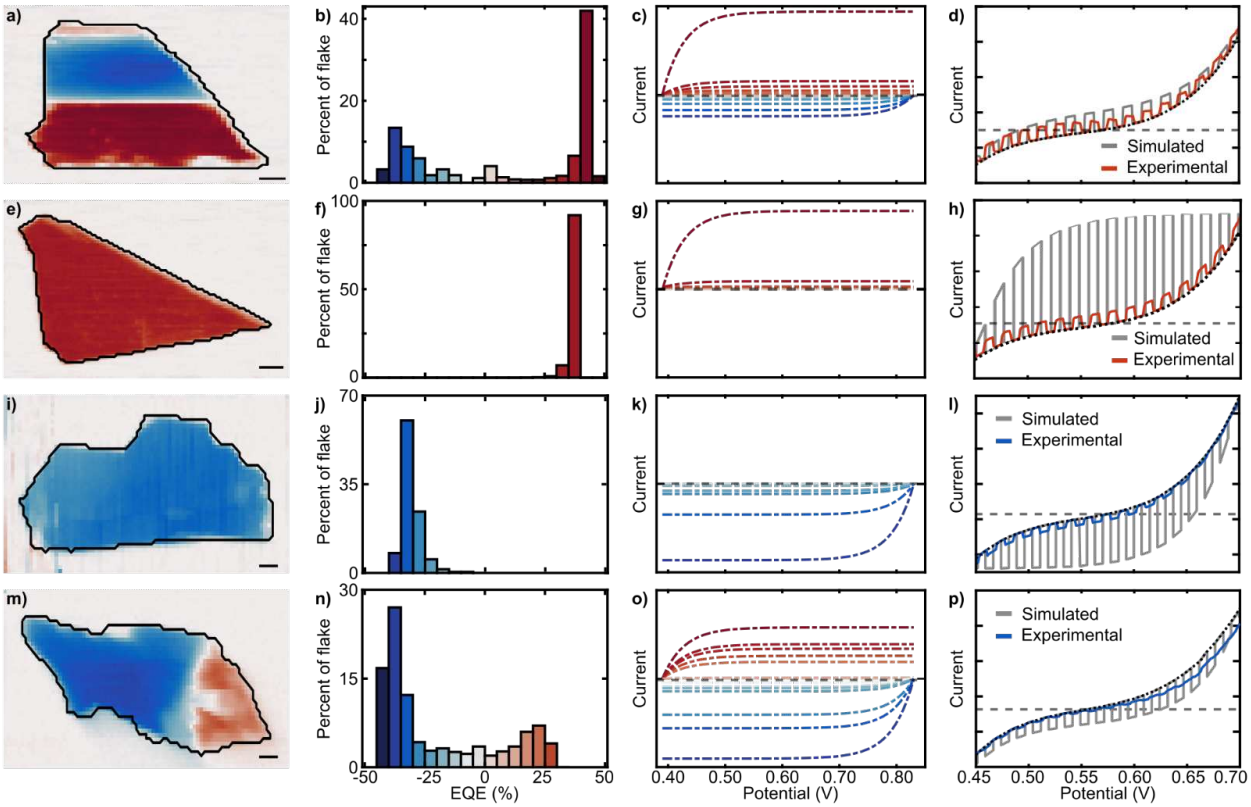

Figure 3.4: Simulating whole-nanoflake *i-E* curves from photocurrent mapping data. (a) EQE map a single MoS_2 nanoflake that contains n– and p– type domains. (b) EQE distribution values from the nanoflake in (a). All bin widths are 5% EQE. (c) Simulated photodiode curves for each bin in (b), see main text for simulation details. (d) Simulated photodiode curve (grey trace) calculated from the sum of all curves in panel (c) compared to the experimental data. The on-off effect of light chopping has been included for clarity. (e-h, i-l, m-p) show the same data as (a-d) but for three MoS_2 nanoflakes with (e-h) homogeneous n-type, (i-l) homogeneous p-type, and (m-p) heterogeneous p-type EQE maps.

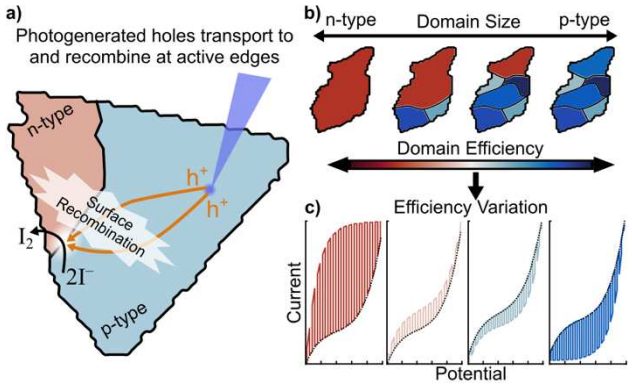

Scheme 3.1: (a) Cartoon Illustration of efficiency losses in apparently smooth TMD photoelectrodes. Photogenerated holes from p-type domains transport to active edge sites and take part in a surface recombination reaction with iodide. (b) Areal fraction and overall domain efficiency of n- and p-type domains causes efficiency variation among individual nanoflakes (c).

3.4 Conclusion

In conclusion, photocurrent mapping and molecular reaction imaging experiments provide a unifying view of efficiency losses in apparently smooth TMD photoelectrodes in iodide/tri-iodide electrolytes. Our experiments revealed a surface recombination process that remains hidden in conventional photoelectrochemical methods. Specifically, the imaging data revealed photogenerated holes in "hidden" p-type domains transport long distances to highly active edge sites for iodide oxidation instead of being collected at the ITO contact (Scheme 3.1a). Moreover, we propose that the magnitude of the efficiency loss in apparently smooth n-type crystals depends on the areal fraction of n- and p-type domains, the efficiency of those domains, and the location of those domains relative to step edges (Scheme 3.1b,c). Such effects likely remained hidden in the bulk TMD literature because scanning light spot measurements in the 1980s used >10 μm light spots[16,29,63,64], which is 30× larger than the light spot used herein and much larger than individual domain sizes. For a dominantly n-type crystal, those large light spots likely excited multiple n- and p-type domains, causing the anodic and cathodic current response from the individual domains to

sum to a small net anodic current. One explanation for the efficiency variation among domains is that impurities in bulk TMD crystals tend to segregate into islands[29], leading to local variations in doping density and photoelectrochemical properties.[65,66] Our results not only explain the origin of efficiency losses in smooth TMD photoelectrodes, but also possibly be leveraged to design electrode architectures that harness the long-range lateral charge transport property for productive photoelectrocatalytic reactions.

REFERENCES

(1) Kline, G.; Kam, K.; Canfield, D.; Parkinson, B. A. Efficient and Stable Photoelectrochemical Cells Constructed with WSe2 and MoSe2 Photoanodes. *Sol. Energy Mater.* **1981**, *4* (3), 301–308. https://doi.org/10/d87x7q.

(2) Kline, G.; Kam, K. K.; Ziegler, R.; Parkinson, B. A. Further Studies of the Photoelectrochemical Properties of the Group VI Transition Metal Dichalcogenides. *Solar Energy Materials* **1982**, *6* (3), 337–350. https://doi.org/10.1016/0165-1633(82)90039-9.

(3) Lewerenz, H. J.; Gerischer, H.; Lübke, M. Photoelectrochemistry of WSe2 Electrodes: Comparison of Stepped and Smooth Surfaces. *J. Electrochem. Soc.* **1984**, *131* (1), 100. https://doi.org/10/cgqfcc.

(4) Tenne, R.; Wold, A. Passivation of Recombination Centers in N-WSe2 Yields High Efficiency (>14%) Photoelectrochemical Cell. *Appl. Phys. Lett.* **1985**, *47* (7), 707–709. https://doi.org/10/fcxrk9.

(5) Prasad, G.; Srivastava, O. N. The High-Efficiency (17.1%) WSe2photo-Electrochemical Solar Cell. *J. Phys. D: Appl. Phys.* **1988**, *21* (6), 1028–1030. https://doi.org/10/c7k5qr.

(6) Tributsch, H. Electrochemical Solar Cells Based on Layer-Type Transition Metal Compounds: Performance of Electrode Material. *Sol. Energy Mater.* **1979**, *1* (3), 257–269. https://doi.org/10.1016/0165-1633(79)90044-3.

(7) Canfield, D.; Parkinson, B. A. Improvement of Energy Conversion Efficiency by Specific Chemical Treatments of Molybdenum Selenide (n-MoSe2) and Tungsten Selenide (n-WSe2) Photoanodes. *J. Am. Chem. Soc.* **1981**, *103* (5), 1279–1281. https://doi.org/10/fnk2st.

(8) LEWERENZ, H. J.; HELLER, A.; LEAMY, H. J.; FERRIS, S. D. Carrier Recombination at Steps in Surfaces of Layered Compound Photoelectrodes. In *Photoeffects at Semiconductor-Electrolyte Interfaces*; ACS Symposium Series; AMERICAN CHEMICAL SOCIETY, 1981; Vol. 146, pp 17–35. https://doi.org/10.1021/bk-1981-0146.ch002.

(9) Furtak, T. E.; Canfield, D. C.; Parkinson, B. A. Scanning Light-spot Analysis of the Carrier Collection in Liquid-junction Solar Energy Converters. *J. Appl. Phys.* **1980**, *51* (11), 6018–6021. https://doi.org/10/fvdfk5.

(10) Parkinson, B. A.; Furtak, T. E.; Canfield, D.; Kam, K.-K.; Kline, G. Evaluation and Reduction of Efficiency Losses at Tungsten Diselenide Photoanodes. *Faraday Discuss. Chem. Soc.* **1980**, *70* (0), 233–245. https://doi.org/10/cg82t4.

(11) Ahmed, S. M.; Gerischer, H. Influence of Crystal Surface Orientation on Redox Reactions at Semiconducting MoS2. *Electrochimica Acta* **1979**, *24* (6), 705–711. https://doi.org/10.1016/0013-4686(79)87055-3.

(12) Lewerenz, H. J.; Heller, A.; DiSalvo, F. J. Relationship between Surface Morphology and Solar Conversion Efficiency of Tungsten Diselenide Photoanodes. *J. Am. Chem. Soc.* **1980**, *102* (6), 1877–1880. https://doi.org/10/b52hqq.

(13) Kam, K. K.; Parkinson, B. A. Detailed Photocurrent Spectroscopy of the Semiconducting Group VIB Transition Metal Dichalcogenides. *J. Phys. Chem.* **1982**, *86* (4), 463–467. https://doi.org/10/fsccvh.

(14) Menezes, S.; Schneemeyer, L. F.; Lewerenz, H. J. Efficiency Losses from Carrier-type Inhomogeneity in Tungsten Diselenide Photoelectrodes. *Appl. Phys. Lett.* **1981**, *38* (11), 949–951. https://doi.org/10/bpmvbx.

(15) Van Erdewyk, M.; Sambur, J. B. Single Nanoflake Photoelectrochemistry Reveals Intrananoflake Doping Heterogeneity That Explains Ensemble-Level Photoelectrochemical Behavior. *ACS Appl. Mater. Interfaces* **2022**, *14* (20), 22737–22746. https://doi.org/10.1021/acsami.1c14928.
(16) Castellanos-Gomez, A.; Buscema, M.; Molenaar, R.; Singh, V.; Janssen, L.; Zant, H. S. J. van der; Steele, G. A. Deterministic Transfer of Two-Dimensional Materials by All-Dry Viscoelastic Stamping. *2D Mater.* **2014**, *1* (1), 011002. https://doi.org/10.1088/2053-1583/1/1/011002.
(17) Todt, M. A.; Isenberg, A. E.; Nanayakkara, S. U.; Miller, E. M.; Sambur, J. B. Single-Nanoflake Photo-Electrochemistry Reveals Champion and Spectator Flakes in Exfoliated MoSe2 Films. *J. Phys. Chem. C* **2018**, *122* (12), 6539–6545. https://doi.org/10/gdc6df.
(18) Isenberg, A. E.; Todt, M. A.; Wang, L.; Sambur, J. B. Role of Photogenerated Iodine on the Energy-Conversion Properties of MoSe2 Nanoflake Liquid Junction Photovoltaics. *ACS Appl. Mater. Interfaces* **2018**, *10* (33), 27780–27786. https://doi.org/10.1021/acsami.8b07617.
(19) Magda, G. Z.; Pető, J.; Dobrik, G.; Hwang, C.; Biró, L. P.; Tapasztó, L. Exfoliation of Large-Area Transition Metal Chalcogenide Single Layers. *Sci Rep* **2015**, *5* (1), 14714. https://doi.org/10.1038/srep14714.
(20) Velický, M.; Donnelly, G. E.; Hendren, W. R.; McFarland, S.; Scullion, D.; DeBenedetti, W. J. I.; Correa, G. C.; Han, Y.; Wain, A. J.; Hines, M. A.; Muller, D. A.; Novoselov, K. S.; Abruña, H. D.; Bowman, R. M.; Santos, E. J. G.; Huang, F. Mechanism of Gold-Assisted Exfoliation of Centimeter-Sized Transition-Metal Dichalcogenide Monolayers. *ACS Nano* **2018**, *12* (10), 10463–10472. https://doi.org/10.1021/acsnano.8b06101.
(21) Liu, F.; Wu, W.; Bai, Y.; Chae, S. H.; Li, Q.; Wang, J.; Hone, J.; Zhu, X.-Y. Disassembling 2D van Der Waals Crystals into Macroscopic Monolayers and Reassembling into Artificial Lattices. *Science* **2020**, *367* (6480), 903–906. https://doi.org/10.1126/science.aba1416.
(22) Radisavljevic, B.; Radenovic, A.; Brivio, J.; Giacometti, V.; Kis, A. Single-Layer MoS2 Transistors. *Nature Nanotech* **2011**, *6* (3), 147–150. https://doi.org/10.1038/nnano.2010.279.
(23) Yin, Z.; Li, H.; Li, H.; Jiang, L.; Shi, Y.; Sun, Y.; Lu, G.; Zhang, Q.; Chen, X.; Zhang, H. Single-Layer MoS2 Phototransistors. *ACS Nano* **2012**, *6* (1), 74–80. https://doi.org/10.1021/nn2024557.
(24) Wang, H.; Yu, L.; Lee, Y.-H.; Shi, Y.; Hsu, A.; Chin, M. L.; Li, L.-J.; Dubey, M.; Kong, J.; Palacios, T. Integrated Circuits Based on Bilayer MoS2 Transistors. *Nano Lett.* **2012**, *12* (9), 4674–4680. https://doi.org/10.1021/nl302015v.
(25) Kim, S.; Konar, A.; Hwang, W.-S.; Lee, J. H.; Lee, J.; Yang, J.; Jung, C.; Kim, H.; Yoo, J.-B.; Choi, J.-Y.; Jin, Y. W.; Lee, S. Y.; Jena, D.; Choi, W.; Kim, K. High-Mobility and Low-Power Thin-Film Transistors Based on Multilayer MoS2 Crystals. *Nat Commun* **2012**, *3* (1), 1011. https://doi.org/10.1038/ncomms2018.
(26) Fontana, M.; Deppe, T.; Boyd, A. K.; Rinzan, M.; Liu, A. Y.; Paranjape, M.; Barbara, P. Electron-Hole Transport and Photovoltaic Effect in Gated MoS2 Schottky Junctions. *Sci Rep* **2013**, *3* (1), 1634. https://doi.org/10.1038/srep01634.
(27) McDonnell, S.; Addou, R.; Buie, C.; Wallace, R. M.; Hinkle, C. L. Defect-Dominated Doping and Contact Resistance in MoS2. *ACS Nano* **2014**, *8* (3), 2880–2888. https://doi.org/10/f5whbz.
(28) Addou, R.; Colombo, L.; Wallace, R. M. Surface Defects on Natural MoS2. *ACS Appl. Mater. Interfaces* **2015**, *7* (22), 11921–11929. https://doi.org/10.1021/acsami.5b01778.

(29) Tributsch, H.; Sakata, T.; Kawai, T. Photoinduced Layer Phenomenon Caused by Iodine Formation in MoSe2: Electrolyte (Iodide) Junctions. *Electrochimica Acta* **1981**, *26* (1), 21–31. https://doi.org/10.1016/0013-4686(81)80002-3.
(30) Tolbert, C. L.; Hill, C. M. Electrochemically Probing Exciton Transport in Monolayers of Two-Dimensional Semiconductors. *Faraday Discuss.* **2022**, *233* (0), 163–174. https://doi.org/10.1039/D1FD00052G.
(31) Chaparro, A. M.; Salvador, P.; Tabernero, A.; Navarro, R.; Coll, B.; Caselles, V. Charge Recombination Imaging at the WSe2/I– Interface. *Surface Science* **1993**, *295* (3), 457–461. https://doi.org/10/ctpm9k.
(32) Chaparro, A. M.; Salvador, P.; Peter, L. M. The Role of Surface Defects in the Photooxidation of Iodide at N-MoSe2: Evidence for a Local "Autocatalytic" Effect. *J. Phys. Chem.* **1995**, *99* (17), 6677–6683. https://doi.org/10.1021/j100017a059.
(33) Salvador, P.; Chaparro, A. M.; Mir, A. Digital Imaging of the Effect of Photoetching on the Photoresponse of N-Type Tungsten Diselenide and Molybdenum Diselenide Single Crystal Electrodes. *J. Phys. Chem.* **1996**, *100* (2), 760–768. https://doi.org/10/fhvs5p.
(34) Chaparro, A. M.; Salvador, P.; Mir, A. The Scanning Microscope for Semiconductor Characterization: Photocurrent, Photovoltage and Electrolyte Electroreflectance Imaging at the n-MoSe2/I– Interface. *J. Electroanal. Chem.* **1997**, *424* (1), 153–157. https://doi.org/10/cbf5rw.
(35) Hill, J. W.; Hill, C. M. Directly Visualizing Carrier Transport and Recombination at Individual Defects within 2D Semiconductors. *Chem. Sci.* **2021**, *12* (14), 5102–5112. https://doi.org/10.1039/D0SC07033E.
(36) Menezes, S.; DiSalvo, F. J.; Miller, B. Photoelectrochemical Compatibility of n - WSe2 and n - MoSe2 with Various Redox Systems. *J. Electrochem. Soc.* **1980**, *127* (8), 1751. https://doi.org/10/bzzwkd.
(37) Palummo, M.; Bernardi, M.; Grossman, J. C. Exciton Radiative Lifetimes in Two-Dimensional Transition Metal Dichalcogenides. *Nano Lett.* **2015**, *15* (5), 2794–2800. https://doi.org/10.1021/nl503799t.
(38) Frindt, R. F.; Yoffe, A. D.; Bowden, F. P. Physical Properties of Layer Structures : Optical Properties and Photoconductivity of Thin Crystals of Molybdenum Disulphide. *Proc. R. Soc. A.* **1963**, *273* (1352), 69–83. https://doi.org/10.1098/rspa.1963.0075.
(39) Beal, A. R.; Hughes, H. P. Kramers-Kronig Analysis of the Reflectivity Spectra of 2H-MoS2, 2H-MoSe2 and 2H-MoTe2. *J. Phys. C: Solid State Phys.* **1979**, *12* (5), 881–890. https://doi.org/10.1088/0022-3719/12/5/017.
(40) Yu, X.; Sivula, K. Photogenerated Charge Harvesting and Recombination in Photocathodes of Solvent-Exfoliated WSe2. *Chem. Mater.* **2017**, *29* (16), 6863–6875. https://doi.org/10/gbwv4z.
(41) Hill, J. W.; Hill, C. M. Directly Mapping Photoelectrochemical Behavior within Individual Transition Metal Dichalcogenide Nanosheets. *Nano Lett.* **2019**, *19* (8), 5710–5716. https://doi.org/10.1021/acs.nanolett.9b02336.
(42) Hill, J. W.; Fu, Z.; Tian, J.; Hill, C. M. Locally Engineering and Interrogating the Photoelectrochemical Behavior of Defects in Transition Metal Dichalcogenides. *J. Phys. Chem. C* **2020**, *124* (31), 17141–17149. https://doi.org/10.1021/acs.jpcc.0c05235.
(43) Addou, R.; McDonnell, S.; Barrera, D.; Guo, Z.; Azcatl, A.; Wang, J.; Zhu, H.; Hinkle, C. L.; Quevedo-Lopez, M.; Alshareef, H. N.; Colombo, L.; Hsu, J. W. P.; Wallace, R. M.

Impurities and Electronic Property Variations of Natural MoS2 Crystal Surfaces. *ACS Nano* **2015**, *9* (9), 9124–9133. https://doi.org/10.1021/acsnano.5b03309.

CHAPTER 4: ANSWERING OLD QUESTIONS WITH NEW TECHNIQUES: UNDERSTANDING PERFORMANCE-LIMITING FACTORS IN TRANSITION METAL DICHALCOGENIDE PHOTOELECTROCHEMICAL SOLAR CELLS[iv]

4.1 Introduction

1980s: Edge sites are recombination centers: Fact or fiction?

The working principles of bulk n-type TMD|I^-,I_3^-|Pt cells are as follows: (1) illumination produces electrons and holes in the semiconductor; (2) photogenerated holes move to the solid/liquid interface and react with surface-adsorbed iodide species ($2I^- + 2h^+ \rightarrow I_2$); (3) surface adsorbed iodine reacts with solution phase iodide to form tri-iodide ($I_2 + I^- \rightarrow I_3^-$); (4) photogenerated electrons extracted from the semiconductor move through the external circuit and reduce I_3^- at the Pt electrode.

In 1978, Gobrecht and Gerischer grew $MoSe_2$ crystals via vapor transport using Br_2 as the transport agent and reported a 3.5 % efficient photoelectrochemical solar cell in an iodide/tri-iodide electrolyte.[1] Tenne and Wold photoetched WSe_2 crystals in perchloric acid under positive bias, creating a presumably "spongy" WO_3 surface that could be removed by immersing the crystal in hot KOH.[2] The significant performance enhancement (>14%-efficient cell) was attributed to less-reflective and well-defined sharp edges that did not contribute to recombination like native step-edges. These results suggest–step-edges have the capability of being either beneficial or detrimental to cell performance. Prasad and Srivastava photo-etched n-WSe_2 in aqua regia and reported a 17% efficient n-WSe_2|I^-,I_3^-|Pt cell with a high >32 mA/cm^2 short circuit current

[iv] This chapter is part of a manuscript that has submitted for publication to Current Opinion in Electrochemistry. Michael Van Erdewyk, Dakota Lorenz, and Justin B. Sambur conceptualized and wrote the manuscript. Portions of Section 4.1 was incorporated earlier in this dissertation as part of Chapter 1, Section 1.2.2. The full-text is contained here.

density.[3] Carefully cleaving crystals to achieve smooth surfaces, Kline et al. reported fill factors >0.75 in n-WSe_2|I^-,I_3^-|Pt cells.[4,5] They also showed that $MoSe_2$ cells could operate for over a month with no visible degradation of the electrode surface.[4]

Despite the outstanding performance of TMD|I^-,I_3^-|Pt cells, a consensus emerged that highly stepped or imperfect crystals produced lower photocurrents and fill factors than apparently smooth crystals.[1,6,4,5,2,3] Gerischer argued that Mo *d*-orbitals extended into the electrolyte at exposed step-edges and participated in electron exchange with tri-iodide species.[7] However, anecdotal evidence in literature suggests that crystal surface morphology alone could not explain performance variation among TMD|I^-,I_3^- cells. For example, Parkinson commented "some crystals which have areas apparently free of surface defects when observed with optical microscopy can still show considerable variation in carrier collection."[8] Bicelli and Razzini remarked "a layer-type semiconductor photoanode, which has an apparently defect-free, smooth surface, does not necessarily give high output characteristics, as is often assumed"[9] and, furthermore, "some crystals having smooth surfaces on a microscopic scale have much lower performance and that this cannot be improved through surface treatments."[10] These ensemble-level observations motivated spatially resolved photoelectrochemical studies to investigate the relationship between bulk crystal properties, surface morphology, and solar cell performance.

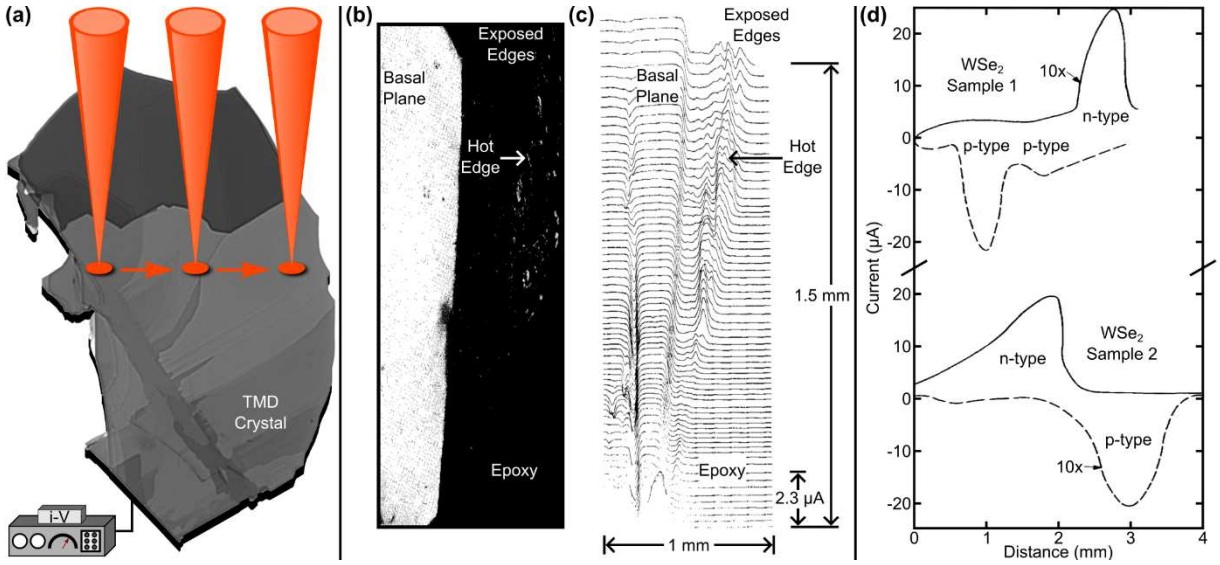

Figure 4.1: a) Cartoon illustration of scanning photocurrent microscopy of a TMD|I^-,I_3^- solar cell. The red light cones represent a focused laser spot moving across a TMD photoelectrode (e.g., MoS_2 or WSe_2). **b)** Photograph and **c)** photocurrent line scan data from a WSe_2|I^-,I_3^- with smooth and highly stepped regions. (c-d) Adapted from *J. Appl. Phys.* 51, 6018-6021 (1980), with the permission of AIP Publishing. **d)** Photocurrent line scan data from the same region of two different WSe_2 crystals. The solid line and dashed lines represent photocurrent measured at 0.1 and -1.4 V vs. $E_{I/I2}$, respectively. Adapted from *Appl. Phys. Lett.* 38, 949 (1981), with the permission of AIP Publishing.

In 1980, Furtak and Parkinson adapted spatially resolved carrier collection measurements for solid-state solar cells to n-GaAs and n-WSe_2 photoelectrochemical cells.[6] Figure 4.1a shows the general principle of scanning photocurrent microscopy measurements. By scanning a laser across a semiconducting sample, supra-bandgap illumination generates electrons and holes only within the illumination volume of the semiconductor. Typically, a potentiostat measures the total current at a fixed applied potential as a function of illumination position, yielding a photocurrent map. Those maps represent the total current flowing through the cell upon generating carriers in different microscopic regions of the crystal; the photocurrent map does not directly image where photogenerated electrons or holes react at the solid/electrolyte interface. The method does not spatially resolve the dark current, therefore, neglecting local dark current contributions to the

photocurrent response. Nonetheless, scanning photocurrent microscopy became a powerful technique to study how surface morphology affects performance of layered TMD while controlling the carrier generation location relative to a feature of interest (e.g., step-edges in Figure 4.1a).

Figure 4.1b,c shows the first example of scanning photocurrent microscopy data of a $WSe_2|I^-,I_3^-$ cell. The photocurrent line scans (Figure 4.1b) show high photocurrent in the smooth crystal regions (region A in Figure 4.1c) and generally low photocurrent in highly stepped areas (region B in Figure 4.1c), supporting the general literature hypothesis that recombination occurs at step-edges. Close examination of the dataset also shows that directly illuminating highly stepped sample regions can produce equivalent photocurrent magnitude as smooth basal planes, suggesting the existence of "hot edges" (see Figure 4.1c). However, A combination of the large light spot size (25 μm diameter) and inability to co-localize the photoelectrochemical data with the–local, illuminated surface structural features likely limited the authors' ability to resolve and elucidate the origin of step-edge performance variability.

Concomitantly, Menezes and Lewerenz applied scanning photocurrent microscopy to study performance variation among different specimens prepared from a single batch.[11] These samples ensemble-level electrochemical measurements revealed mixed n- and p-type crystals (even though all samples were prepared under the same reaction conditions). Figure 4.1d shows photocurrent line scan data at positive (solid line) and negative (dashed line) potentials from the same microscopic region of two different mixed n- and p-type crystals. The authors observed negligible anodic photocurrent from some regions of two different crystals under significant anodic bias even though whole-crystal illumination produced anodic photocurrent in ensemble-level current-voltage curve measurements. Under negative bias, the authors observed cathodic photocurrent in the crystal regions that did not exhibit clear n-type behavior. However, the 60,000

μm^2 laser spot size, which is five orders of magnitude larger than near-diffraction limited laser spot sizes reported in the 2020s,[12–18] prevented the authors from characterizing the n- and p-type domain sizes and carrier generation-collection behavior near step-edges.

The spatially resolved photocurrent measurements in Figure 4.1 raised several interesting questions that could help to answer the critical question "Why do some smooth TMD crystals make bad solar cells?" Furtak and Parkinson's results (Figure 4.1b,c) showed directly illuminating some highly stepped regions of n-type crystals produced larger anodic photocurrents than smooth crystal regions. *Are step-edges recombination centers or highly active for iodide oxidation? Do n- and p-type domains exist within all TMD crystals? If mixed n- and p-type domains are generally present in TMD samples, how do neighboring n- and p-type domains affect carrier generation and transport behavior parallel to the layers?* In this mini-review, we take a narrow focus on the application of spatially resolved photoelectrochemical measurements developed in the 2020s to answer decade-old questions regarding TMD|I^-,I_3^-|Pt solar cells.

4.2 Molecular Reaction Imaging to Study Hole Transport in TMD|I^-,I_3^- Solar Cells

Inspired by the early photoelectrochemical microscopy work of TMD solar cells by Parkinson and Lewerenz, our group developed a molecular reaction imaging technique that directly images where photogenerated holes react at TMD electrode surfaces.[19] This imaging modality can be coupled in a one-to-one fashion with near-diffraction-limited resolution scanning photocurrent microscopy measurements to understand carrier generation-recombination-collection behavior in TMD liquid junction solar cells.[20] Figure 4.2a,b shows the experimental scheme for molecular reaction imaging experiments, where a focused laser spot (1 μm in diameter) moves across the surface of the nanoflake while a camera acquires bright field transmission images. The large number of exfoliated TMD nanoflake entities allows us to acquire significant statistics

regarding how basal and edge/perimeter site surface morphologies affect photoelectrochemical performance. Interestingly, dark contrast pixels appear in bright field images when the laser illuminates some regions of the nanoflake (Figure 4.2e-inset). Those dark spots can be attributed to iodine film formation, as originally reported by Tributsch[21] and later characterized by our group using Raman micro-spectroscopy.[14] The iodine deposition phenomenon occurs when the local concentrations of I_2 exceed the solubility limit in the electrolyte. These deposition spots report on oxidative reactivity "hot spots", or locations where photogenerated holes preferentially transport to and react with iodide at the surface. A key observation in Figure 4.2e is that edge sites are highly active sites for iodide oxidation, which could result from an "autocatalytic" effect proposed by Salvador where I_3^- adsorbs at edge sites causing the TMD surface to become negatively charged and thus band-bending increases.[22] This increases the hole flux toward the TMD surface and decreases recombination. Figure 4.2g shows cumulative molecular reaction imaging results as the laser spot moves across a single MoS_2 nanoflake at fixed positive bias in an iodide-triiodide electrolyte. The orange arrows in Figure 4.2g represent hole transport distances ($d_{transport}$), defined as the distance between the point of hole generation (i.e., the focused laser spot) and hole-induced reactivity (i.e., the deposition spot). Surprisingly, photogenerated holes can travel as far as 45 μm to a reactivity hot spot, in agreement with recent long-range charge transport observations reported by Hill and Tolbert for similar samples.[23] *How does the observation of long range hole transport help us understand performance variation among apparently smooth TMD samples?*

To answer that question, we performed correlated photocurrent microscopy measurements on the same nanoflake. The photocurrent map in Figure 4.2d shows n- and p-type domains exist within the same nanoflake, as evidenced by positive (anodic) and negative (cathodic) external

quantum efficiency (EQE) values at a fixed bias, consistent with the line scan data reported by Lewerenz in Figure 4.1d. Our results consistently show over 48 nanoflakes that iodine deposition occurs at step-edges, regardless of the underlying n- or p-type domain character. Importantly, overlaying the molecular reaction imaging results on the photocurrent map (Figure 4.2h) further reveals that photogenerated holes in p-type domains transport to highly active edge sites and react with iodide to form iodine, which represents a surface recombination process.

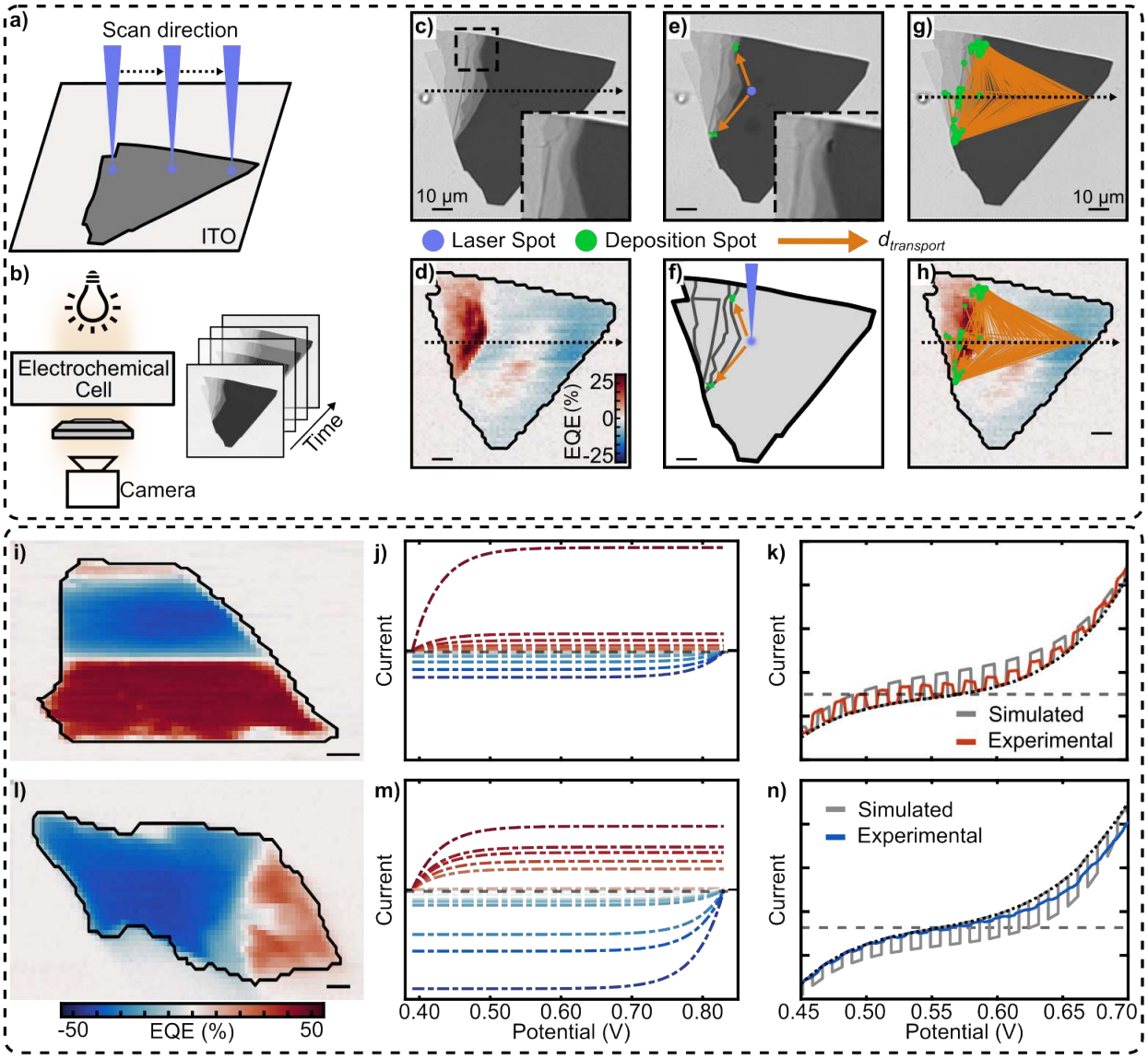

Figure 4.2: (top panel, a-h) Photocurrent mapping and molecular reaction imaging of a single MoS_2 nanoflake. (a) Cartoon illustration of a 425 nm excitation laser scanning across a nanoflake in a point-by-point fashion for 2D photocurrent mapping and 1D molecular reaction imaging line scan experiments. (b) Cartoon illustration of the bright field transmission imaging sequence during molecular reaction imaging. (c) Transmission image and (d) EQE map of a single MoS_2 nanoflake before a molecular reaction imaging experiment. The black dashed arrow in (c-d) indicates the laser line scan direction. The inset in (c) shows a magnified view of the nanoflake region indicated by the black dashed box. (e) Transmission image of the same MoS_2 nanoflake at a different excitation location during a molecular reaction imaging experiment. The purple circle, green shaded pixel regions, and the orange arrows represent the laser position, iodine deposition spots, and hole transport distance from the laser centroid to the deposition spot ($d_{transport}$), respectively. The dark contrast pixels in the inset images show the iodine deposition spots. (f) Cartoon illustration depicting the carrier generation, hole transport, and hole-induced iodine formation process. (g-h) Cumulative results of a molecular reaction imaging experiment, where all iodine deposition spots and $d_{transport}$ vectors are overlayed on the (g) transmission image and (h) EQE

map. (bottom panel, i-n) Simulating whole-nanoflake *i-E* curves from photocurrent mapping data. (i) EQE map of a single MoS_2 nanoflake that contains n– and p– type domains. (j) Simulated photodiode curves. (k) Simulated photodiode curve (grey trace) calculated from the sum of all curves in panel (j) compared to the experimental data. The on-off effect of light chopping has been included for clarity. (l, m, n) show the same data as (i, j, k) but for an MoS_2 nanoflake with heterogeneous p-type EQE maps. Adapted with permission from Ref. 19.

The observations in Figure 4.2c-h, which were observed over multiple MoS_2 nanoflakes, led us to develop the following hypothesis: TMD crystals with more p-type domains located near highly active edge sites will exhibit lower ensemble-level performance than TMD crystals with less doping heterogeneity and active edge sites. To test this hypothesis, we performed whole nanoflake-level photocurrent-potential measurements and correlated those results with the photocurrent maps and molecular reaction imaging results. To do so, We first measured the whole-nanoflake photocurrent-potential (*i*-V) curve and then simulated the total nanoflake current by modelling and summing each n- and p-type domain as a photodiode (Figure 4.2j,m). Figure 4.2k,n shows the experimental *i*-V curves and simulated results for two different nanoflake cases. Our weighted efficiency method correctly predicts the sign (n-type or p-type) of the whole-nanoflake-level behavior for a wide variety of heterogeneous nanoflakes. Hence, molecular reaction imaging and photocurrent microscopy provided key insight into the heterogeneous behaviors: *both* the size and efficiency of n- and p-type domains dictate whole-nanoflake-level behavior. Our simulations do not quantitatively agree with the data likely because scanning photoelectrochemical microscopy does not measure the local dark current from individual n- and p-type domains. Next, we discuss one technique that overcomes the dark current limitations: scanning electrochemical cell microscopy (SECCM).

4.3 SECCM Measurements of Edge Site Reactivity in TMD Solar Cells

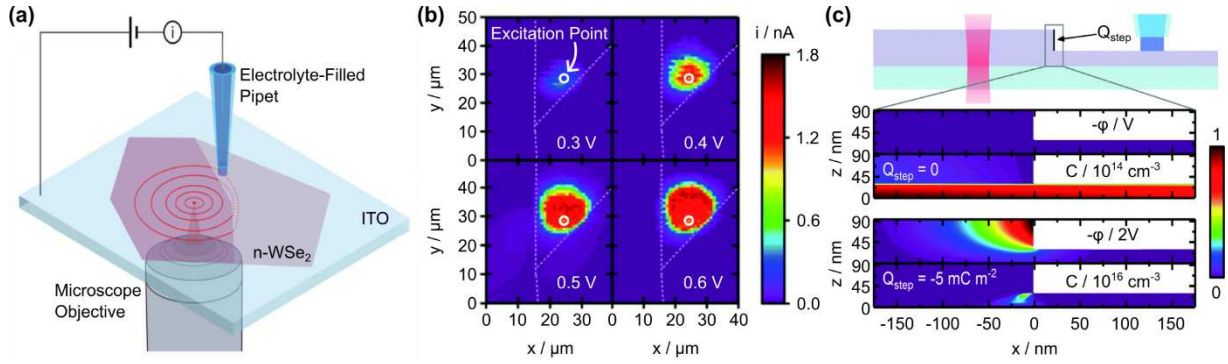

Figure 4.3: Carrier Generation-Tip Collection Scanning Electrochemical Cell Microscopy (CG-TC SECCM). (a) A focused laser excites a fixed position of the TMD nanoflake while an SECCM tip scans above the sample surface. (b) CG-TC SECCM photocurrent images with the photoexcitation located near a triangular boundary within an n-WSe_2 nanosheet. The white dashed lines represent step-edge boundaries. (c) Simulated potential (φ) and hole concentration (C) profiles in the vicinity of the step-edge in the absence or presence of a 5 mC m^{-2} surface charge. Adapted from Ref. 43 with permission from the Royal Society of Chemistry.

Here we discuss recent advances in understanding long range charge transport and edge site reactivity in TMD liquid junction solar cells using SECCM, which is an exciting and commercially available high-throughput electrochemical imaging method [24–30]. Typical SECCM measurements scan a glass pipette over a sample in a hopping-mode fashion. A 100 nm or larger electrolyte droplet protrudes from the pipette tip and contacts the sample. Effectively creating a mobile nano-electrochemical cell; all electrochemical data stems from the surface area contained within the droplet. The spatial resolution of the method depends on the contact area between the electrolyte and sample surface. One major advantage of SECCM, especially for layered TMD samples, is *z*-height is measured at the same time as electrochemical data, providing key insight into structure-property relationships like electron transfer kinetics versus layer thickness.[31,32] Several research groups utilized SECCM to study TMD materials.[33–41] For example, Bentley and co-workers showed that the edge plane of MoS_2 possesses greatly enhanced activity for the hydrogen evolution reaction compared to the basal plane,[33,34] supporting earlier scanning

tunneling microscopy studies.[42] Below we highlight SECCM imaging of TMD|iodide-based solar cells focusing on carrier generation and collection near step-edges.

Hill and co-workers developed a carrier-generation tip-collection SECCM (CG-TC-SECCM) methodology that uses a focused laser to spatially control carrier generation and the SECCM electrolyte droplet to spatially define the collection area (Figure 4.3a). In a typical experiment, the excitation point is fixed while the SECCM tip moves above the sample. Hill and Hill applied CG-TC-SECCM to study charge transport within basal planes and across step-edges of TMD materials.[43] Figure 4.3b shows potential-dependent CG-TC-SECCM maps near the same triangular step-edge boundary of a single WSe_2 nanoflake. The heat map contrast expands vertically with increasing positive bias, meaning the authors detect more anodic photocurrent with increasing positive bias but only within the single domain where carriers are photogenerated by the focused laser. Importantly, their results showed that photogenerated holes do not cross over or beneath a step-edge and react at the adjacent basal plane surface. To explain this observation, Hill and Hill modelled a negative surface charge at the step-edge (Figure 4.3c-bottom panel), which creates an electric field within the WSe_2 nanosheet that drives photogenerated holes toward the step-edge, where electron-hole recombination occurs. This observation supports our results that photogenerated holes can transport 10s of microns parallel to the layers, perhaps driven by an electric field at the step-edge.

Hill and Tolbert also showed that step-edges in WSe_2 nanosheets can be highly active for iodide oxidation. They utilized CG-TC-SECCM to measure the photocurrent response upon illuminating regions of varying thickness within a single nanoflake. Figure 4.4a shows an optical reflection image of the sample with WSe_2 layer thicknesses labelled in white. Figure 4.4b shows CG-TC-SECCM maps as a function of applied potential. The map acquired at 0.60 V vs. Ag/AgI

shows that the step-edge feature located between the 60-layer and 5-layer-thick regions produces higher photocurrent response than the surrounding basal planes. This phenomenon also occurs in the left side of the same map at the step-edge located between the 28-layer and 7-layer-thick regions. These observations also support our scanning photocurrent mapping data that photogenerated holes transport >10 μm and react at highly active step-edge sites.

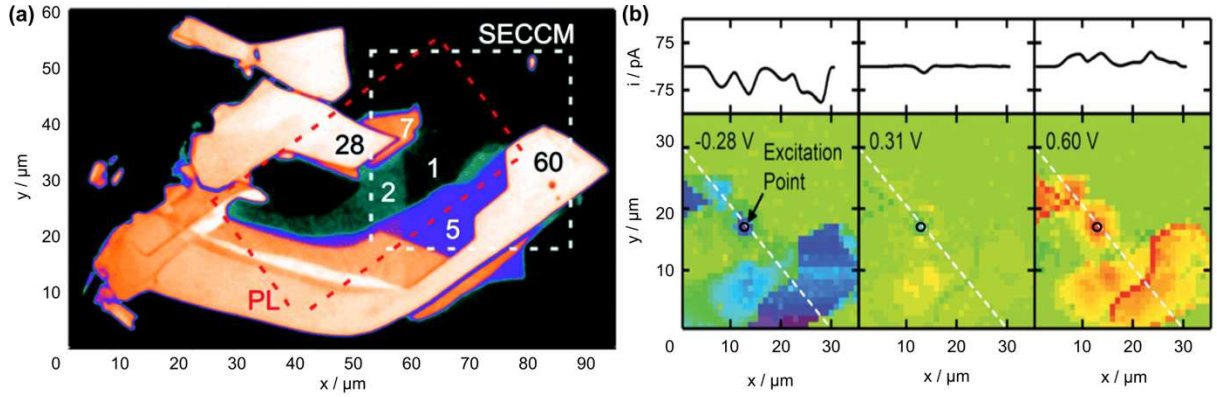

Figure 4.4: CG-TC SECCM imaging of hole transport within a WSe_2 nanoflake. (a) False color optical reflection image of an exfoliated WSe_2 structure. The numbers indicate layer thickness as determined via atomic force microscopy images. (b) CG-TC SECCM maps at different potentials obtained in the vicinity of a chopped (20 Hz), focused 633 nm laser (0.4 mW). All SECCM data was obtained using a ~600 nm diameter probe filled with 0.1 M NaI, 0.01 M I_2. Adapted from Ref. 22 with permission from the Royal Society of Chemistry.

4.4 Conclusions and Outlook

Scanning photocurrent microscopy and SECCM techniques both produce photocurrent maps that indicate long-range hole transport parallel to TMD layers is possible. However, directly comparing results from these different techniques can be challenging. Both techniques employ a focused laser spot for charge carrier generation. However, in scanning photocurrent microscopy, the electrolyte contacts the entire nanoflake and, therefore, carriers can transport to and react with iodide or tri-iodide species at all available surface sites. Electric field gradients presumably exist at near-surface regions of the entire nanoflake. *How might scanning photocurrent microscopy*

maps change if only a portion of the nanoflake were in contact with the electrolyte? In CG-TC-SECCM, photogenerated electrons and holes can only react at the solid/electrolyte interface defined by the droplet area. Space charge regions presumably only exist at microscopic regions surrounding the electrolyte droplet. *How might SECCM photocurrent maps change if more electrolyte droplets were introduced on the nanoflake surface?* The key point is that several fundamental processes contribute to signal generation in both methods and, therefore, directly comparing "photocurrent maps" can be challenging.

Another important consideration is whether the data obtained from either technique can be extrapolated to practical solar energy conversion conditions. The focused, intense monochromatic laser illumination can induce a high-level injection condition where the photogenerated majority carrier concentration exceeds the thermally excited population under dark conditions.[44] Under these conditions, carriers move via diffusion along a concentration gradient instead of drift along an electric-field gradient in the space charge region, which is the case for bulk TMD solar cells under low light illumination conditions. It is unclear how the long-range transport data obtained under the unique conditions of both measurement modes, translates to practical TMD-based photoelectrochemical solar cells under realistic solar flux illumination conditions. Despite these open questions, we believe both scanning photocurrent microscopy and SECCM techniques have answered open questions regarding the origin of performance variation in TMD|I^-,I_3^-|Pt solar cells. Specifically, these methods revealed that small p-type domains exist within nominally n-type TMD crystals, and photogenerated holes in these p-type domains can transport >10 mm to highly active edge sites for iodide oxidation, which represents a surface recombination reaction. Going forward, both techniques provide an unprecedented real-time view of a wide range of photoelectrode materials under working photoelectrochemical cell conditions. We envision a new frontier of

photoelectrochemistry knowledge generation when both techniques are combined on a single microscope platform.

REFERENCES

[1] J. Gobrecht, H. Tributsch, H. Gerischer, Performance of Synthetical n-MoSe2 in Electrochemical Solar Cells, J. Electrochem. Soc. 125 (1978) 2085. https://doi.org/10/ddtbz9.

[2] R. Tenne, A. Wold, Passivation of recombination centers in n-WSe2 yields high efficiency (>14%) photoelectrochemical cell, Appl. Phys. Lett. 47 (1985) 707–709. https://doi.org/10/fcxrk9.

[3] G. Prasad, O.N. Srivastava, The high-efficiency (17.1%) WSe2photo-electrochemical solar cell, J. Phys. D: Appl. Phys. 21 (1988) 1028–1030. https://doi.org/10/c7k5qr.

[4] G. Kline, K. Kam, D. Canfield, B.A. Parkinson, Efficient and stable photoelectrochemical cells constructed with WSe2 and MoSe2 photoanodes, Solar Energy Materials. 4 (1981) 301–308. https://doi.org/10/d87x7q.

[5] G. Kline, K.K. Kam, R. Ziegler, B.A. Parkinson, Further studies of the photoelectrochemical properties of the group VI transition metal dichalcogenides, Sol. Energy Mater. 6 (1982) 337–350. https://doi.org/10/fn3zxw.

[6] T.E. Furtak, D.C. Canfield, B.A. Parkinson, Scanning light-spot analysis of the carrier collection in liquid-junction solar energy converters, J. Appl. Phys. 51 (1980) 6018–6021. https://doi.org/10/fvdfk5.

[7] S.M. Ahmed, H. Gerischer, Influence of crystal surface orientation on redox reactions at semiconducting MoS2, Electrochimica Acta. 24 (1979) 705–711. https://doi.org/10.1016/0013-4686(79)87055-3.

[8] B.A. Parkinson, T.E. Furtak, D. Canfield, K.-K. Kam, G. Kline, Evaluation and reduction of efficiency losses at tungsten diselenide photoanodes, Faraday Discuss. Chem. Soc. 70 (1980) 233–245. https://doi.org/10/cg82t4.

[9] G. Razzini, Photocatalytic behaviour of n-MoSe2 single crystals in contact with the I–, I2 redox couple in solar photo-electrochemical cells, Journal of Power Sources. 7 (1982) 275–280. https://doi.org/10.1016/0378-7753(82)80016-5.

[10] L.P. Bicelli, Razzini, G., Surface behaviour of n-MoSe2 photoanodes in photoelectrochemical solar cells, Surface Technology. 16 (1982) 37–47. https://doi.org/10.1016/0376-4583(82)90093-0.

[11] S. Menezes, L.F. Schneemeyer, H.J. Lewerenz, Efficiency losses from carrier-type inhomogeneity in tungsten diselenide photoelectrodes, Appl. Phys. Lett. 38 (1981) 949–951. https://doi.org/10/bpmvbx.

[12] J. M. Velazquez, J. John, D. V. Esposito, A. Pieterick, R. Pala, G. Sun, X. Zhou, Z. Huang, S. Ardo, M. P. Soriaga, B. S. Brunschwig, N. S. Lewis, A scanning probe investigation of the role of surface motifs in the behavior of p-WSe 2 photocathodes, Energy Environ. Sci. 9 (2015) 164–175. https://doi.org/10/ggpvh4.

[13] M.A. Todt, A.E. Isenberg, S.U. Nanayakkara, E.M. Miller, J.B. Sambur, Single-Nanoflake Photo-Electrochemistry Reveals Champion and Spectator Flakes in Exfoliated MoSe2 Films, J. Phys. Chem. C. 122 (2018) 6539–6545. https://doi.org/10/gdc6df.

[14] A.E. Isenberg, M.A. Todt, L. Wang, J.B. Sambur, Role of Photogenerated Iodine on the Energy-Conversion Properties of MoSe2 Nanoflake Liquid Junction Photovoltaics, ACS Appl. Mater. Interfaces. 10 (2018) 27780–27786. https://doi.org/10/gdtndb.

[15] M.V. Erdewyk, J.B. Sambur, Single Nanoflake Photoelectrochemistry Reveals Intrananoflake Doping Heterogeneity That Explains Ensemble-Level Photoelectrochemical Behavior, ACS Appl. Mater. Interfaces. 14 (2022) 22737–22746. https://doi.org/10.1021/acsami.1c14928.
[16] L. Wang, J.B. Sambur, Efficient Ultrathin Liquid Junction Photovoltaics Based on Transition Metal Dichalcogenides, Nano Lett. 19 (2019) 2960–2967. https://doi.org/10/gf2wsk.
[17] L. Wang, M. Schmid, Z.N. Nilsson, M. Tahir, H. Chen, J.B. Sambur, Laser Annealing Improves the Photoelectrochemical Activity of Ultrathin MoSe2 Photoelectrodes, ACS Appl. Mater. Interfaces. 11 (2019) 19207–19217. https://doi.org/10/ggp7cq.
[18] L. Wang, M. Tahir, H. Chen, J.B. Sambur, Probing Charge Carrier Transport and Recombination Pathways in Monolayer MoS2/WS2 Heterojunction Photoelectrodes, Nano Letters. (2019). https://doi.org/10/ggp65d.
[19] Z. Nilsson, M. Van Erdewyk, L. Wang, J.B. Sambur, Molecular Reaction Imaging of Single-Entity Photoelectrodes, ACS Energy Lett. (2020) 1474–1486. https://doi.org/10/ggsp89.
[20] M. Van Erdewyk, J.B. Sambur, Molecular Reaction Imaging of a Surface Recombination Process Explains Performance Variation Among Smooth MoS2 Photoelectrodes, Journal of The Electrochemical Society. Submitted (2022).
[21] H. Tributsch, T. Sakata, T. Kawai, Photoinduced layer phenomenon caused by iodine formation in MoSe2: electrolyte (iodide) junctions, Electrochimica Acta. 26 (1981) 21–31. https://doi.org/10.1016/0013-4686(81)80002-3.
[22] A.M. Chaparro, P. Salvador, L.M. Peter, The Role of Surface Defects in the Photooxidation of Iodide at n-MoSe2: Evidence for a Local "Autocatalytic" Effect, J. Phys. Chem. 99 (1995) 6677–6683. https://doi.org/10.1021/j100017a059.
[23] C.L. Tolbert, C.M. Hill, Electrochemically probing exciton transport in monolayers of two-dimensional semiconductors, Faraday Discuss. 233 (2022) 163–174. https://doi.org/10.1039/D1FD00052G.
[24] N. Ebejer, A. Guell, S. Lai, K. McKelvey, M.E. Snowden, P.R. Unwin, Scanning Electrochemical Cell Microscopy: A Versatile Technique for Nanoscale Electrochemistry and Functional Imaging, Annual Review of Analytical Chemistry. 6 (2013) 329–351. https://doi.org/10.1146/annurev-anchem-062012-092650.
[25] E. Daviddi, L.F. Gaudin, C.L. Bentley, Scanning electrochemical cell microscopy: High-resolution structure–property studies of mono- and polycrystalline electrode materials, Current Opinion in Electrochemistry. 34 (2022) 101006. https://doi.org/10.1016/j.coelec.2022.101006.
[26] C.L. Bentley, Scanning electrochemical cell microscopy for the study of (nano)particle electrochemistry: From the sub-particle to ensemble level, Electrochemical Science Advances. 2 (2021) e2100081. https://doi.org/10.1002/elsa.202100081.
[27] C.L. Bentley, M. Kang, P.R. Unwin, Scanning electrochemical cell microscopy: New perspectives on electrode processes in action, Current Opinion in Electrochemistry. 6 (2017) 23–30. https://doi.org/10.1016/j.coelec.2017.06.011.
[28] O.J. Wahab, M. Kang, P.R. Unwin, Scanning electrochemical cell microscopy: A natural technique for single entity electrochemistry, Current Opinion in Electrochemistry. 22 (2020) 120–128. https://doi.org/10.1016/j.coelec.2020.04.018.
[29] A. Kumatani, T. Matsue, Recent advances in scanning electrochemical microscopic analysis and visualization on lithium-ion battery electrodes, Current Opinion in Electrochemistry. 22 (2020) 228–233. https://doi.org/10.1016/j.coelec.2020.07.010.

[30] Y. Takahashi, A. Kumatani, H. Shiku, T. Matsue, Scanning Probe Microscopy for Nanoscale Electrochemical Imaging, Anal. Chem. 89 (2017) 342–357. https://doi.org/10.1021/acs.analchem.6b04355.
[31] M. Velický, M.A. Bissett, C.R. Woods, P.S. Toth, T. Georgiou, I.A. Kinloch, K.S. Novoselov, R.A.W. Dryfe, Photoelectrochemistry of Pristine Mono- and Few-Layer MoS2, Nano Lett. 16 (2016) 2023–2032. https://doi.org/10.1021/acs.nanolett.5b05317.
[32] M. Brunet Cabré, A.E. Paiva, M. Velický, P.E. Colavita, K. McKelvey, Electrochemical kinetics as a function of transition metal dichalcogenide thickness, Electrochimica Acta. 393 (2021) 139027. https://doi.org/10.1016/j.electacta.2021.139027.
[33] B. Tao, P.R. Unwin, C.L. Bentley, Nanoscale Variations in the Electrocatalytic Activity of Layered Transition-Metal Dichalcogenides, J. Phys. Chem. C. 124 (2020) 789–798. https://doi.org/10/ggth8h.
[34] C.L. Bentley, M. Kang, F.M. Maddar, F. Li, M. Walker, J. Zhang, P.R. Unwin, Electrochemical maps and movies of the hydrogen evolution reaction on natural crystals of molybdenite (MoS2): basal vs. edge plane activity, Chem. Sci. 8 (2017) 6583–6593. https://doi.org/10.1039/C7SC02545A.
[35] C.L. Bentley, M. Kang, P.R. Unwin, Nanoscale Structure Dynamics within Electrocatalytic Materials, J. Am. Chem. Soc. 139 (2017) 16813–16821. https://doi.org/10.1021/jacs.7b09355.
[36] Y. Takahashi, Y. Kobayashi, Z. Wang, Y. Ito, M. Ota, H. Ida, A. Kumatani, K. Miyazawa, T. Fujita, H. Shiku, Y.E. Korchev, Y. Miyata, T. Fukuma, M. Chen, T. Matsue, High-Resolution Electrochemical Mapping of the Hydrogen Evolution Reaction on Transition-Metal Dichalcogenide Nanosheets, Angewandte Chemie International Edition. 59 (2020) 3601–3608.
[37] Y. Liu, C. Jin, Y. Liu, K.H. Ruiz, H. Ren, Y. Fan, H.S. White, Q. Chen, Visualization and Quantification of Electrochemical H_2 Bubble Nucleation at Pt, Au, and MoS_2 Substrates, ACS Sens. 6 (2021) 355–363. https://doi.org/10.1021/acssensors.0c00913.
[38] J.W. Hill, C.M. Hill, Directly Mapping Photoelectrochemical Behavior within Individual Transition Metal Dichalcogenide Nanosheets, Nano Lett. 19 (2019) 5710–5716. https://doi.org/10.1021/acs.nanolett.9b02336.
[39] C.L. Bentley, R. Agoston, B. Tao, M. Walker, X. Xu, A.P. O'Mullane, P.R. Unwin, Correlating the Local Electrocatalytic Activity of Amorphous Molybdenum Sulfide Thin Films with Microscopic Composition, Structure, and Porosity, ACS Appl. Mater. Interfaces. 12 (2020) 44307–44316. https://doi.org/10.1021/acsami.0c11759.
[40] L.E. Strange, J. Yadav, S. Garg, P.S. Shinde, J.W. Hill, C.M. Hill, P. Kung, S. Pan, Investigating the Redox Properties of Two-Dimensional MoS_2 Using Photoluminescence Spectroelectrochemistry and Scanning Electrochemical Cell Microscopy, J. Phys. Chem. Lett. 11 (2020) 3488–3494. https://doi.org/10.1021/acs.jpclett.0c00769.
[41] J.W. Hill, Z. Fu, J. Tian, C.M. Hill, Locally Engineering and Interrogating the Photoelectrochemical Behavior of Defects in Transition Metal Dichalcogenides, J. Phys. Chem. C. 124 (2020) 17141–17149. https://doi.org/10.1021/acs.jpcc.0c05235.
[42] T.F. Jaramillo, K.P. Jørgensen, J. Bonde, J.H. Nielsen, S. Horch, I. Chorkendorff, Identification of Active Edge Sites for Electrochemical H2 Evolution from MoS2 Nanocatalysts, Science. 317 (2007) 100–102. https://doi.org/10.1126/science.1141483.

[43] J.W. Hill, C.M. Hill, Directly visualizing carrier transport and recombination at individual defects within 2D semiconductors, Chem. Sci. 12 (2021) 5102–5112. https://doi.org/10.1039/D0SC07033E.
[44] M.X. Tan, C.N. Kenyon, O. Krüger, N.S. Lewis, Behavior of Si Photoelectrodes under High Level Injection Conditions. 1. Steady-State Current−Voltage Properties and Quasi-Fermi Level Positions under Illumination, J. Phys. Chem. B. 101 (1997) 2830–2839. https://doi.org/10.1021/jp962483s.

CHAPTER 5: KINETIC MODELLING OF THE PHOTOCURRENT DURING MOLECULAR REACTION IMAGING EXPERIMENTS[v]

5.1 Introduction

During the analysis of the molecular reaction imaging data contained in Chapter 3, we realized that our analysis methods did not include any consideration of the measured photocurrent during the iodine deposition process. We became curious about the various behaviors we observed in the photocurrent during these experiments and wondered if a kinetic model could be developed that would provide new knowledge about the underlying photoelectrochemical processes. A kinetic model was developed based on earlier work by Sambur and co-workers that considers a limited number of oxidation and reduction steps of iodine species.[1] The goal of this study was to develop a single kinetic model to explain the time-dependent formation and consumption of iodine and the overall photocurrent data. The results of this kinetic model would allow us to ascertain surface reaction kinetics related to the iodine deposition process. Further, the determined kinetics could be correlated to surface structural features relating to either the charge carrier generation location (i.e. the laser spot) or the iodine deposition spot. For example, if we could understand the underlying kinetics of iodine deposition we could understand why iodine deposition occurs at some step-edges but not all. This information could then be further used with atomic level methods, like transmission electron microscopy (TEM) to understand if specific atomic configurations of step-edges are more susceptible for iodine deposition. The knowledge gained from this kinetic model would help to further answer the question *"what is the role of step-edges in TMDs?"*

[v] Analysis and manuscript in process. Data and fitting work done by Michael Van Erdewyk. Development of the kinetic model by Michael Van Erdewyk and Justin Sambur.

5.2 Example Data and Experimental Methods

An example photocurrent trace is shown in Figure 5.1. The photocurrent quickly rises after the laser turns on, but after ~300ms it begins to rapidly decay. The photocurrent then crosses the magnitude of the background current (the current before the laser turns on) and moves negative. This change in sign of the photocurrent indicates that there is time-dependent evolution of the dominant photoelectrochemical processes during illumination. One possible explanation for this could be that the deposition of iodine blocks the surface of the MoS_2 that is highly active for oxidation and thus the oxidative component of the photocurrent drops off. This explanation is supported by the optical data shown in Figure 5.1, where the decrease in pixel intensity (iodine deposition causes darker contrast) is consequent with the decrease in photocurrent.

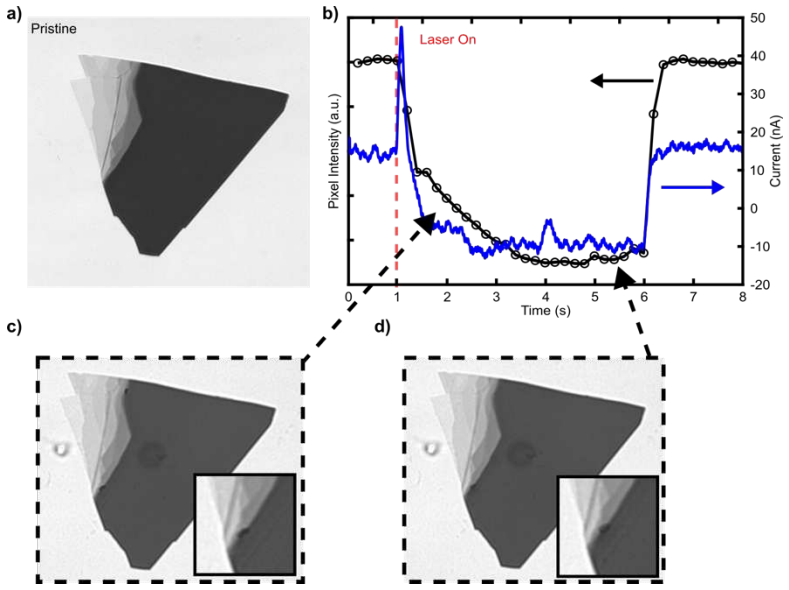

Figure 5.1: Transmission images**,** Pixel Intensity and Photocurrent trajectories during iodine deposition. a) Bright field transmission image of an MoS_2 nanoflake before iodine deposition. b) Photocurrent and pixel intensity trajectories. The black data represents the change in pixel intensity, or contrast, observed during iodine deposition. The blue line is the photocurrent measured at the same time as the imaging data (black) is collected. The red dotted line marks the time point at which the laser turns on. c) Tranmission image of the nanoflake from (a) during iodine deposition. The inset shows a magnified view of the deposition spot. d) Same as (c) but for a different point during the deposition trajectory.

5.3 Kinetic Model

The individual steps of the kinetic model are described below. The first step of the model considers the generation and separation of electrons and holes in MoS_2 (i.e. $(h^+)_b \rightarrow (h^+)_s$). We consider this step to be fast and thus occur much faster than the subsequent charge transfer across the semiconductor/electrolyte interface that contributes to the measured photocurrent. Additionally, the incident photon flux used in these experiments results in carrier generation rates that move the system into the high-injection regime.[2] For this reason, we consider the available surface holes for charge transfer to be a constant value. Next, surface holes react with surface adsorbed iodide anions to produce the one-electron oxidized species, $(I\bullet)_s$.

$$(h^+)_s + (I^-)_s \overset{k_1}{\rightarrow} (I^\bullet)_s \qquad \text{Eq. 5.1}$$

This one-electron species can react with another surface adsorbed one-electron species by Eq. 5.2 to form iodine, I_2. When the local concentration of iodine exceeds the solubility limit, it spontaneously deposits on the surface of MoS_2 giving rise to change in optical contrast that we observe on the microscope via bright field transmission imaging.

$$(I^\bullet)_s + (I^\bullet)_s \overset{k_2}{\rightarrow} I_2 \qquad \text{Eq. 5.2}$$

However, this spontaneous deposition competes with the chemical reaction of iodine with iodide anions in solution to form triiodide that can quickly adsorb to the MoS_2 surface via Eq. 5.3.

$$(I^-)_{soln} + I_2 \overset{k_3}{\leftrightarrow} (I_3^-)_s \qquad \text{Eq. 5.3}$$

We further consider two reduction reactions that contribute to the cathodic current we observe during molecular reaction imaging experiments. The first reaction, Eq. 5.4 considers the reduction of a surface adsorbed triiodide anion to iodide. In this reaction, we consider the first electron transfer to be rate limiting so the reaction is first order.[1] The second reaction, shown in

Eq. 5.5 considers the reduction of the surface adsorbed one-electron iodine species back to an iodide anion.

$$(I_3^-)_s + 2(e^-)_s \overset{k_4}{\rightarrow} 3(I^-)_s \quad \text{Eq. 5.4}$$

$$(I^\bullet)_s + (e^-)_s \overset{k_5}{\rightarrow} (I^-)_s \quad \text{Eq. 5.5}$$

With this limited model, we wrote the respective rate laws and solved for the time dependent equations for iodide, one-electron iodine, iodine, and triiodide (Eq. 5.6-5.9).

$$\frac{d[I^-]}{dt} = (k_5 \times [e^-]_s \times [I^\bullet]_t) + (3 \times k_4 \times [e^-]_s \times [I_3^-]_t) - (k_1 \times [h^+]_s \times [I^-]_t) - (k_3 \times [I_2]_t \times [I^-]_t) \quad \text{Eq. 5.6}$$

$$\frac{d[I^\bullet]}{dt} = (k_1 \times [h^+]_s \times [I^-]_t) - \left(2 \times k_2 \times [I^\bullet]_t^{\,2}\right) - (k_5 \times [e^-]_s \times [I^\bullet]_t) \quad \text{Eq. 5.7}$$

$$\frac{d[I_2]}{dt} = \left(k_2 \times [I^\bullet]_t^{\,2}\right) - (k_3 \times [I_2]_t \times [I^-]_t) \quad \text{Eq. 5.8}$$

$$\frac{d[I_3^-]}{dt} = (k_3 \times [I_2]_t \times [I^-]_t) - (k_4 \times [e^-]_s \times [I_3^-]_t) \quad \text{Eq. 5.9}$$

These equations were used with a homewritten MATLAB code to solve for a numerical solution with given initial conditions for the concentrations of $[I^-]$, $[I^\bullet]$, $[I_2]$, and $[I_3^-]$, as well as initial guesses for rate constants k_1 through k_5. The output of the solver was compared to the experimental current and the mean squared error between the two was minimized. Photocurrent time traces of interest were identified based on whether iodine deposition occurred during the laser on period of specific step in a molecular reaction imaging experiment. Detailed descriptions of molecular reaction imaging experiments and subsequent data processing are provided in Chapter 2 and Appendix B.

5.4 Results

Another photocurrent trace is shown in Figure 5.2 with an early attempt at fitting overlaid in red. Current work on the fitting procedure has been successful in fitting photocurrent of similar behavior (deemed slow rise) to that shown in Figure 5.2. However, the same model has not been able to handle the spike-and-decay behavior shown in Figure 5.1. Further iterations on the model are necessary to find a solution for both types of behavior. Only then can the optical data be incorporated to the model to provide knowledge of both the photoelectrochemical processes involved with the photocurrent and the physical processes involved iodine deposition. Work is still ongoing to develop this fitting procedure.

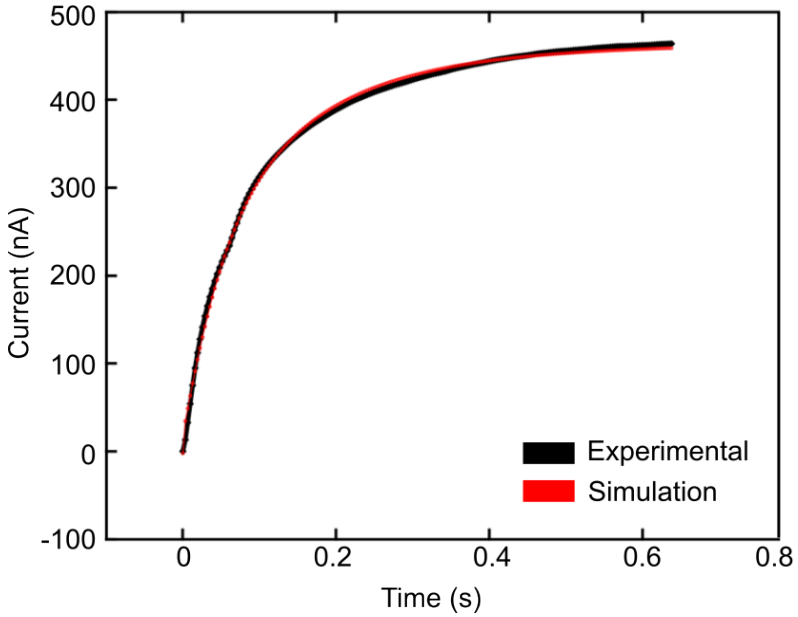

Figure 5.2: An example photocurrent trace (black line) during iodine deposition. The simulated current from the fitting model described above is shown in red.

We envision that the model will allow us to fit the overall photocurrent data and time-dependent optical signal from the formation / consumption of iodine. This information can then be correlated with the surface structure, charge carrier transport distance, and underlying doping heterogeneity profile of the nanoflake. Ideally, this will allow for us to predict where charge

carriers will react or explain why charge carriers react at some step-edges but not others (Scheme 5.1).

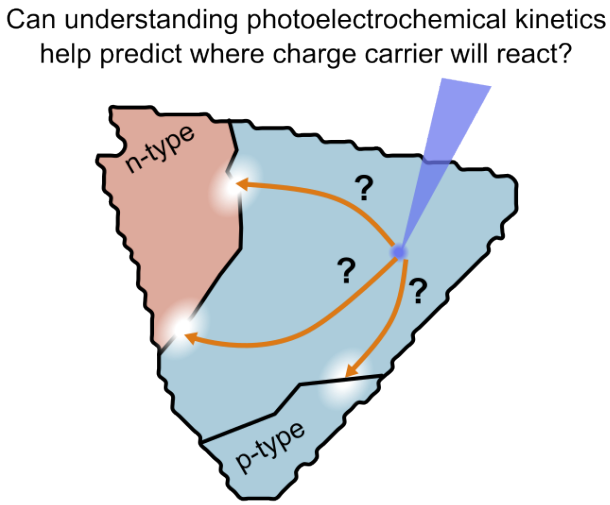

Scheme 5.1: Cartoon of an MoS_2 nanoflake during a molecular reaction imaging experiment. Kinetic modelling of the photocurrent and time-dependent iodine formation/consumption should provide knowledge as to why charge carriers react at some step-edges but not others.

REFERENCES

(1) Sambur, J. B.; Shepherd, D. P.; Hesari, M.; Erdewyk, M. V.; Choudhary, E.; Chen, P. Correlated Single-Molecule Reaction Imaging and Photocurrent Measurements Reveal Underlying Rate Processes in Photoelectrochemical Water Splitting. *J. Electrochem. Soc.* **2019**, *166* (5), H3286. https://doi.org/10/gfxz4s.

(2) Tan, M. X.; Kenyon, C. N.; Krüger, O.; Lewis, N. S. Behavior of Si Photoelectrodes under High Level Injection Conditions. 1. Steady-State Current−Voltage Properties and Quasi-Fermi Level Positions under Illumination. *J. Phys. Chem. B* **1997**, *101* (15), 2830–2839. https://doi.org/10.1021/jp962483s.

CHAPTER 6: SUMMARY AND OUTLOOK

6.1 Summary

Scanning photoelectrochemical microscopy measurements were used to reveal doping heterogeneity of mechanically exfoliated MoS_2 nanoflakes. The resulting EQE maps were used to determine both the size and efficiency of n- and p-type domains present within individual nanoflakes. Single domain photocurrent-potential curves were used to confirm the photoelectrochemical behavior of an individual domain. These measurements revealed that individual domains behave like photodiodes and thus can be simulated as such. It was determined that the photoelectrochemical behavior of the nanoflake can be correctly predicted by taking the summation of all the simulated photodiode curves for the individual domains of a single nanoflake. These results showed that the size and efficiency of a domain are important factors that affect the total performance of the nanoflake. Further XPS measurements of exfoliated MoS_2 agreed with previous literature that showed Mo:S stoichiometry to be the underlying cause of doping heterogeneity.

Molecular reaction imaging experiments were used to visualize the reversible deposition of iodine on the surface of MoS_2 nanoflakes. An image analysis algorithm was developed to relate the position of the iodine deposition to the carrier generation location (the laser spot) as well as the underlying doping heterogeneity profile and the physical morphology of the nanoflake surface. The results revealed a hidden surface recombination reaction, where photogenerated holes in p-type domains, transport and react at surface step-edges.

The results contained in this dissertation have expanded upon the work of the 1980s and provided answers to open questions that were unable to be answered without more modern

methods. Specifically, this work has answered the open question of *"what is the role of step-edges in TMD | I^-,I_3^- solar cells?"* The knowledge of edge sites being the active locations for oxidation reactions is an important contribution to the field of 2D TMDs as it provides clarification that can influence design decisions for solar energy conversion devices. For example, a device requiring high-activity photo-oxidative activity, such as a photoelectrochemical cell for iodide or carboxylate oxidation, could be designed to utilize mechanically exfoliated TMD nanoflakes. Mechanical exfoliation of TMD nanoflakes is a cheap and facile exfoliation method, and typically results in heterogeneous nanoflakes with many surface step-edges. The high-density of step-edges in exfoliated nanoflakes would be beneficial for this type of photoelectrochemical cell. At the same time, the build-up of reaction products at these step-edges could pose a problem if diffusion of reactive species to the step-edges becomes hindered. Careful consideration would need to be taken to ensure reaction products are efficiently collected and reactive species are able to reach the electrode surface. One such solution would be to design the device to include electrolyte flow.

The report of intra-flake doping heterogeneity is also broadly relevant for solar energy conversion because it could be utilized to drive both oxidation and reduction reactions concurrently. Because n- and p-type doping domains are present within individual MoS_2 nanoflakes under the same applied potential and excitation conditions, a device could be engineered to take advantage of the dual-reactivity from the domains. For example, the reductive hydrogen evolution reaction and oxidative oxygen evolution reaction could be targeted in a single device. Global illumination of a film of MoS_2 nanoflakes with doping domains could then drive both reactions at once, under the same conditions. This type of device would be incredibly useful as it would eliminate the need for separate electrodes (i.e. a photocathode and photoanode) in a photoelectrochemical cell. Instead, a single electrode could be used, both saving cost and space.

Additionally, the report of intra–flake doping heterogeneity is greatly beneficial because it can explain possible pitfalls or unexpected efficiency losses in exfoliated TMD thin films, thus answering the open question of *"why do some apparently smooth crystals behave poorly?"* Further, the correlation of doping heterogeneity to local variations in transition metal:chalcogen stoichiometry provides a route to tune the doping heterogeneity of individual samples or entire thin films by altering this stoichiometry. Controlled passivation or generation of S-vacancies in exfoliated nanoflakes would alter the transition metal:chalcogen stoichiometry thus shifting the Fermi level of the material and providing a tuning knob to create more n-type or more p-type materials. In turn, this controlled doping would result in more uniformly doped materials, thus reducing the deleterious effects of competing n- and p-type domains. Alternatively, the controlled doping could be used in conjunction with lithography/masking techniques to create patterned n- and p-type domains. This would be useful when defined n- and p-type domains are required, rather than the random size and location found in the as-exfoliated nanoflakes. For example, one could imagine creating a 50/50 n-type/p-type nanoflake to more easily separate the oxidative and reductive reaction products.

The research contained herein has both provided answers to long-standing questions and generated new knowledge about the fundamental photoelectrochemistry of TMD materials that can be beneficial to researchers looking to advance the use of TMDs in solar energy conversion devices.

6.2 Outlook

There are a number of directions that future work based on the results from Chapter 2 & 3 can be directed. Already, the Sambur group has begun to investigate how doping heterogeneity in natural TMD nanoflakes affects the corrosion of these materials. Interesting differences in both

the rate of corrosion and the form/type of corrosion have been observed between natural and synthetic MoS_2 samples. It is likely that the doping heterogeneity that is present in the natural MoS_2 sample is responsibly in some part for these differences. However correlated photocurrent mapping and corrosion studies would be needed to fully ascertain the role of doping heterogeneity.

Other work is focused on the development and use of scanning electrochemical cell microscopy (SECCM) as described in Chapter 4. SECCM measurements allow for the determination of the local electrochemical activity of small regions on the surface of TMD nanoflakes. These measurements remove the influence of the conformal electrolyte interface present in the scanning photoelectrochemical microscopy measurements discussed in this dissertation. This is a key difference as SECCM measurements can be used to further understand the role of doping heterogeneity in photogenerated charge carrier transport and reactivity because the charge carriers can only react at the semiconductor/electrolyte interface. Thus, experiments such as those in CG-TC-SECCM, where an excitation source is used that is de-coupled from the SECCM pipette tip, can be performed. These measurements would be able to address questions as to how charge carriers move across doping domain boundaries.

Alternatively, research could be focused on leveraging the doping heterogeneity present in these TMD materials to tune the function of the materials. Research could be focused on utilizing the internal electric fields present due to n- and p-type domains to controllably drive charge transport in a desired direction. For example, researchers could look to drive photogenerated electrons toward p-type domains where they are able to react with a desired molecule, like H^+ for the hydrogen evolution reaction (HER). At the same time, photogenerated holes could be driven along the internal electric field toward n-type domains where they could oxidize a target molecule.

Further, research could focus on controlling the location and size of n- and p-type domains. Variations in transition metal–chalcogen stoichiometry are the root cause of the doping heterogeneity in the TMD materials discussed herein. Therefore, a possibly facile way of controlling the doping heterogeneity is through the introduction or passivation of chalcogen vacancies. The introduction of more chalcogen vacancies would shift the fermi-level (E_F) of the material higher in energy, thus making the material more n-type and better suited for driving oxidation reactions. The opposite would be the case where already present chalcogen vacancies were passivated, thus making the material more p-type and better suited for reduction reactions like HER. An interesting opportunity arises where the target TMD materials could be "masked" before undergoing a vacancy generation or passivation treatment. This would allow for the controlled patterning of n- and p-type domains in the underlying material.

The elucidation of the size and underlying origin of doping heterogeneity in TMD nanoflakes as well as the discovery of the hidden surface recombination reaction from p-type domains discussed herein is an important finding that has great relevance for researchers in the 2D materials community. A strong understanding of the fundamental photoelectrochemistry of these materials is essential for the development of efficient devices for solar energy conversion. The research presented here take an approach to find open questions from the historical literature and use new microscopy methods to find answers to these questions. The resulting answers provide important knowledge that will assist other researchers and drive the field of 2D materials for solar energy conversion forward.

APPENDIX A

SUPPORTING INFORMATION FOR CHAPTER 2: SINGLE NANOFLAKE PHOTOELECTROCHEMISTRY REVEALS INTRA-NANOFLAKE DOPING HETEROGENEITY THAT EXPLAINS ENSEMBLE-LEVEL PHOTOELECTROCHEMICAL BEHAVIOR

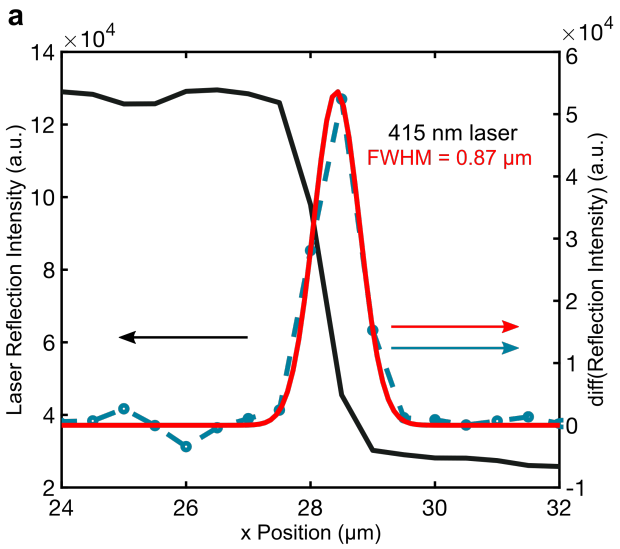

Figure S2.1. Knife-edge analysis of laser beam profiles. Laser reflection intensity of 415 nm laser as it was scanned over an opaque region of sample. (black line). The derivative of the black trace is shown in blue and a gaussian fit of the derivative is shown in red. The diameter of these laser beam was determined to be the full-width half-maximum (FWHM) of this gaussian fit.

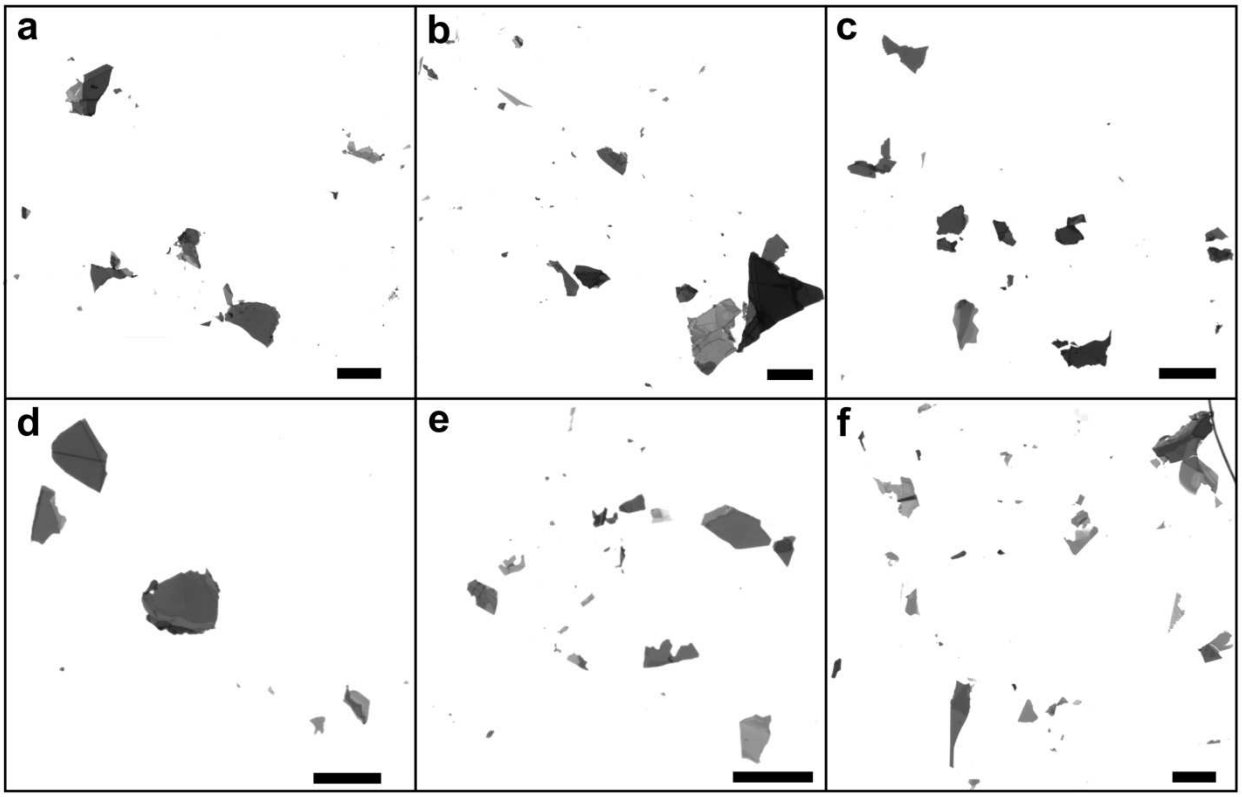

Figure S2.2. Optical microscope images of (a-c) SPI-MoS_2 and (d-f) Re-MoS_2 nanoflakes on ITO electrodes. All scale bars are 100 μm.

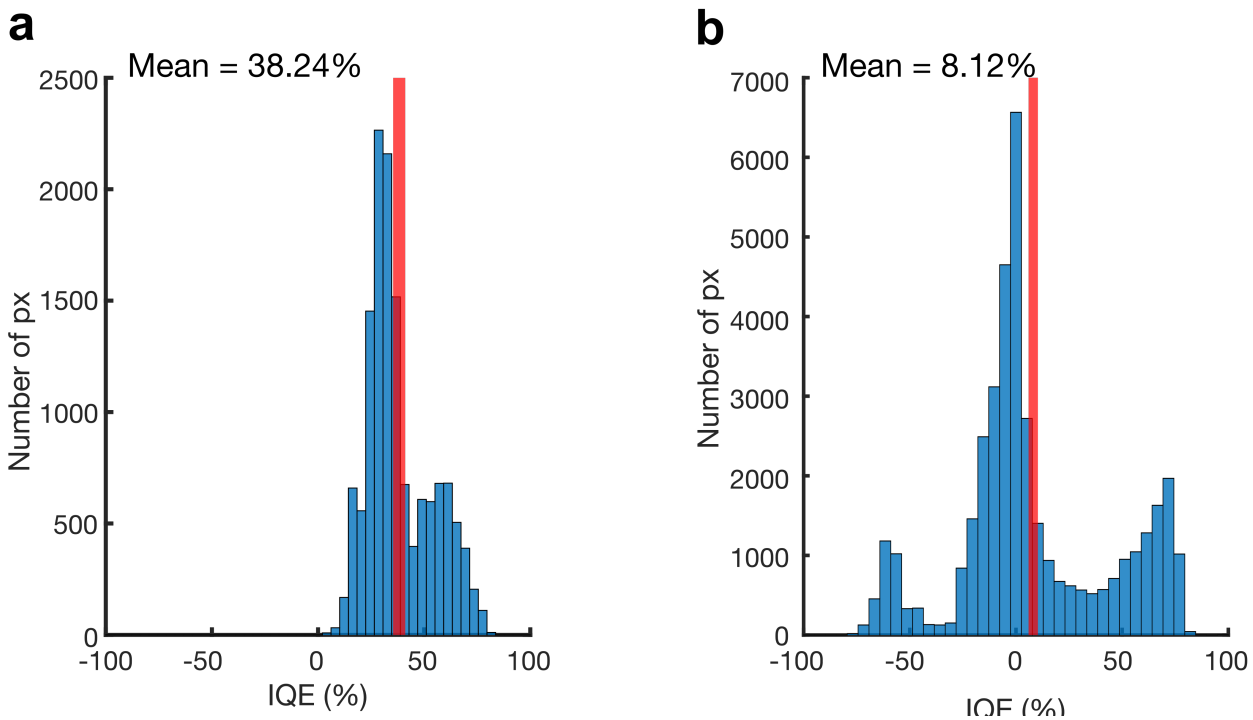

Figure S2.3. IQE distributed from (a) 21 Re-MoS_2 nanoflakes and (b) 52 SPI-MoS_2 nanoflakes. The red lines in both panels indicate the mean IQE value from the data shown.

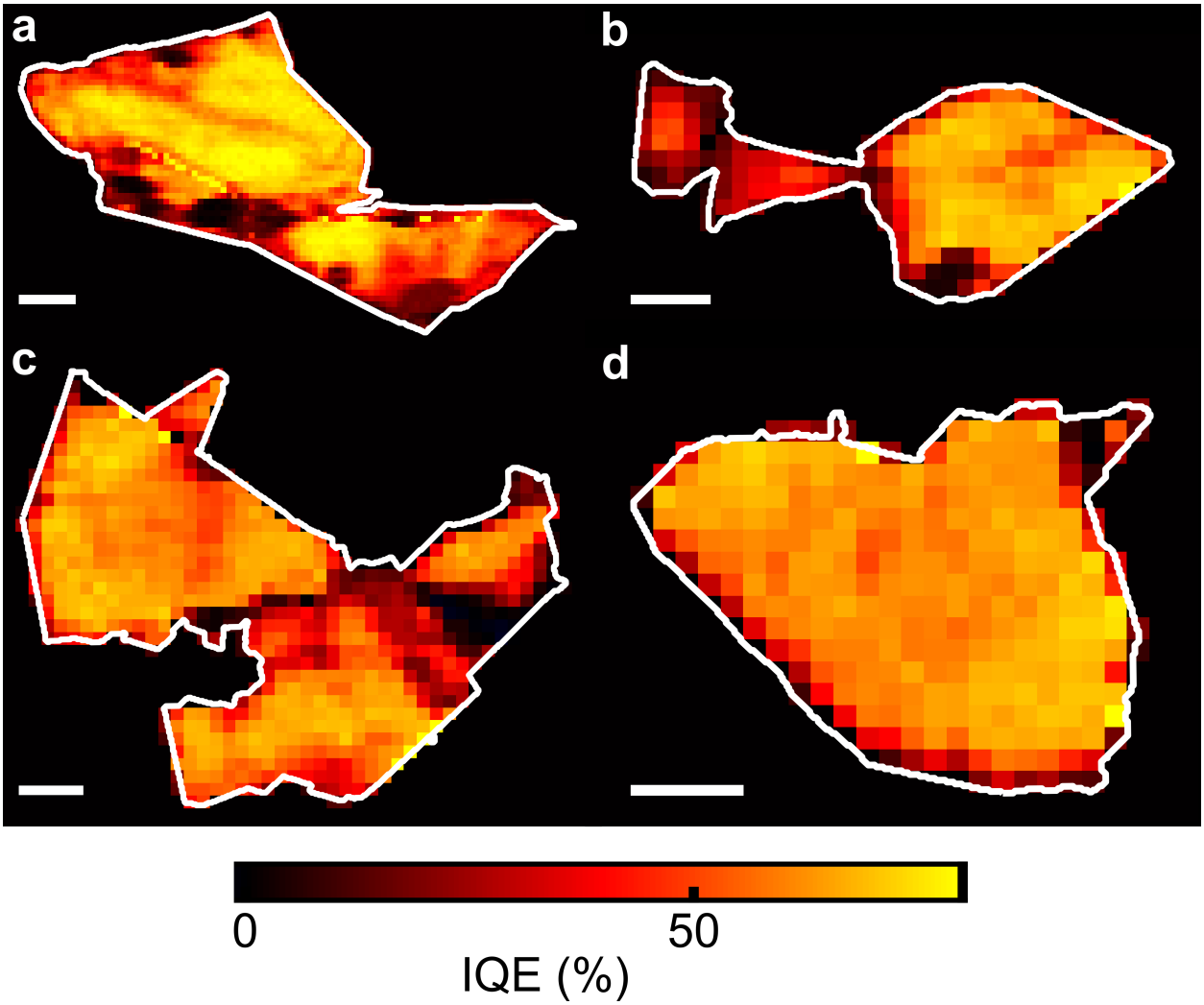

Figure S2.4: Additional IQE maps of n-type SPI-MoS2 nanoflakes. All scale bars are 10 μm.

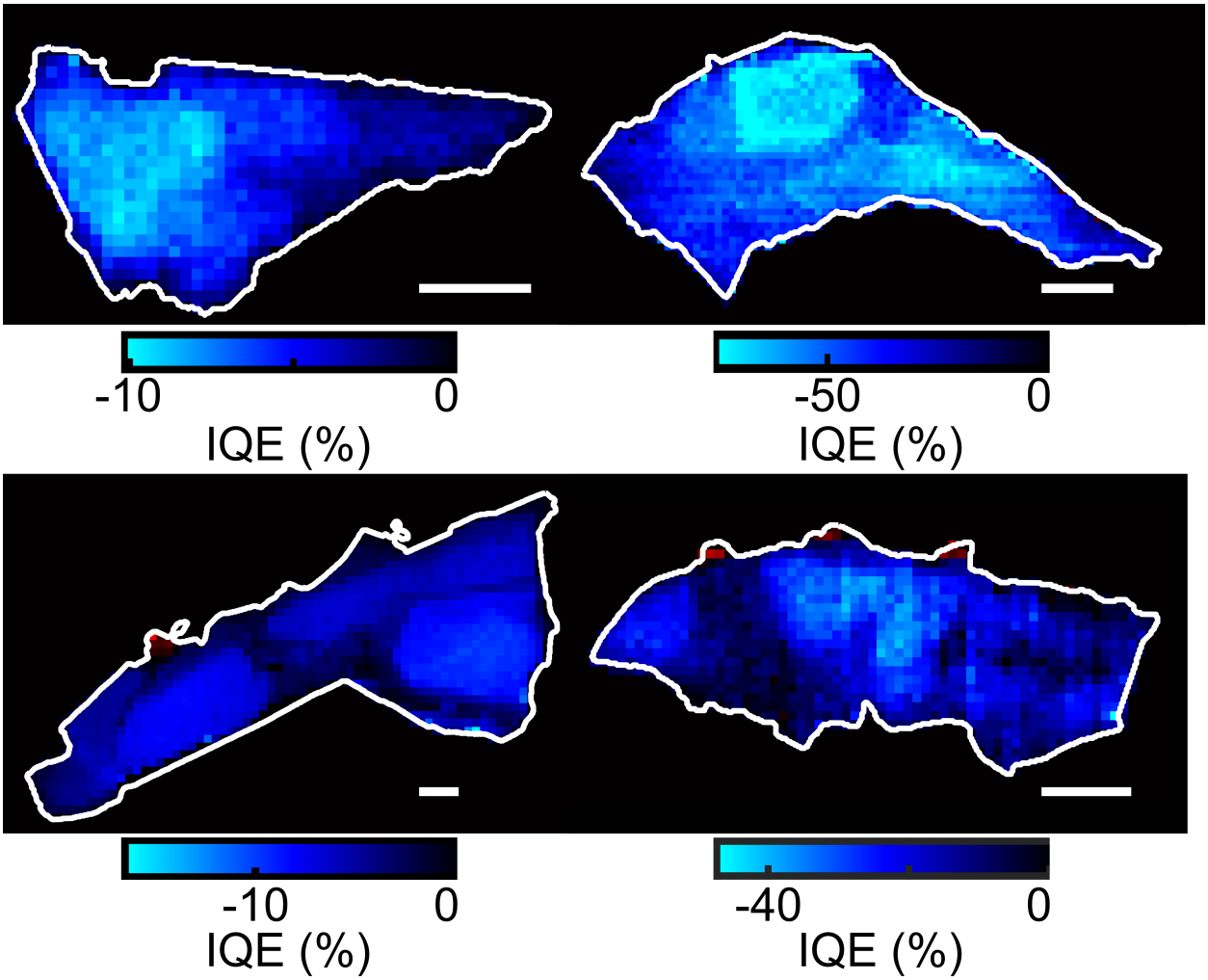

Figure S2.5: Additional IQE maps of p-type SPI-MoS2 nanoflakes. All scale bars are 10 μm.

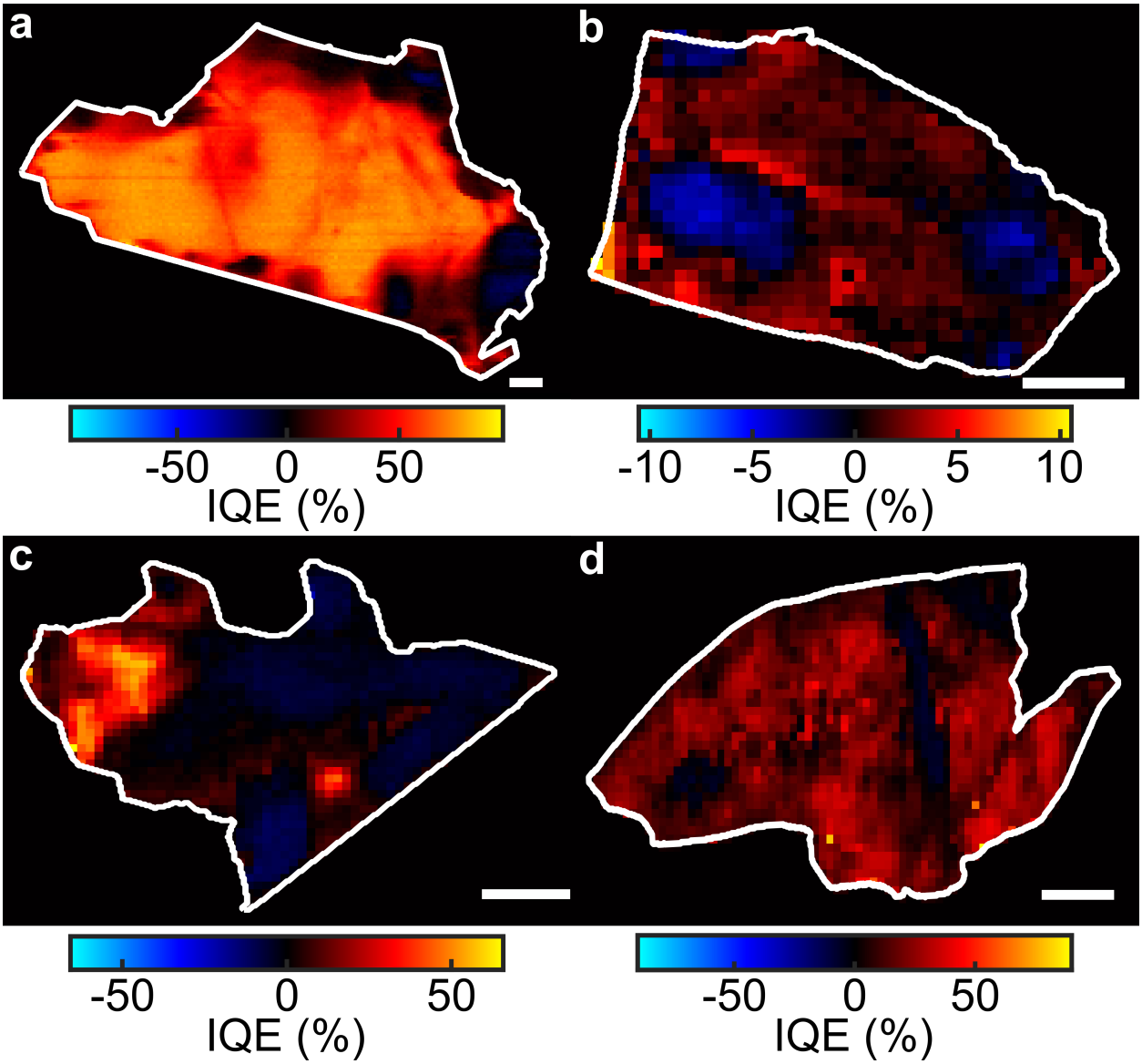

Figure S2.6. Additional IQE maps of SPI-MoS_2 nanoflakes exhibiting randomly distributed n- and p-type domains. All scale bars are 10 μm.

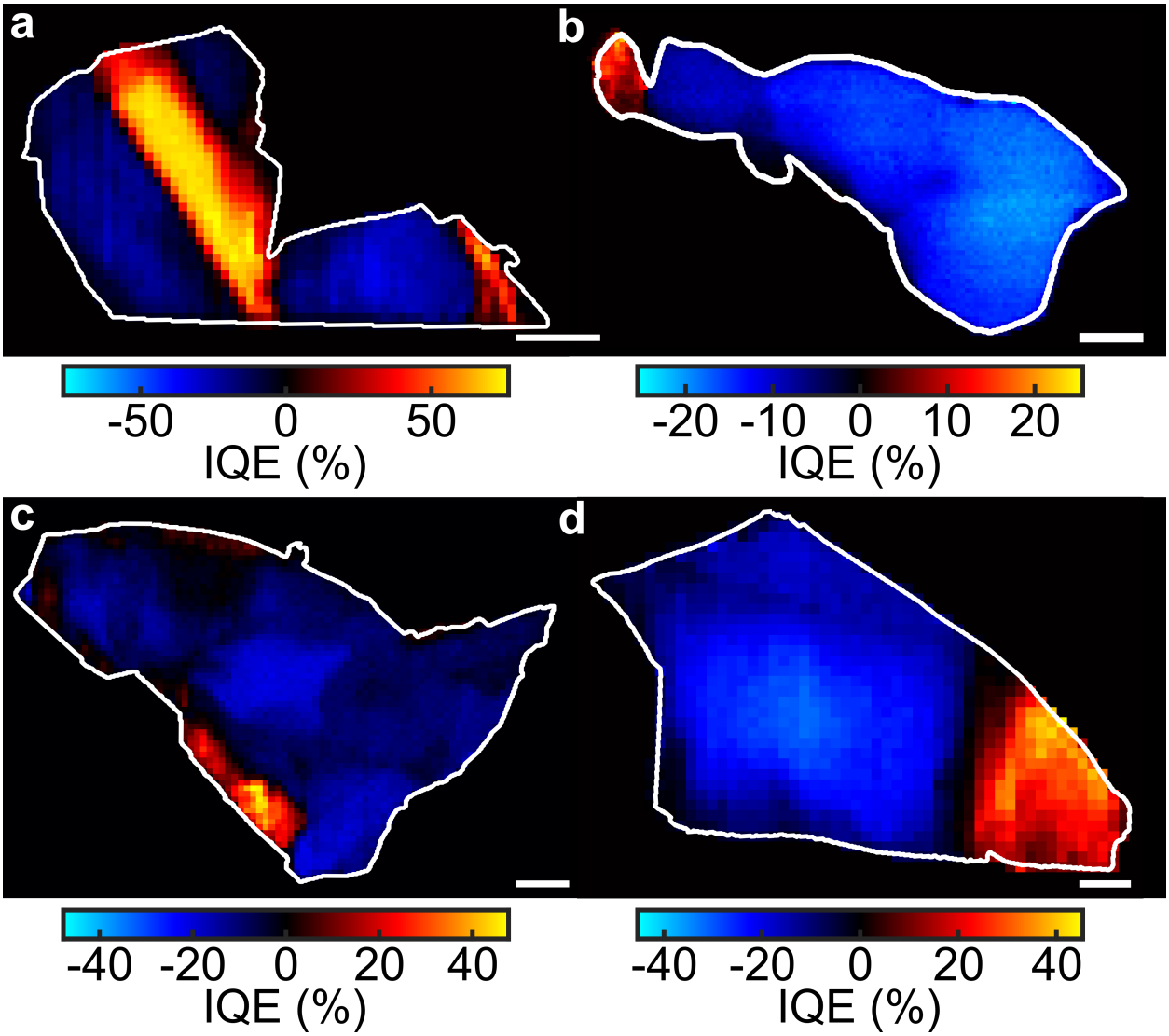

Figure S2.7: Additional IQE maps of SPI-MoS_2 nanoflakes with intraflake doping heterogeneity. All flakes exhibit sharp boundaries between n- and p-type domains. All scale bars are 10 μm.

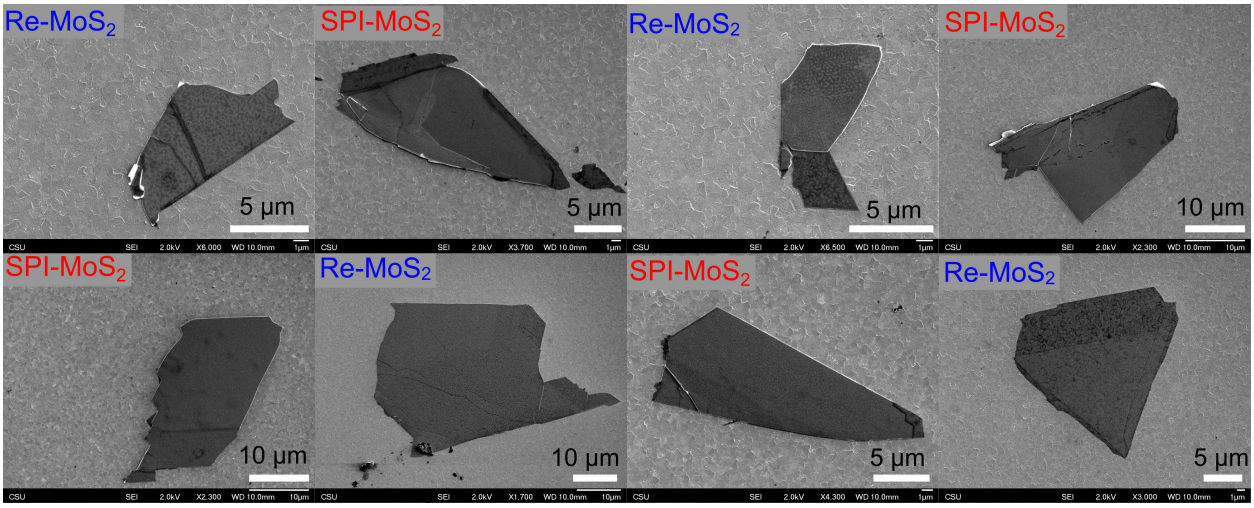

Figure S2.8. SEM images of Re-MoS_2 and SPI-MoS_2 nanoflakes.

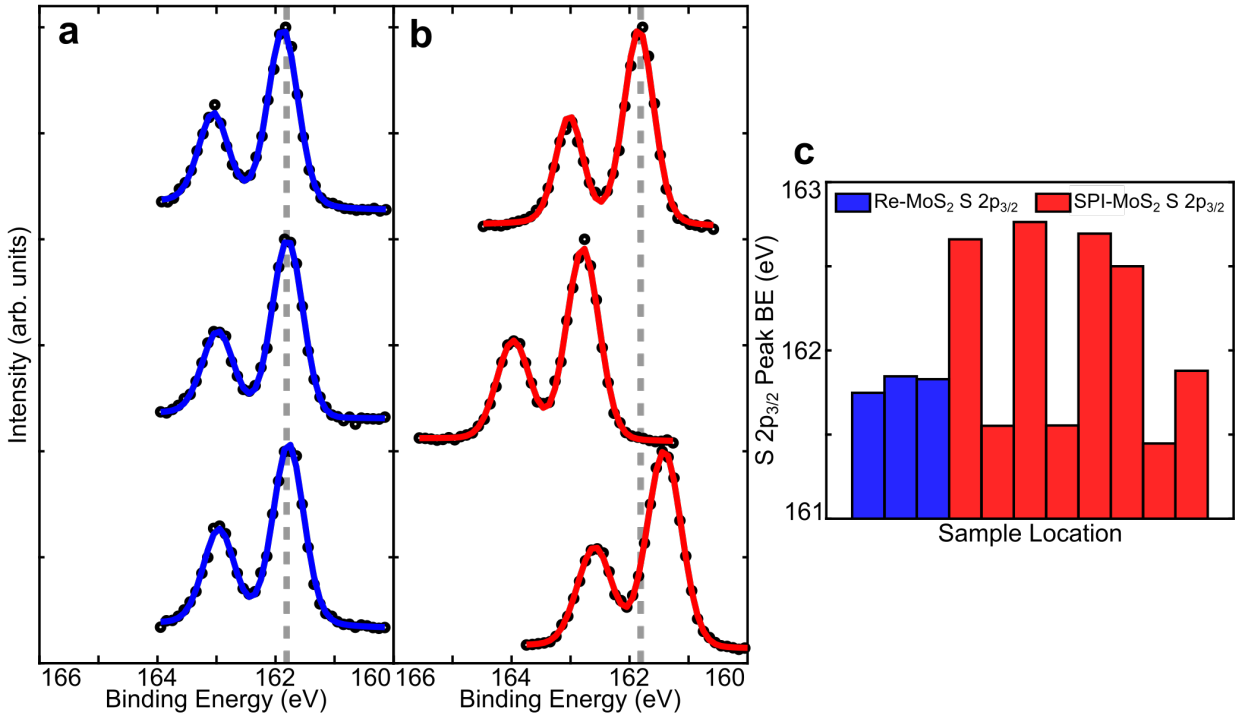

Figure S2.9. High resolution XPS data of the S 2p region. (a) S 2p XPS data from 3 locations on Re-MoS_2 as shown in Figure 2.5 in the main text. (b) Same as (a) but for SPI-MoS_2. (c) Peak binding energies of the S $2p_{3/2}$ peak as a function of sample location from both Re-MoS_2 and SPI-MoS_2.

Element	SPI-MoS_2 (mg/L)	Re-MoS_2 (mg/L)	Solvent (HNO_3) (mg/L)	Blank (mg/L)
Ag	0.03	0.01	0.14	2.62
Al	0.13	0.04	4.03	0.38
B	0.88	0.19	60.24	10.54
Ba	0.00	0.00	0.32	0.00
Cd	0.00	0.00	0.00	0.31
Cr	0.00	0.00	0.05	0.00
Cu	0.01	0.00	0.26	0.08
Fe	2.41	8.94	121.51	0.00
K	0.07	0.01	0.08	-8.62
Li	0.00	0.00	0.03	0.00
Mn	0.00	0.00	0.08	0.00
Mo	1.00	1.00	1.00	1.00
Na	1.15	0.20	42.50	0.00
Ni	0.00	0.00	0.00	0.54
S	0.47	0.56	0.36	0.00
Sb	0.00	0.00	0.49	0.38
Se	0.02	0.00	0.39	6.62
Si	1.02	0.50	34.51	0.00
Zn	0.00	0.00	0.05	0.00

Table S2.1. Elemental analysis results for SPI-MoS_2, Re-MoS_2, nitric acid solvent blank, and a blank sample. The concentrations are normalized to the Mo content in each sample.

Supplementary Note 2.1: Calculating IQE values from EQE maps.

General correlated photocurrent and laser reflection experimental procedure: A Horiba iH550 spectrometer measures the reflected laser light intensity from the sample at the same time as the potentiostat measures the photocurrent; reflected laser light intensity increases on MoS_2 regions of the sample. Hence, we measure the photocurrent and laser reflection maps of single nanoflakes at the same time. The data and image processing routines were executed in MATLAB.

Background subtraction routine in photocurrent mapping experiments. Direct current (DC) photocurrent maps (Figure S2.10c) were background subtracted according to the procedure detailed below. First, we thresholded the laser reflection map in Figure S2.10a to distinguish ITO and MoS_2 pixels. We define ITO pixels as those pixels that are located more than four pixels away from the MoS_2 flake contour (see pink and blue vertical lines in Figure S2.10b). The photocurrent from the illuminated MoS_2 pixels represents the signal at that location minus the average of the ITO pixels of the same row, yielding the background subtracted map in Figure S2.10c.

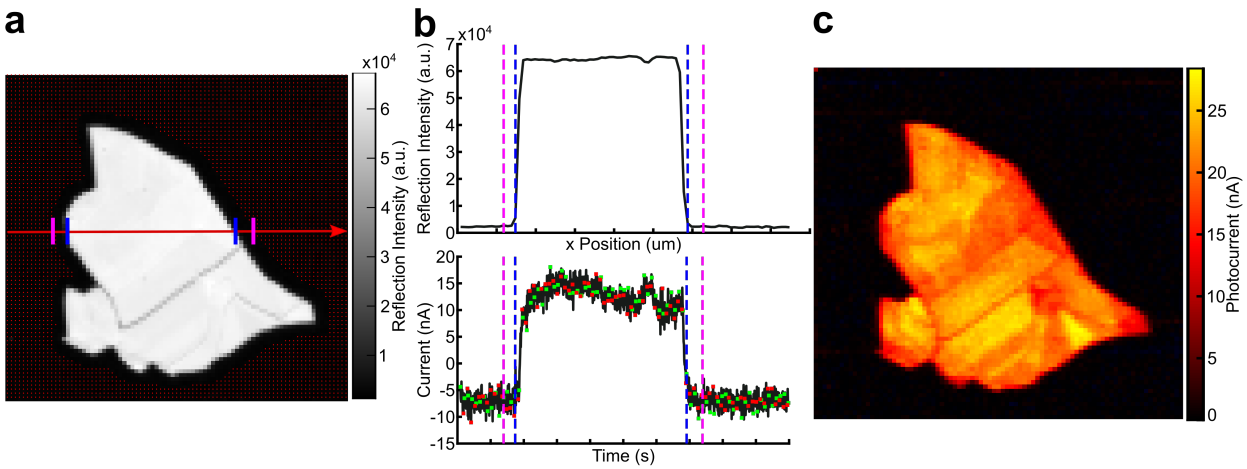

Figure S2.10. Background subtraction routine for photocurrent maps. (a) Laser reflection map of a Re-MoS_2 nanoflake. The red dots represent background pixels. The red arrow indicates the line profile data in panel (b). The blue and pink lines indicate the edge of the nanoflake and the four-pixel distance from the flake edge to the first background pixel, respectively. (b) Top: Laser reflection line profile from the red arrow in (a). Blue and pink lines are the same as (a). Bottom: Raw current data during the mapping experiment from the cross section indicated by the red arrow in (a). Green and red markers indicate microscope stage start and stop points that define the data in each pixel. Current values in each pixel were assigned as the average of the current data between a single pair of green and red markers. Background current values were determined from the region to the left of the pink line. (c) Photocurrent map after background subtraction.

Calculating EQE and IQE maps. We calculate the EQE values according to

$$EQE = \frac{i_{pc}}{qI_0} \tag{S2.1}$$

where i_{pc} represents the background subtracted current (i.e., the photocurrent described above in unites of amperes), q is the elementary charge (C), and I_0 is the incident photon flux (s^{-1}).

Having calculated the EQE maps, IQE maps were calculated using the EQE maps, monochromatic transmission images, and laser reflection maps according to

$$IQE = \frac{EQE}{1-T(\lambda)-R(\lambda)} \quad (S2.2)$$

where $T(\lambda)$ and $R(\lambda)$ are the transmittance and reflectance values at wavelength λ, respectively.

$T(\lambda)$ values were obtained from widefield monochromatic transmission images using monochromatic illumination from a Horiba OBB Tunable PowerArc Illuminator equipped with a 150 W tungsten-halogen lamp. The transmittance value for each pixel in the image was calculated from the ratio between the nanoflake pixel intensity and the background (i.e., ITO substrate) pixel intensity (see Eq. S2.3).

$$T(\lambda) = \frac{Int._{flake}}{Int._{bkg}} \quad (S2.3)$$

Since the pixel size of the widefield transmission image differs from the reflection and EQE images, we compute the transformation matrix that transforms the transmittance image onto the reflection and EQE images to obtain correlated $T(\lambda)$ and $R(\lambda)$ values and, ultimately, the spatially resolved IQE image. The transformation matrix was calculated by selecting identical points in both the transmittance images and laser reflection map using the *ginput* function in MATLAB (see red dots in Figure S2.11b and c, corresponding to the widefield transmittance and scanning reflection maps, respectively). Then, the *imwarp* function transforms the transmittance image onto the reflection image using the transformation matrix.

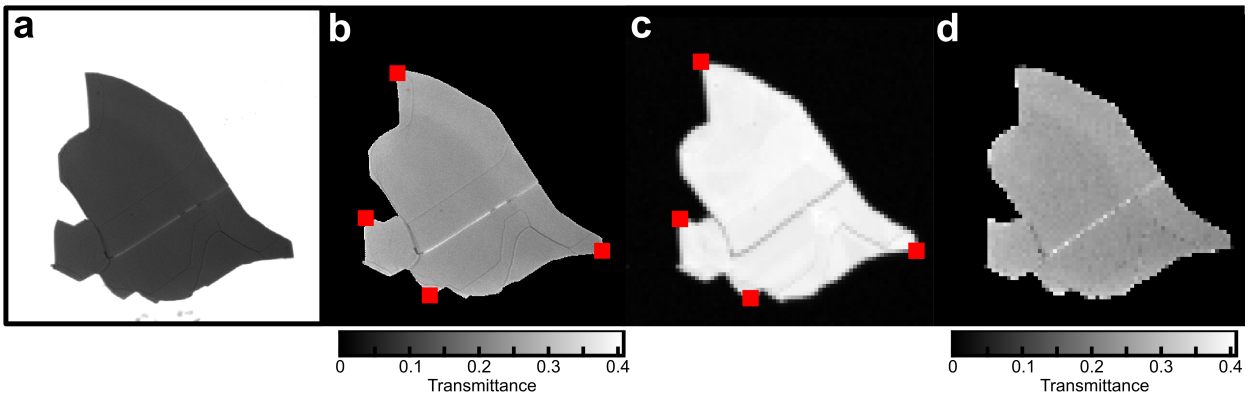

Figure S2.11. Calculating the transformation matrix for image overlay. (a) Monochromatic transmission image (415 nm) of a single Re-MoS_2 nanoflake. (b) Transmittance image calculated according to Eq. S3. Red squares represent the points used to calculate the transformation matrix. (c) Laser reflection image. Red squares represent the same locations as (b). (d) Transmittance image after applying the transformation matrix.

R(λ) values were calculated in a pixel-by-pixel fashion using the reflected laser light intensity maps in Figure S2.10a. According to literature, the reflectance value for bulk MoS_2 ($R_{MoS2,bulk}$) at 415 nm, corresponding to the laser illumination wavelength in photocurrent mapping experiments, is 0.30.[S1] According to the Delta Technologies manufacturer, the reflectance value of the ITO substrate (R_{ITO}) at 415 nm is 0.09.[S2] The ratio of the reflected 415 nm light intensity from thick, bulk-like MoS_2 nanoflakes to the ITO substrate should be 0.30/.09 = 3.33. However, we measured the intensity of reflected 415 nm laser light from 10 bulk-like MoS_2 nanoflakes ($I(415\text{ nm})_{MoS2,bulk\text{-}NF}$) was ~10,000 counts and the reflected 415 nm laser light from the ITO substrate ($I(415\text{ nm})_{ITO}$) was ~200 counts, yielding a reflected laser intensity ratio of 50. We attribute the large intensity ratio difference to multiple laser reflection paths in our experimental setup. To account for this effect, we calculated a response factor (*RF*) according to

$$RF = \frac{\left(I(\lambda)_{\mathrm{MoS_2,bulk-NF}} \Big/ R(\lambda)_{\mathrm{MoS_2,bulk}}\right)}{\left(I(\lambda)_{\mathrm{ITO}} \Big/ R(\lambda)_{ITO}\right)} \quad \text{(S4)}$$

The reflected 415 nm laser intensity from any nanoflake ($I(415\text{ nm})_{\text{MoS2-NF}}$) can be used to calculate the reflectance value $R(415\text{ nm})_{\text{MoS2-NF}}$ using

$$R(415\text{ nm})_{\text{MoS2-NF}} = \frac{I(\lambda)_{\text{MoS}_{2-\text{NF}}}}{\text{RF}\left(I(\lambda)_{\text{ITO}} / R(\lambda)_{ITO}\right)} \quad \text{(S2.5)}$$

Figure S2.12 shows the reflectance value map, where the thickest nanoflake regions have bulk values.

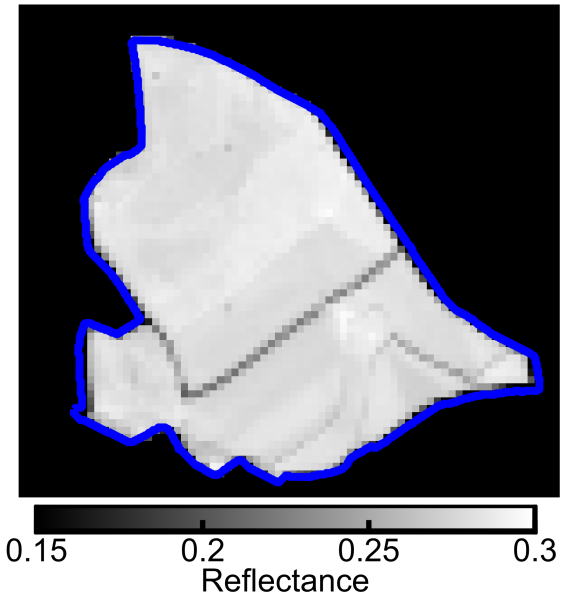

Figure S2.12. Reflectance map of a single Re-MoS_2 nanoflake.

Supplementary Note 2.2: Calculating nanoflake thickness

Nanoflake thickness (d) was calculated according to

$$d = \frac{1}{\alpha(\lambda)} ln\left[\frac{(1-R(\lambda)^2}{T(\lambda)}\right] \quad \text{(S2.6)}$$

where $\alpha(\lambda)$ is the absorption coefficient of bulk MoS_2 ($\alpha(636\text{ nm}) = 3 \times 10^5\text{ cm}^{-1}$).[S3-4]

References

(S2.1) Bichsel, R.; Levy, F. Influence of Process Conditions on the Electrical and Optical Properties of RF Magnetron Sputtered MoS2 films. *J. Phys. D: Appl. Phys.* **1986**, *19* (9), 1809–1819.

(S2.2) Delta Technologies, Limited. *General Bibliography*. http://www.delta-technologies.com/downloads/bibliography.pdf?C=3 (accessed 2020-11-15)

(S2.3) Frindt, R. F.; Yoffe, A. D.; Bowden, F. P. Physical Properties of Layer Structures : Optical Properties and Photoconductivity of Thin Crystals of Molybdenum Disulphide. *Proc. R. Soc. A.* **1963**, *273* (1352), 69–83.

(S2.4) Hassanien, A. S.; Akl, A. A. Influence of Composition on Optical and Dispersion Parameters of Thermally Evaporated Non-Crystalline Cd50S50−xSex Thin Films. *J. Alloys Compd.* **2015**, *648*, 280–290.

APPENDIX B

SUPPORTING INFORMATION FOR CHAPTER 3: MOLECULAR REACTION IMAGING OF A SURFACE RECOMBINATION PROCESS EXPLAINS PERFORMANCE VARIATION AMONG SMOOTH MOS_2 PHOTOELECTRODES

Supplementary Note 3.1: Additional image and photoelectrochemical data.

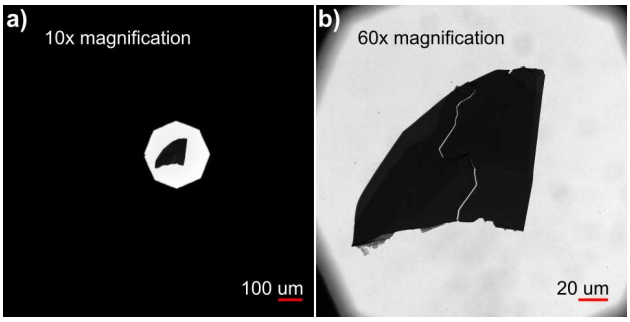

Figure S3.1: Illumination mode for whole-nanoflake photoelectrochemical measurements. (a) 10× magnification transmission image of a nanoflake with the light illumination spot limited by the Field Iris Diaphragm of the microscope. (b) 60× magnification transmission image of the same nanoflake from (a). The edges of the Field Iris Diaphragm can be seen near the corners of the image.

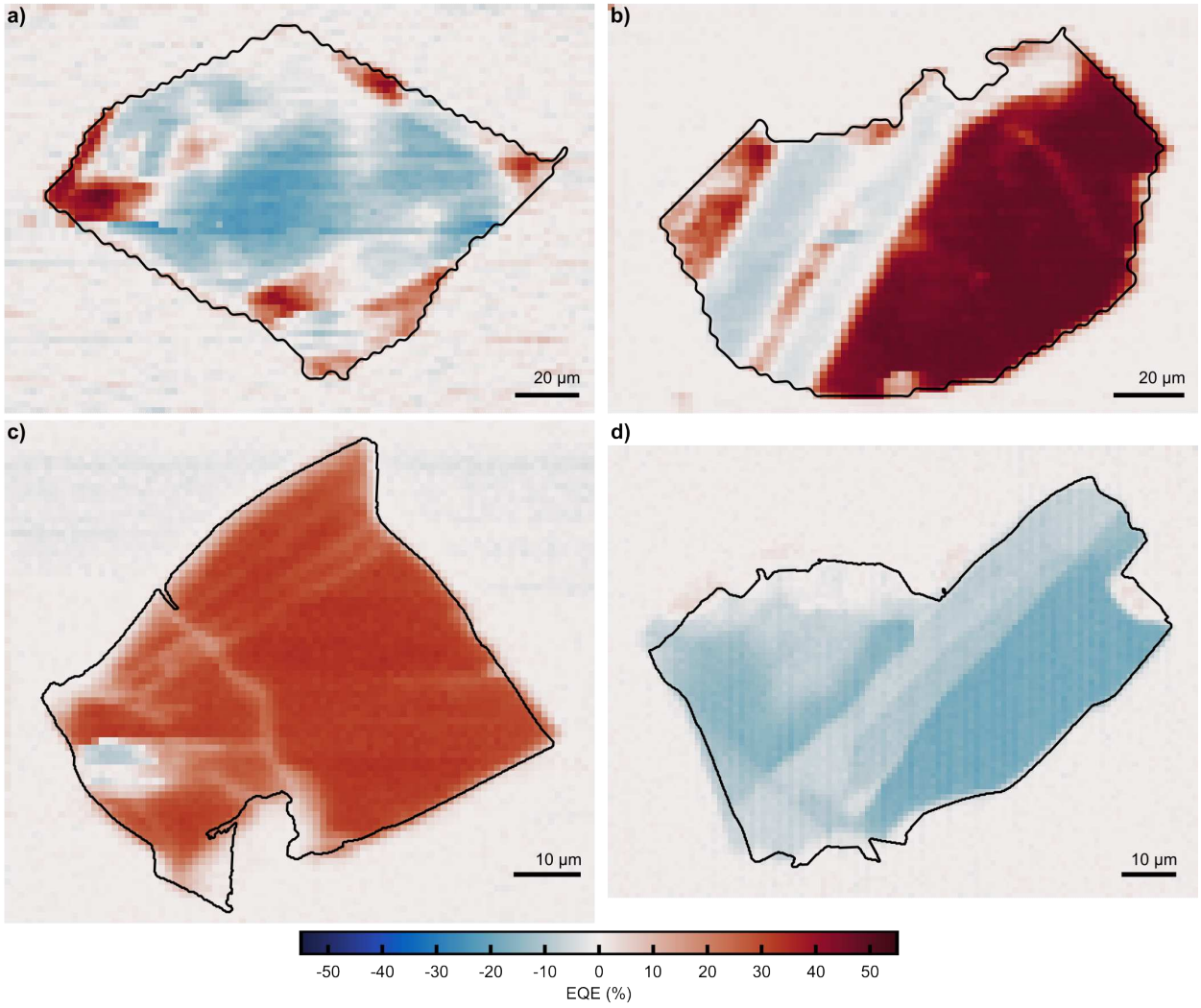

Figure S3.2: EQE maps of MoS_2 nanoflakes exfoliated from naturally occurring bulk crystals obtained from SPI manufacturer.

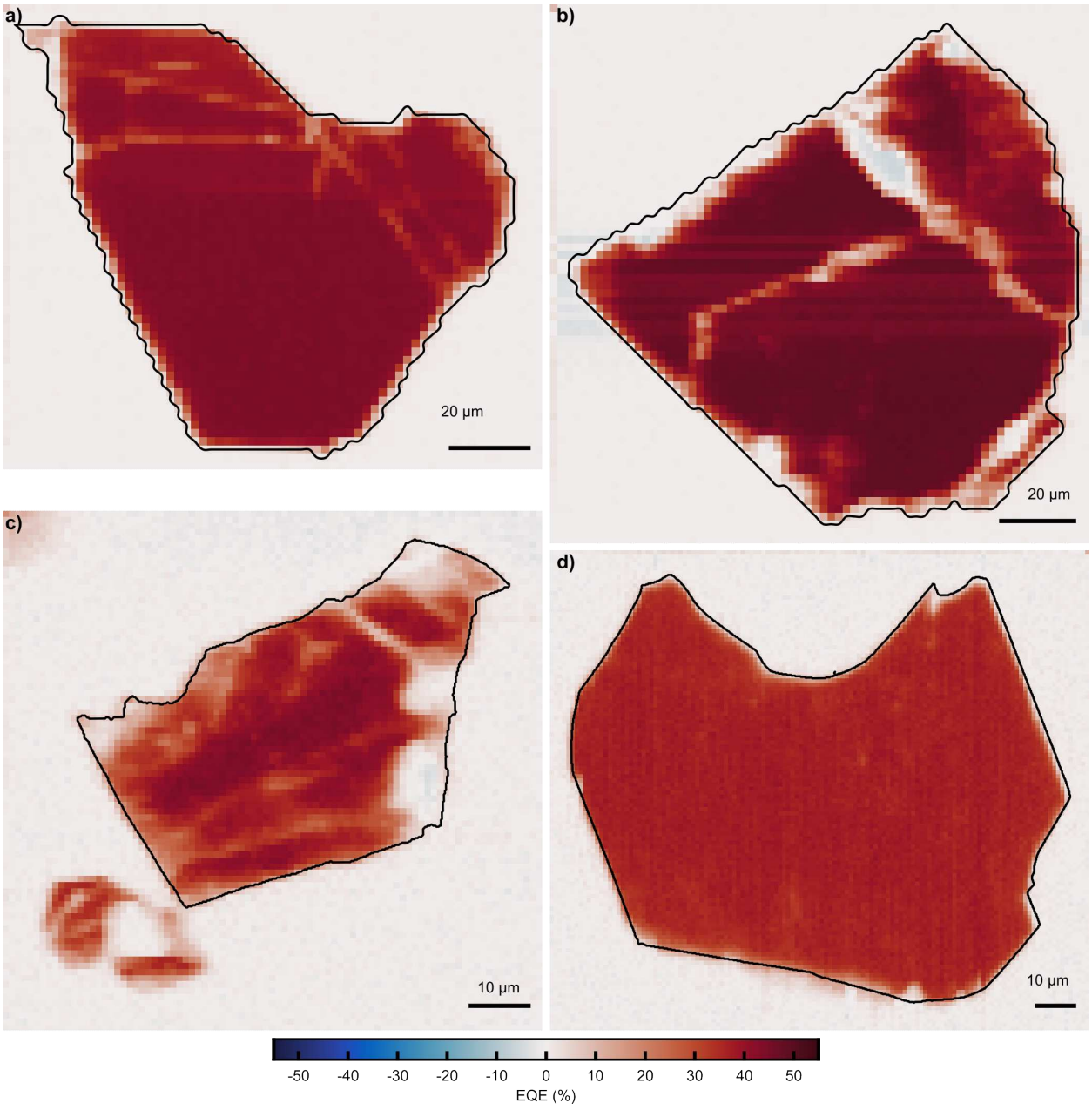

Figure S3.3: Additional EQE maps of MoS_2 nanoflakes exfoliated from a bulk synthetic Re-doped MoS_2 crystal from 2D Semiconductor manufacturer.

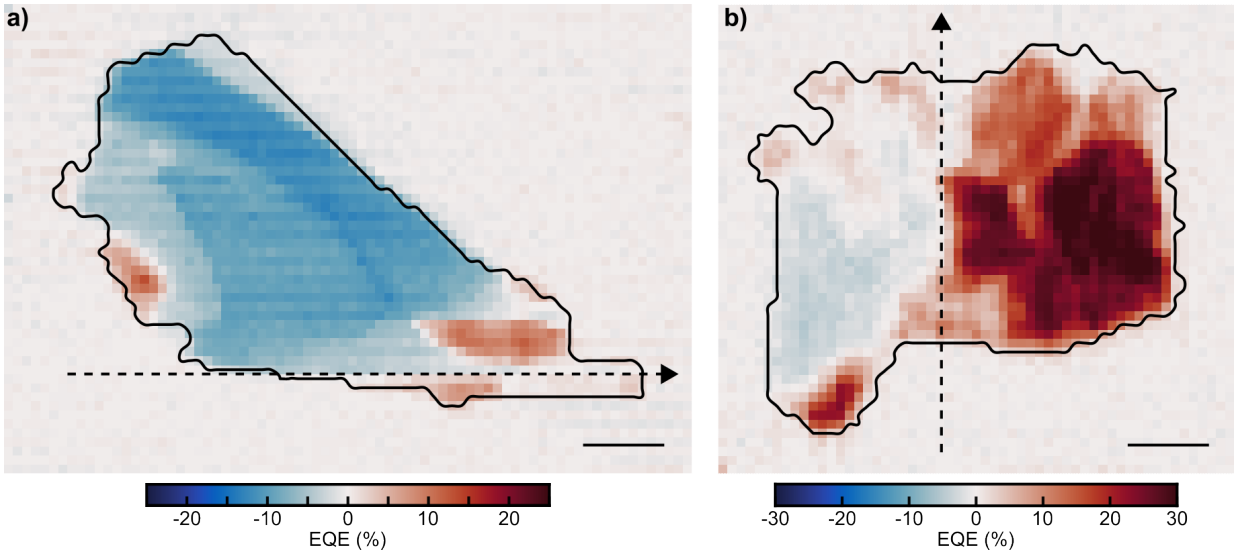

Figure S3.4: EQE maps of nanoflakes. (a) EQE map of the nanoflake from **Error! Reference s ource not found.**b. (b) EQE map of the nanoflake from **Error! Reference source not found.**c. The laser scan direction is indicated for both flakes by the black, dashed arrow. Scale bars are 10 μm.

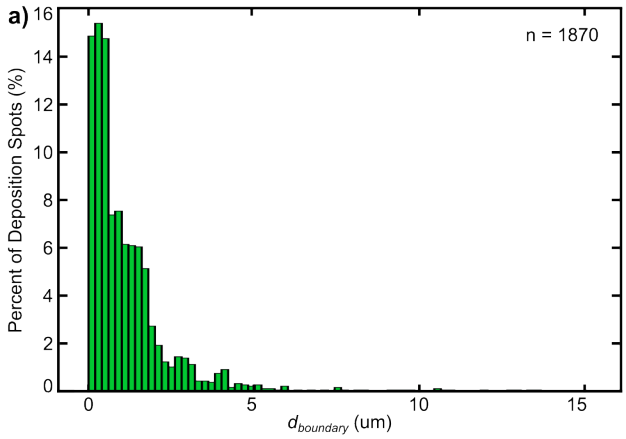

Figure S3.5: Histogram of $d_{boundary}$ values from all iodine deposition spots from all nanoflakes.

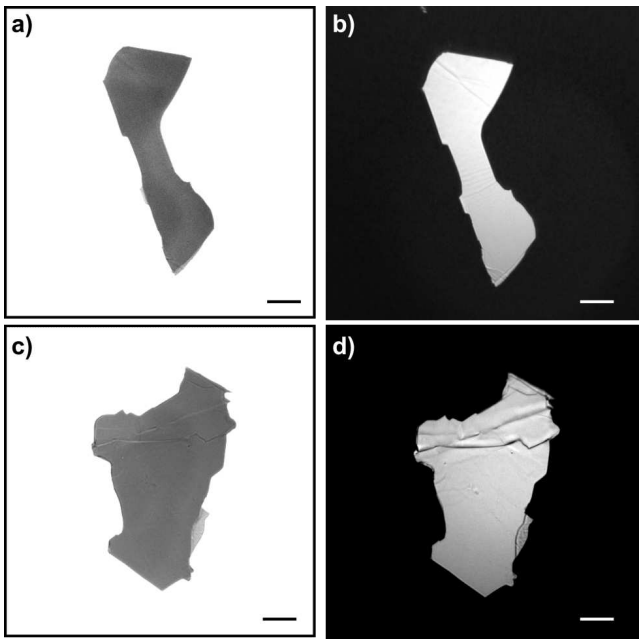

Figure S3.6: (a,c) Transmission images of MoS_2 nanoflakes. (b,d) Reflection images of MoS_2 nanoflakes that reveal fine surface structure unseen in (a,c). Scale bars are 10 μm.

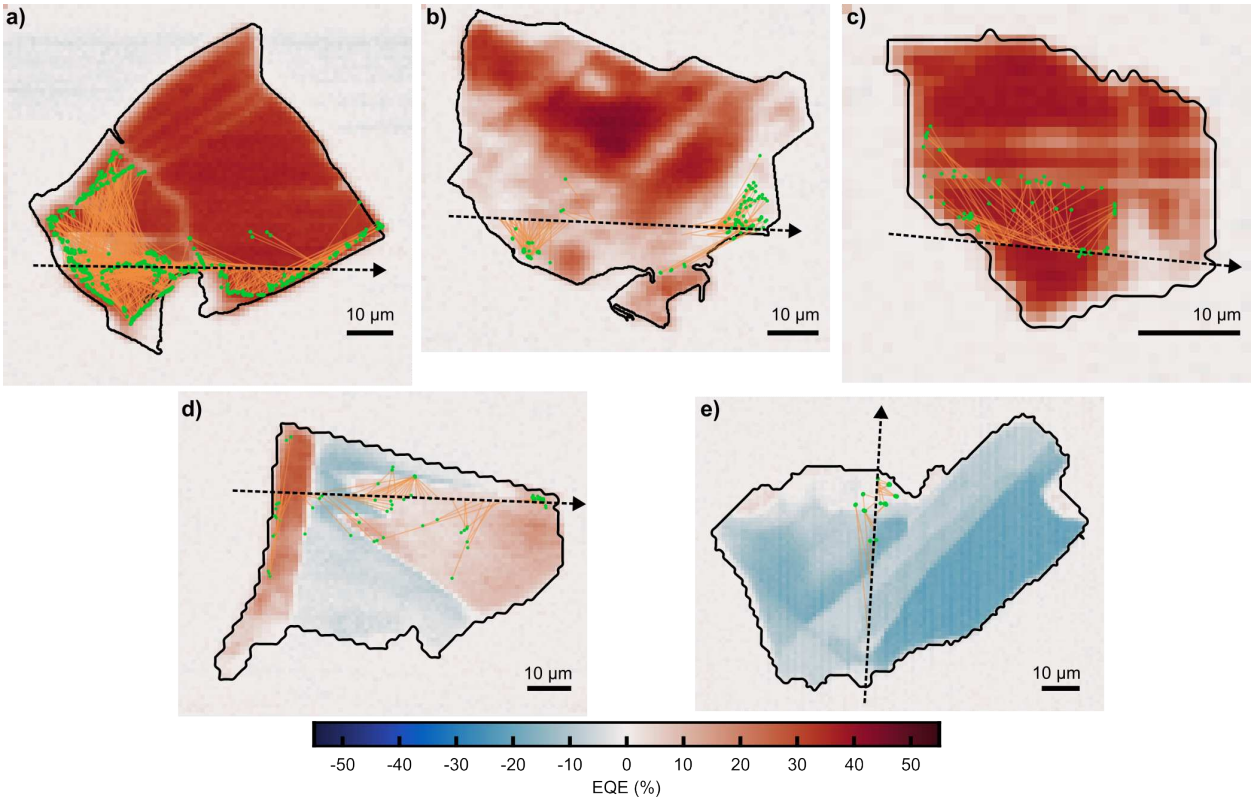

Figure S3.7: Iodine Deposition spots overlaid on EQE maps. (a-e) EQE maps of MoS_2 nanoflakes with iodine deposition spots overlaid in green. The orange lines represent the $d_{transport}$ vector and the black dashed arrow represents the laser line scan.

Supplementary Note 3.2: Image Analysis Procedures for Molecular Reaction Imaging

In a typical molecular reaction imaging experiment, the microscope stage was rastered in 1 µm steps every 8 seconds as a focused 415 nm laser excited the sample for a period of 5 seconds at each stage position. At the same time, the MoS_2-coated ITO electrode was imaged on an EM-CCD camera and the current was monitored via a potentiostat. The image data was analyzed with homewritten MATLAB code as described below.

3.2.1 Locate and quantify the laser illumination spot and size at the electrode surface.

The first step of the image analysis was to determine the position of the focused laser. To do so, we acquire a transmission image of the sample under focused laser spot illumination only. Figure S3.8a shows a transmission image of the sample, where the focused laser spot appears as bright white pixels and the background appears dark because the white light illuminator remains off. To

determine the center position of the laser spot as well as the beam diameter (defined as the full width at half maximum), we fit the image data in Figure S3.8b with a 2D Gaussian function, yielding the center position (red dot in Figure S3.8a and FWHM = 0.87 μm).

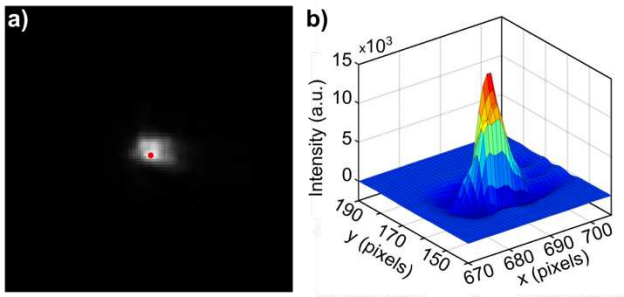

Figure S3.8: Laser spot determination for molecular reaction imaging experiments. (a) Transmission image of the 415 nm laser spot. The red dot represents the center position of the Gaussian beam. (b) 3–dimensional projection of the laser spot from (a).

3.2.2 Segment images during a single step in the line scan experiment.

Following step 3.2.1, the molecular reaction imaging line scan experiment commenced. Here we discuss how image data at each position of the line scan experiment is segmented. Our home-built photocurrent mapping system syncs image and electrochemical data with the focused laser spot position (i.e., stage position) using a data acquisition (DAQ) card. Figure S3.9 shows three different analog data signals acquired by the DAQ card for a single "step" in the molecular reaction imaging experiment. The top trace is the stage movement signal (or a TTL trigger signal from the automated stage). This signal is 0 V (or off) when the stage is moving and 1 V when the stage is not moving. Figure S3.9-top shows the stage arrives at a position at t = 0 s, remains fixed for 8 s, then moves at t = 8 s to the next stage position. During this time, the laser shutter (as monitored by another TTL trigger signal in Figure S3.9-middle) remains off for the first 1 s, opens at t = 1 s, and then closes at t = 6 s. This "closed-open-closed" laser shutter sequence allowed us to acquire control images of the sample before the laser illuminated the sample, inducing iodine formation,

as well as after the sample returned to a dark equilibrium state after illumination. Since the camera continuously acquires images during the entire experiment (Figure S3.9-bottom), we segmented and assigned images during the "close" and "open" portions of the experiment and rejected any images acquired within 0.25s of the stage moving to ensure this movement did not induce blurring in the images.

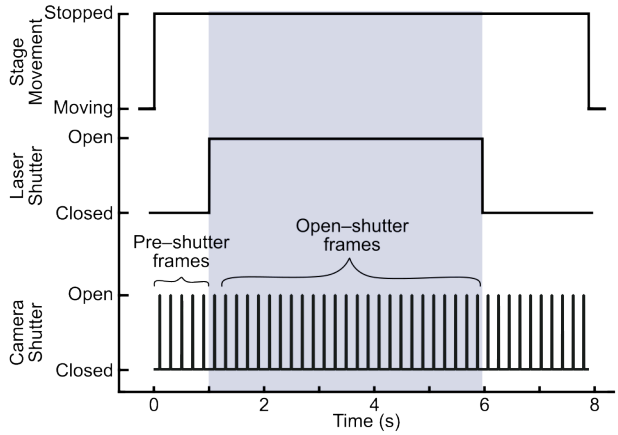

Figure S3.9: Data acquisition signals for a signal step during a molecular reaction imaging line scan experiment. (top) stage movement TTL trigger signal. (middle) laser shutter TTL trigger signal. (bottom) cMOS trigger signal. Each step of the line scan experiment is 8s, indicated by a "stopped" stage for 8 s. The blue shaded region indicates the laser "on" time from 1s to 5s.

3.2.3 Acquire a control image before the line scan experiment and reference all other images in the experiment to the control image using a transformation matrix.

Before the line scan experiment begins, we acquire a single "control" transmission image (Figure S3.10a) of the nanoflake that serves as a reference point for all other images in the experiment. As the experiment proceeds, we reference all other images to the control image using a transformation matrix (as described in the SI of Ref. S3.1). Briefly, we identify "reference points" using the *regionprops* function in MATLAB (schematically shown as red squares in Figure S3.10) in the control image and any other image in the movie (for example, image n in Figure S3.10b). We compute the transformation matrix from the same reference points in the two different images (i.e., the control image and any other image n) using the *fitgeotrans* function in MATLAB. Then,

we transform all pixel coordinates (including the iodine deposition spot information, as discussed below) using the *transformPointsForward* function in MATLAB. Importantly, this procedure allowed us to quantitatively overlay the iodine deposition locations onto the single control image.

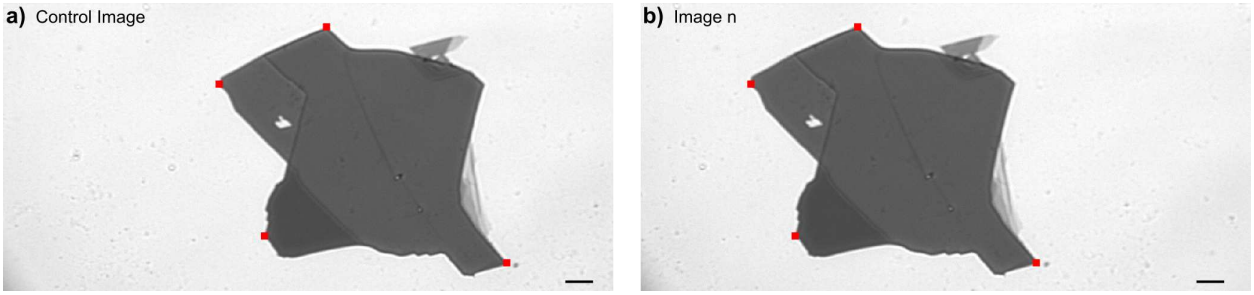

Figure S3.10: Transmission images of a nanoflake (a) before the line scan experiment, which serves as the "control image". The red squares indicate the reference points used to generate the transformation matrix. (b) Representative image of the same nanoflake near the middle of a line scan experiment. The red squares mark the same points on the flake as in (a).

3.2.4 Image thresholding procedure to identify iodine deposition spots.

Here we qualitatively describe the image subtraction procedure to identify iodine deposition locations in transmission images. The first step of the algorithm generates a single "control" image of the nanoflake in a "dark" equilibrium state before the laser shutter opens. To do so, we averaged all frames before the laser shutter opens (see Figure S3.9). Figure S3.11a shows this dark equilibrium state image for a representative nanoflake. The next section describes how we analyze the pixel intensity values of the "control" image to identify iodine deposition spots. Here we note that subtracting the average control image (i.e., Figure S3.11a) from all individual images before the laser shutter opens (e.g., Figure S3.11b), yields a featureless "blank" image (Figure S3.11c). On the other hand, if we subtract the average image in Figure S3.11a from individual frames when the laser illuminates the nanoflake while iodine deposition occurs (Figure S3.11d), then we effectively remove the contrast from the nanoflake alone and observe clear dark pixels in the

transmission image due to iodine formation (Figure S3.11e). The following section describes how we locate those iodine pixels using a thresholding procedure.

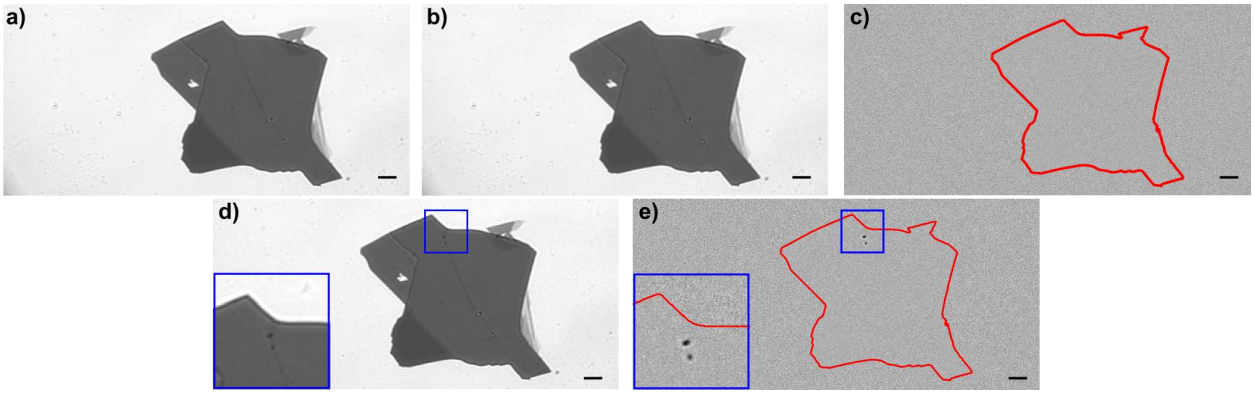

Figure S3.11. Image analysis algorithm to identify iodine deposition spots. (a) Average transmission image from all individual images acquired before the laser shutter opens. (b) A single image acquired before the laser shutter opens. (c) Average "blank" image, which represents the average image (a) subtracted from all individual frames before the shutter opens. The red line represents the nanoflake contour in (a). (d) Transmission image acquired during the laser "on" period. The inset shows a zoomed in section of the region of the nanoflake indicated by the blue box. The iodine deposition spots appear as dark contrast region in the center of the inset. (e) Iodine deposition spots appear after subtracting (a) from (d). The inset shows the same region as (d).

To identify any possible iodine deposition "events" under photoelectrochemical reaction conditions, we compared the pixel intensity distribution of the control "laser off" frames in Figure S3.11c to the "laser on" frames in Figure S3.11e. Figure S3.12a compares the distribution of pixel intensities from "laser off" and "laser on" images. Both populations resemble a normal distribution with a large peak centered at 0 intensity due to the background subtraction procedure. Next, we defined an iodine deposition threshold by fitting the "laser off" distribution with a Gaussian function and quantifying the threshold value as the center position of the gaussian minus 3-times the standard deviation (i.e., $x_0 - 3s$). Figure S3.12b shows a zoomed-in view of the histograms in Figure S3.12a near the iodine threshold value. Any pixels whose intensity values were less than the threshold value (meaning "darker contrast") were identified as iodine deposition pixels.

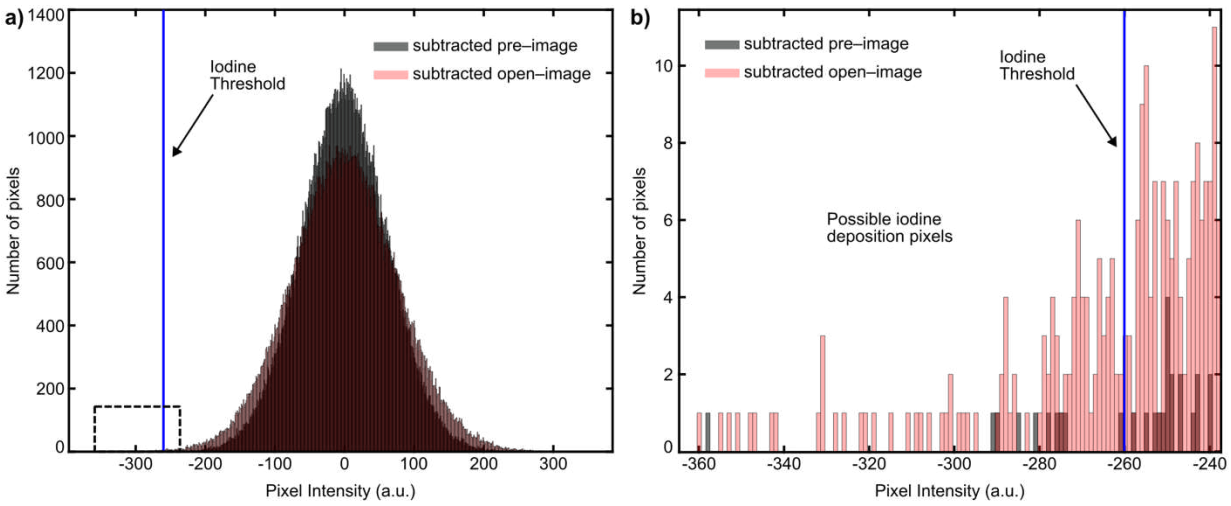

Figure S3.12: Quantitative analysis of pixel intensity distributions from laser "off" and "on" image data. (a) Histograms of all nanoflake pixels from laser "off" and "on" images, see SI text above for details. The blue vertical line indicates the numerical value defined as the iodine deposition threshold, see SI text for details. (b) Zoomed in section of (a) from the region indicated by the black dashed box.

Having identified all possible iodine deposition locations (i.e., pixels), we created binary images where each possible deposition spot was assigned a pixel value of 1 and all other pixels were assigned 0 values. Figure S3.13a shows a representative binary image including all possible iodine deposition spots (i.e., pixels). Two large, bright spots appear within the nanoflake and sporadic pixels appear in the background areas beyond the nanoflake contour. The MATLAB function *regionprops* was used to collect spatial information regarding the number of connected "1" pixels in the binary image. First, we filtered the initial binary image in Figure S3.13a by rejecting all pixels outside the nanoflake boundary (Figure S3.13b). Next, we rejected any pixels that were not 4-point connected using the *bwconncomp* function and any pixel groups less than 4 pixels. This filtering procedure effectively removed sporadic "hot" pixels that statistically passed the threshold value but did not coincide with obvious qualitative iodine formation events in bright field transmission images. Figure S3.13c shows a typical binary image of an iodine deposition event after the filtering algorithm.

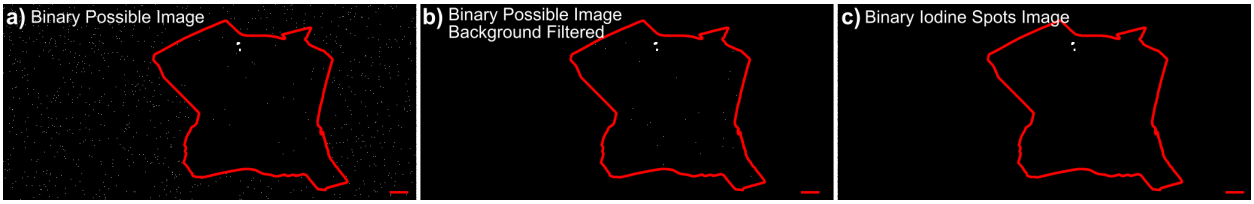

Figure S3.13: Iodine deposition spot identification and filtering. (a) A binary image of the nanoflake where all possible iodine deposition pixels are marked in white (pixel values of 1). (b) The same image as (a) after the first round of filtering that removes any possible spots in the background. (c) The final binary iodine spots image after the last filtering step, see SI text for details. The red line indicates the boundary of the nanoflake in all panels.

The final binary image was also used to calculate the distance between the laser spot and iodine deposition spot, which is defined as $d_{transport}$ in **Error! Reference source not found.**. We repeated t hat procedure for all "steps" in the line scan and overlaid all the iodine deposition location information on a single image using the transformation matrix procedure described above. The result is a single image that contains an overlay of all the iodine deposition spots for the entire molecular reaction imaging experiment.

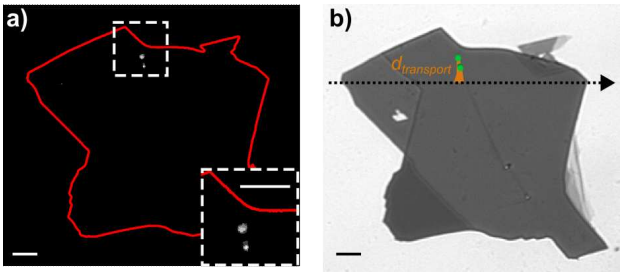

Figure S3.14: Quantifying the charge transport distance. (a) Binary image of a single nanoflake showing iodine deposition spots in white. The inset shows a zoomed in section with the deposition spots. The red line indicates the boundary of the nanoflake. (b) The control image of the nanoflake with the iodine deposition spots overlaid in green. The orange lines indicate the $d_{transport}$ vector. The black, dashed arrow shows the laser scan direction.

Supplementary Note 3.3: Calculation of Critical Incident Light Intensity for Iodine Formation (I_{crit})

We calculated the critical light intensity to induce iodine deposition following the procedure used by Isenberg, et. al.[S3.2] To do this, we fixed the position of a focused 532 nm laser on individual nanoflakes and measured the photocurrent as a function of the incident laser power (I_0). Figure S3.15a,b shows representative chronoamperometric data measured at 0.600 V vs. Ag/AgI. As expected, the photocurrent magnitude increases with increasing laser power. Following the procedure used by Isenberg, et. al. we calculated the derivative of the chronoamperometric data during the illumination period. Figure S3.15c shows the mean value of the derivative versus I_0 on a log–log scale. The derivative value remains flat with increasing I_0 until a critical power where the value dramatically increases. We quantitatively defined this critical incident light intensity (I_{crit}) using a linear fit (see Isenberg et al.[S3.2]). Performing this experiment for a large number of nanoflakes herein yielded typical I_{crit} values of 5 – 7 μW. We converted this laser power to photon flux to determine the laser power condition for the 415 nm laser used in these experiments. For example, a 532 nm laser power of 7 μW corresponds to an I_{crit} of ~ 2 x 10^{13} photon s^{-1}. This corresponds to a 415 nm laser power of 9.8 μW. We chose to switch to a 415 nm laser to coincide with the EQE mapping data, which was acquired with a 415 nm laser.

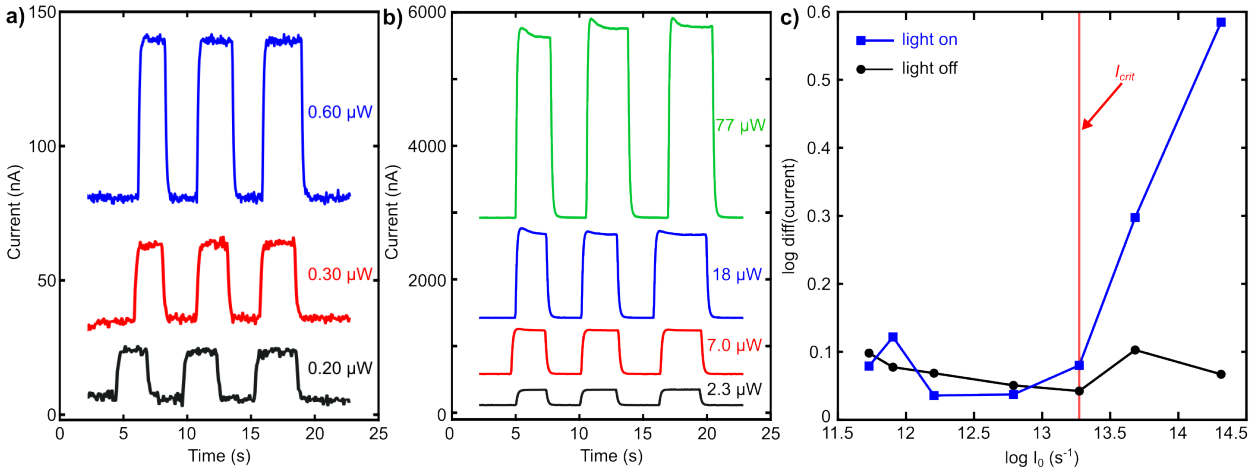

Figure S3.15: Determination of I_{crit} for molecular reaction imaging experiments. (a) Series of chronoamperometry measurements at various laser powers. (b) Same as (a) but for another series of laser powers. (c) Plot of the log of the derivative of the current as a function of the incident photon flux. The data is shown for both the light on and light off periods from (a) and (b). The determined value of I_{crit} is marked by the red vertical line.

References

S3.1. M. V. Erdewyk and J. B. Sambur, *ACS Appl. Mater. Interfaces*, **14**, 22737–22746 (2022).

S3.2. A. E. Isenberg, M. A. Todt, L. Wang, and J. B. Sambur, ACS Appl. Mater. Interfaces, **10**, 27780–27786 (2018).

APPENDIX C
BACKGROUND ANECDOTES ON THE RESEARCH RESULTS FROM CHAPTERS 2 & 3

Background On Chapter 2

The work contained in this chapter grew out of one of the oft-mentioned "failed" experiments, graduate students and PIs seem to always talk about. I had just begun to settle in on the 2D materials sub-group of the lab after jumping around on various other projects, and was working to build-up the capability to do direct-current photocurrent mapping experiments. I was spending the day in the laser lab, cranking out photocurrent maps when I noticed that the current trace on the potentiostat software had flipped sign. This immediately caught my attention and after watching a few more "line-scans" I was convinced that the data was real and not just some artifact. Throughout the rest of that day and the next few days I found more evidence of the same behavior – nominally n-type materials exhibiting p-type behavior under an anodic applied potential. The rest of this chapter is our study of this phenomenon and our perspective on why this behavior is important to understand for any group looking to study TMD materials.

Background On Chapter 3

This chapter is an interesting one because the groundwork for the imaging experiments described here was laid before any of the data contained in Chapter 2 was ever collected. The basic idea was seeded before I ever joined the group. Dr. Michael Todt and Allan Isenberg, in working on the very first Sambur group publication observed bubbles of iodine form on the surface of $MoSe_2$ nanoflakes. Allan then followed up on this observation with correlated Raman microscopy of these droplets. From there, I believe it wasn't until Dr. Li Wang, a former post-doc in the Sambur group, observed a similar phenomenon on a TMD heterostructure sample he was studying. Li had

discovered a way to do reversible iodine deposition upon illumination of a nanoflake. I remember being in the laser lab watching him “drive” around the microscope and observing the now characteristic dark deposition spots appear, and then disappear. At that time, we weren’t sure of the significance of these observations and we didn’t have a good way to systematically test and subsequently analyze the data from a large number of flakes. However, when I moved over to the 2D materials sub-group, this problem became a little project of mine. I was able to develop an image analysis algorithm to find the deposition spots and then pull out meaningful metrics from the data. But all this got pushed to the side, while we looked to develop better mapping protocols, which is when the observations that led to Chapter 2 came about. It wasn’t until after I had begun writing the manuscript contained in Chapter 2, that I turned my attention back to the iodine deposition experiments that are contained herein.